A HYBRID OPTICAL TWEEZERS AND PHOTOACOUSTIC MICROSCOPY SYSTEM

by

Esra Aytaç Kipergil

B.S., Integrated MS & BS Program in Teaching Physics, Boğaziçi University, 2009,

M.S., Physics, Boğaziçi University, 2012

Submitted to the Institute for Graduate Studies in
Science and Engineering in partial fulfillment of
the requirements for the degree of
Doctor of Philosophy

Graduate Program in Physics

Boğaziçi University

2017

ACKNOWLEDGEMENTS

Before all else, I wish to acknowledge to my thesis supervisor Prof. Mehmet Burcin Unlu for all his encouragement, generous instruction, relieving guidance and the countless time he has spent for me through all my years as a graduate student. One simply could not wish for a friendlier and understanding advisor.

I would like to express my sincere gratitude to the mentor of this thesis Dr. Hakan Erkol for his valuable guidance for every step of this study. I gratefully acknowledge him for helpful discussions and for his efforts in constituting theoretical basis of photoacoustics. He is not only a mentor but also a precious friend. I feel honored to work with him.

Thanks to my dearest friend Nasire Uluc for her sharing through all the years. Apart from academic help, she always provided me moral and emotional support and became my sister. I am also very thankful to Aytac Demirkiran for his friendship and for the countless time we spent together in our laboratory. Also I want to thank Alican Kartal for his assistance during the experiments.

I would like to express my gratitude to Dr. Seydi Yavas, Dr. Ugur Parlatan, and Dr. Alessandro Magazzu for their help, guidance and consultancy. Without their contribution this dissertation would not be possible.

A very special gratitude goes out to TUBITAK (Grant No: 213E033), Ministry of Development (Project No: 2009K120520), Bogazici University Research funding (Grant No: BAP 15B03TUG3) for funding of the work.

I would like to thank my husband Mustafa Faruk Kipergil for his endless support, and understanding to every aspect of my life. My special and deepest thanks to my father and my mother for their strength, help, and for everything.

ABSTRACT

A HYBRID OPTICAL TWEEZERS AND PHOTOACOUSTIC MICROSCOPY SYSTEM

Photoacoustic microscopy (PAM) is a promising imaging modality that combines optical and ultrasound imaging. It takes advantage of high optical contrast and high ultrasonic spatial resolution. Conventionally, piezoelectric transducers are used to detect photoacoustic waves. Here, it is aimed to utilize a particle trapped by an optical tweezers (OT) system as a sensor by tracking the change in its displacements caused by the photoacoustic radiation force. By this way, it is possible to put the detector as close as a few microns to the absorber which is not possible with any other currently existing detection mechanisms. An all-fiber integrated laser with custom-developed electronics and software is developed specifically for the hybrid PAM and OT system. The laser is home-built for maximum flexibility in adjustment of its parameters; pulse duration (5-10 ns), energy (up to 10 μJ) and repetition frequency (up to 1 MHz) independently from each other. It covers a broad spectral region from 450 to 1100 nm and can also emit wavelengths of 532, 355, and 266 nm. Photoacoustic radiation force caused by the change in the density of time-averaged kinetic and potential energy of the acoustic wave when encountered with a compressible or incompressible sphere is analyzed theoretically. Then, experiments are conducted on several particles and cells to manipulate them inside an absorbing medium. Apart from system development for diagnostics, to turn a hand on the treatment side, proton-induced acoustics is studied which has a potential to get real-time feedback for intratreatment adjustments and to reduce range uncertainty via high spatial resolution in ultrasound. In this regard, an analytic solution for the proton-induced acoustic wave is presented; then it is combined with an analytic approximation of the Bragg curve. The influence of the beam energy, pulse duration and beam diameter variation on the acoustic waveform are investigated.

ÖZET

HİBRİT OPTİK CIMBIZ VE FOTOAKUSTİK MİKROSKOP SİSTEMİ

Fotoakustik mikroskop sistemi optik ve ultrason görüntüleme sistemlerini birleştiren gelecek vaadeden bir sistemdir. Hibrit yapısı gereği optik kontrast ve yüksek uzaysal ultason çözünürlükten aynı anda faydalanmaktadır. Geleneksel olarak fotoakustik dalgalar piezoelektrik problarla algılanmaktadır. Bu tezde ses algılanmasının optik cımbız tarafından tuzaklanan parçacık vasıtasıyla yapılması hedeflenmiştir, bu sayede soğurucuya halijazırda kullanılan herhangi bir dedektörün yapamayacağı kadar (birkaç mikron) yakınlaşılmak hedeflenmiştir. Hibrit fotoakustik mikroskop ve optik cımbız sistemi için özel olarak fiber lazer sistemi geliştirilmiştir. Bu lazer sistemi parametrelerinde azami ayarlanabilirlik sağlanacak şekilde tasarlanmıştır. Geliştirilen lazerin atım süresi 5-10 ns arasında, atım enerjisi 10 μJ'e kadar ve tekrar sıklığı 1 MHz'e kadar birbirinden bağımsız olarak ayarlanabilmektedir, dalga boyunu ise 450-1100 nm arasında ayarlamak ve 1064 nm'nin harmonikleri olan 532, 355, ve 266 nm'den faydalanmak mümkündür. Fotokustik dalgalar sıkıştırılabilir veya sıkıştırılamaz parçacıklarla karşılaştığında, kinetik ve potansiyel enerji yoğunluğunluğun değişiminden ötürü parçacıklara kuvvet uygulamaktadırlar. İlk olarak bu kuvvetler hakkında teorik çalışmalar yapılmış daha sonra da deneysel olarak parçacıklar ve hücreler bu kuvvetlerle manipüle edilmiştir. Teşhiş için yapılan bu çalışmalar dışında tedavi kısmında da yer almak için proton tarafından indüklenen akustik dalgalar da incelenmiştir. Bu ses dalgalarının takibinin tedavi sırasında düzenleme yapma imkanı tanıma ve yüksek uzaysal çözünürlüğü sayesinde proton menzil belirsizliğini azaltma gibi potansiyel faydaları bulunmaktadır. Bu konuda dalga denklemi analitik olarak çözülmüş, ışının enerji, atım süresi, ve çapı gibi değişkenlerinin etkileri incelenmiş, ayrıca frekans uzayında da analizler yapılmıştır.

TABLE OF CONTENTS

LIST OF FIGURES

LIST OF TABLES

LIST OF SYMBOLS

α	Linear polarizability constant
β	Conversion factor
δ_{tot}	Total damping constant
ϵ	Small fraction
η	Viscosity constant
γ	Friction coefficient
$\gamma^{(ex)}$	Experimental friction coefficient
κ	Trap stiffness
λ	Wavelength
μ_a	Absorption coefficient
∇	Gradient
ν	Speed of sound
ν_{PRF}	Pulse repetition frequency
ω_0	Resonant frequency of a microbubble
$\overline{T_i}$	Time-averaged kinetic energy density
$\overline{V_i}$	Time-averaged potential energy density
ρ	Density
ρ_s	Density of the particle
σ	Beam width
τ	Pulse duration
τ_{ot_x}	Trap characteristic time
τ_L	Non-dimensional pulse duration
τ_m	Momentum relaxation time
τ_r	Relaxation time
θ_R	Reflection angle
θ_T	Transmission angle
φ	Scalar potential of the velocity field

LIST OF ACRONYMS/ABBREVIATIONS

ACF	Autocorrelation Function
ARF	Acoustic Radiation Force
ASE	Amplified Spontaneous Emission
BBO	Barium Borate
DAQ	Data Acquisition Card
DC	Double Clad
DWA	Dielectric Wall Accelerators
FFAG	Fixed Field Alternating Gradients
FFT	Fast Fourier Transform
FHG	Fourth Harmonic Generation
FPGA	Field Programmable Gate Array
FWHM	Full Width At Half Maximum
HOT	Holographic Optical tweezers
LBO	Lithium Triborate
LET	Linear Energy Transfer
LINAC	Linear Accelerator
LMA-PCF	Large Mode Area Photonic Crystal Fiber
MAP	Maximum Amplitude Projection
MOPA	Master Oscillator Power Amplifier
MPC	Multimode Pump Combiner
MRI	Magnetic Resonance Imaging
MSD	Mean Squared Displacement
NCPM	Non Critical Phase Matching
OCT	Optical Coherence Tomography
OPO	Optical Parametric Oscillator
OR-PAM	Optical Resolution Photoacoustic Microscopy
OSA	Optical Spectrum Analyzer
OT	Optical Tweezers

PAM	Photoacoustic Microscopy
PCF	Photonic Crystal Fiber
PDMS	Polydimethylsiloxanes
PET	Positron Emission Tomography
PI	Photoacoustic Imaging
PM-SMF	Polarization Maintaining Single Mode Fiber
PRF	Pulse Repetition Frequency
PSD	Power Spectrum Distribution
PVA	Polyvinyl Alcohol
PVCP	Polyvinyl Chloride Plastisol
RNAP	RNA Polymerase
SHG	Second Harmonic Generation
SLMs	Spatial Light Modulators
SNR	Signal To Noise Ratio
SOBP	Spread Out Bragg Peak
SPECT	Single Positron Emission Tomography
SRS	Stimulated Raman Scattering
THG	Third Harmonic Generation
UV	Ultra Violet
WDM	Wavelength Division Multiplexer
YD	Yterrbium Doped

1. INTRODUCTION

Photoacoustic microscopy (PAM) is a biomedical imaging modality that combines optical and ultrasound imaging. It takes advantage of high optical contrast and high ultrasonic spatial resolution owing to its hybrid nature. When a short laser pulse illuminates tissue, absorbed light leads to acoustic emission via thermoeleastic expansion [4–13]. Generated ultrasonic waves are commonly detected by transducers. Recorded signals are used to map the distribution of the locations of optical absorbers. Relatively low scattering of ultrasonic waves in biological tissues provides deeper penetration beyond the optical transport mean free path [7]. The contrast of PAM is endogenously produced by optical absorption of chromophores within the tissue [14, 15].

Photoacoustic imaging has various applications from material characterization to biomedical sciences [16, 17]. Photoacoustic imaging is safe for in vivo tissue imaging since it has a non-ionizing absorption mechanism. Considering these particular advantages, Photoacoustic imaging is a promising technique for biomedical optics. Resolution and contrast of photoacoustic imaging depend primarily on laser parameters. Thus, developing a model that reveals the dependence of the photoacoustic signal on laser parameters and building a laser that takes the results of the model into account is important to achieve optimal values for different applications.

In general, the laser system needs to produce short enough pulses, *i.e.*, several nanoseconds, in order to generate photoacoustic signals efficiently and emit wavelengths in the visible range to cover absorption peaks of tissue chromophores in their spectra [7, 18,19]. To obtain adequate penetration depth, it is also desirable to utilize a wavelength in the near infrared range, from 600 to 1200 nm, where biological tissues are relatively transparent [20, 21].

1.1. Lasers in Photoacoustic Microscopy Systems

Several kinds of lasers have been used for photoacoustic imaging. Pulsed laser diodes draw researchers' attention by being compact and inexpensive. While the peak power is relatively modest [20,22], it is sufficient to obtain adequate signal-to-noise ratio for in-vivo optical resolution photoacoustic microscopy (OR-PAM), as demonstrated in several publications [23–27]. On the other hand, they found only limited place in photoacoustic applications due to their lack of continuous tunability in wavelength. Q-switched Nd:YAG lasers operating at 1064 nm (and/or acquiring 532 nm by frequency doubling) are frequently utilized for PAM [20,28]. They are generally preferred because of their easy accessibility. However, their fixed wavelength output is a serious drawback for multispectral photoacoustic applications which quantify unique spectral features of each absorber by a set of wavelengths. On the other hand, Q-switched Nd:YAG pumped dye lasers, Ti:Sapphire lasers, and optical parametric oscillators (OPOs) are usually preferred for providing necessary wavelength tuning with high pulse energies (>1 mJ) [10, 11, 19, 29–37]; yet, they have some major limitations of their practical applications such as having low pulse repetition frequency (PRF) (generally less than 50 Hz, recently up to several kHz for OPOs [38, 39]), being bulky and expensive, and requiring external cooling units [17].

For the sake of enabling spectroscopic measurements, multiwavelength spectrum is obtained from a single wavelength emitting Q-switched Nd:YAG laser (sometimes microchip), either through stimulated Raman scattering (SRS) or nonlinear broadening by coupling its output to a fiber [40–49]. For lasers utilizing SRS, major energy is distributed on a series of fixed individual wavelength peaks that result from nonlinear interaction between incoming photons through the fiber and the molecules in the fiber itself, thus offers a limited wavelength tunability [50]. Polarization-maintaining single-mode fiber (PM-SMF) as well as PCF have been used for generation of SRS peaks [44, 45, 50–52]. Koeplinger *et al.* [45] reported four bands in a polarization maintaining single mode fiber (PM-SMF), and Loya *et al.* [44] improved the system with a broader wavelength tuning range also with a higher repetition rate and pulse energy per band.

Koeplinger *et al.* [45] sent the output of a Q-switched Nd:YAG microchip laser with a repetition frequency of 7.5 kHz to a frequency-doubling KTP crystal. Then, this output was sent to a 6 m-long PM-SMF and acquired four distinct bands 546, 560, 574, and 600 nm with a pulse energy of 80 nJ for the each wavelength. Loya *et al.* [44] coupled the output of a Q-switched Nd:YAG laser operating at 30 kHz repetition rate to a 30 m-long large mode area photonic crystal fiber (LMA-PCF) and individual pulse energies were reported as 270, 360, 520, 530, and 400 nJ at wavelengths of 532, 546, 568, 589, and 600 nm, respectively. It was also demonstrated that both discrete lines and a continuum can be produced by using four-wave mixing in a special fiber (SMF-28e) [46]. As a different technique, Buma *et al.* [47] used a birefringent optical fiber and produced discrete spectral bands in near infrared region. For comparison, Table 1.1 summarizes specifications of these lasers with respect to the pump laser, pulse duration, output wavelengths, measured pulse energies for some of the output wavelengths counting in the bandwidth of the filter, pulse repetition frequency, and fiber type. For all of the studies compared here, SRS in a fiber is utilized to obtain a multiwavelength spectrum except from Ferrari *et al.*'s study in which four-wave mixing is used [46].

Much more broader wavelength tuning can potentially be achieved by a supercontinuum source such as photonic crystal fiber (PCF), which relies on spectral broadening through nonlinear processes [2, 40, 53, 54]. PCF is a silica optical fiber with an ordered array of microscopic air holes running along its length [55, 56]. Figure 1.1 shows the structure of a PCF in detail [2]. The supercontinuum can also be generated in a standard silica based optical fiber. However, the high-index contrast between the core material and the air holes inside PCFs leads to a very strong waveguide contribution which is related to the geometrical distribution of air holes in the cladding microstructure.

Billeh *et al.* [40] utilized PCF for developing spectroscopic photoacoustic microscopy system. They sent the output of a Q-switched Nd:YAG microchip laser with a repetition frequency of 6.6 kHz to a 7 m-long PCF and reported seven wavelengths of

Table 1.1. Comparison of specifications of lasers with respect to the pump laser, pulse duration, output wavelengths, measured pulse energies for some of the output wavelengths counting in the bandwidth of the filter, pulse repetition frequency, and fiber type. For the studies compared here, SRS and four-wave mixing are utilized to obtain multiwavelength spectrum. PD: Pulse duration, OW: Output wavelengths, MW: Wavelengths for which energy values are measured, BW: Bandwidth, E: Energy, PRF: Pulse Repetition Frequency, and ML: Microchip laser.

	Pump Laser	**PD (ns)**	**OW (nm)**	**MW (nm)**	**BW (nm)**	**E (nJ)**	**PRF (kHz)**	**Fiber Type**
Koeplinger *et al.* 2011 [45]	Q-switched Nd:YAG ML	0.6	532, 546, 560, 574, 600		NA	80	7.5	6 m PM-SMF
Loya *et al.* 2012 [44]	Q-switched Nd:YAG	1.8	532-610	532, 546, 568, 589, 600	NA	NA	30	30 m LMA-PCF
Buma, *et al.* 2015 [47]	Q-switched Nd:YAG ML	0.6	1064 1100 1175 1225 1275 1375	1064 1097 1150 1215 1275 1325	NA 4 4.5 10 20 55	1170 250 390 480 430 200	7.4	20 m PM-SMF
Ferrari *et al.* 2015 [46]	Q-switched Nd:YAG	2	532-900	532, 546 590, 600 650, 700 750, 800 850	NA	up to 100	20	100 m SMF-28e

575, 625, 675, 725, 775, 825, and 875 nm with a bandwidth of 40 nm for each wavelength and pulse energies were measured as 7, 15, 24, 31, 31, 31, and 33 nJ, respectively.

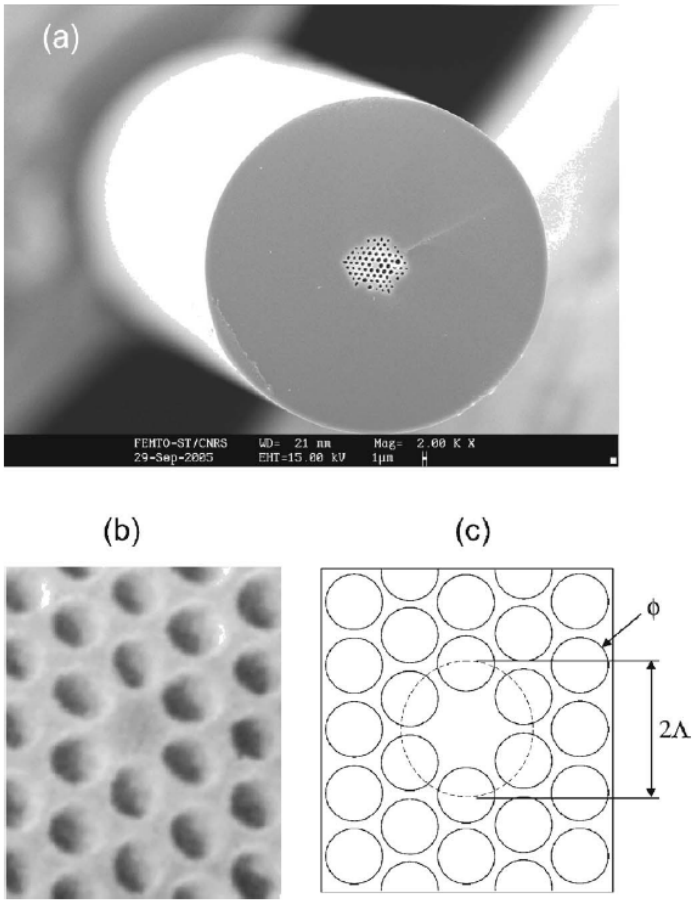

Figure 1.1. Photonic crystal fiber structure. a) Electron micrograph of the PCF used in the supercontinuum generation experiments of Ranka *et al.* [1]. b) Central microstructure of PCF in detail, and c) ideal hexagonal structure with the parameters of $\Lambda = 1.6$ μm pitch and $\phi = 1.4$ μm hole diameter [2].

Lee *et al.* [41] also built a supercontinuum laser system for both PAM and optical coherence tomography (OCT). Afterwards, they determined oxygen saturation of hemoglobin and hemoglobin concentration via the same laser source [42]. They also sent the output of the same type of laser to a 10 m-long PCF and stated pulse energy of the generated supercontinuum light as 500 nJ.

The pulse energies of two bands, 500 to 560 and 560 to 660 nm were measured as 0.6 and 1.8 nJ, respectively. As can be seen, these pulse energies are quite low despite the wide bandwidths. There are many attempts to develop multiwavelength laser systems generating higher pulse energies from the output of an integrated fiber for various photoacoustic imaging applications [40, 43–45, 49]. However, this condition requires PCFs to withstand such high energies. Since non-linearity increases as the effective mode area of fiber gets smaller; thus, it is advantageous to decrease core diameter for generation of more efficient supercontinuum. Yet, energy per surface area of the fiber has a major effect on the maximum optical pulse peak power which a fiber can withstand [57–59]. Therefore, there is a trade-off between supercontinuum efficiency and energy to be coupled into the fiber. In order to overcome this limitation, tapered fibers are designed. Bondu *et al.* [49] used a nonlinear fiber that combines a large-core fiber for high-pulse energy handling with a small-core fiber for efficient spectral broadening. They used five different PCFs with varying core diameters, two of them were tapered for supercontinuum generation. They also demonstrated that total energy at the output of the straight PCF with core diameters of 5, 9, and 10 μm as 10, 29.5, and 30 μJ, respectively; with visible output energies of 1.7, 5.4, and 4.6 μJ. Total output energy of tapered PCF of length of 1 m with an input core diameter of 10 μm tapered down to 5 μm was stated as 22 μJ with visible output energy of 6 μJ [43,49]. Whensoever the applications by coupling the output of Q-switched Nd:YAG microchip to PCF are considered, energy per band is reported to be lower in supercontinuum case than SRS, which may be a drawback for many applications [50]. In order to achieve wider tunability in the wavelength with high energy per band, Shu *et al.* [43] proposed a master oscillator power amplifier (MOPA) laser system with a home-built yterrbium-doped (Yb) fiber amplifier for power boost. The amplifier was coupled to a specially designed PCF taper that connects a large-core fiber that has a much more resistance to high-pulse energy at the input to a small-core PCF for spectrum broadening. Pulse energy per band increased dramatically and became comparable to the ones produced through SRS [43, 49]. Table 1.2 summarizes these comparisons with respect to the pump laser, pulse duration, output wavelengths, measured pulse energies for some of the output wavelengths counting in the bandwidth of the filter,

pulse repetition frequency, fiber type and the method. For all of the studies compared here, non-linear broadening in a fiber is utilized to obtain multiwavelength spectrum.

Table 1.2. Comparison of specifications of lasers with respect to the pump laser, pulse duration, output wavelengths, measured pulse energies for some of the output wavelengths counting in the bandwidth of the filter, pulse repetition frequency, fiber type. For all of the studies compared here, non-linear broadening in a fiber is utilized to obtain multiwavelength spectrum. PD: Pulse duration, OW: Output wavelengths, MW: Wavelengths for which energy values are measured, BW: Bandwidth, E: Energy, PRF: Pulse Repetition Frequency, and ML: Microchip laser.

	Pump Laser	**PD (ns)**	**OW (nm)**	**MW (nm)**	**BW (nm)**	**E (nJ)**	**PRF (kHz)**	**Fiber Type**
Billeh *et al.* 2010 [40]	Q-switched Nd:YAG ML	0.6	500-1300	575, 625, 675, 725, 775, 825, 875	40	7, 15, 24, 31, 31, 31, 33	6.6	7 m PCF
Lee *et al.* 2014 [42]	Q-switched Nd:YAG ML	0.7	500-1700	530, 610	60-100	0.6, 1.8	21	10 m PCF
Shu *et al.* 2016 [43]	Q-switched Nd:YAG ML	2	500-2300	NA	NA	NA	25	PCF Taper
Bondu *et al.* 2016 [49]	Q-switched Nd:YAG ML	4	500-1600	Total Visible	NA	4000	1	15 m PCF Taper

Apart from wavelength tunability, a laser system with high pulse repetition frequency (PRF) is also desired for fast image acquisition. The repetition frequencies of solid-state lasers are limited up to several kHz; but recently, fiber lasers with high

repetition rates emerge as an alternative excitation source for PAM. Through their high repetition rate, near real and real time imaging can be achieved [50, 60–62]. It has already been reported that in comparison to conventional systems with solid state lasers, the ones with fiber lasers are at least two orders of magnitude faster without compromising lateral resolution [60, 63]. Fiber laser sources are also used for in vivo and in vitro studies also including flow cytometry applications [60, 62–66]. The main disadvantage of these systems are their fixed wavelength that does not allow for multi-spectral functional imaging. To overcome the limitations, fiber laser technology seeking for tunability in wavelength is put forward. Hajireza *et al.* [51] developed an SRS fiber laser source for photoacoustic imaging. They coupled the output of an Yb fiber laser into a PM-SMF in varying lengths at different PRFs and extended the number of wavelengths at SRS peaks that were previously limited [50,52]. The acquired pulse energies were in between 100 to 500 nJ. In recent years, due to high power capabilities, MOPA laser systems have begun to be developed [67–69]. The first demonstration of a short pulse MOPA fiber laser at 1 μm was the study by Ilday *et al.* [70]. Allen *et al.* [67] produced a fiber laser system with a high repetition frequency in MOPA configuration with a single emission wavelength of 1064 nm. Mahmud *et al.* [68] demonstrated an OR-PAM system by using a commercial picosecond MOPA laser system consisting of a fiber-based tunable oscillator and three amplifier stages with a high power booster amplifier. However, the wavelength tunability was limited with 50 nm bandwidth. The output power was reported up to 1.1 W and pulse energy up to 500 nJ. Table 1.3 summarizes these comparisons with respect to the pump laser, pulse duration, output wavelengths, measured pulse energies for some of the output wavelengths counting in the bandwidth of the filter, pulse repetition frequency, fiber type and the method. For all of the studies compared here, pump lasers are fiber based, and SRS in a fiber is utilized to obtain multiwavelength spectrum.

For this thesis, to address the limitations of each approach, a tunable fiber based MOPA laser system producing nanosecond pulses, covering spectrum from 450 nm to 1100 nm is developed specifically for PAM. The supercontinuum part is all fiber-integrated; guided-beam-propagation renders its misalignment free and largely immune

to mechanical perturbations. Free space harmonic generation creates higher pulse energy for a specific band, i.e. 532 nm, and also generates ultra violet (UV) light with wavelengths of 355 and 266 nm. Total supercontinuum output power is over 1 W, and visible output power is around 270 mW at 65 kHz repetition rate corresponding to 4 μJ pulse energy.

Table 1.3. Comparison of specifications of lasers with respect to the pump laser, pulse duration, output wavelengths, measured pulse energies for some of the output wavelengths counting in the bandwidth of the filter, pulse repetition frequency, fiber type. For all of the studies compared here, pump lasers are fiber based and SRS in a fiber is utilized to obtain multiwavelength spectrum. PD: Pulse duration, OW: Output wavelengths, MW: Wavelengths for which energy values are measured, BW: Bandwidth, E: Energy, and PRF: Pulse Repetition Frequency.

	Pump Laser	**PD (ns)**	**OW (nm)**	**MW (nm)**	**BW (nm)**	**E (nJ)**	**PRF (kHz)**	**Fiber Type**
Hajireza *et al.* 2013 [51]	Yb-doped fiber laser	1	532, 543, 560, 590, 600		10	300-500	40	3 m PM-SMF
Hajireza *et al.* 2014 [50]	Yb-doped fiber laser	1	545, 550, 558, 570, 580, 590, 600		NA	136, 76, 151, 21, 105, 213, 116	160	6 m PM-SMF
Mahmud *et al.* [68]	Fiber based laser (MOPA)	0.1-5	1030-1080 515-540	1064	NA	500	100-120000	NA

One of the novelties here is the improvement of wavelength tunability, output power, and pulse energy when fiber-based lasers are benchmarked. This is the first demonstration of spectroscopic PAM by developing a supercontinuum all-fiber based

MOPA source. The tunability of the laser parameters allows using only one laser for many different PAM applications, and also high repetition rate enables fast scanning. The coverage of near-UV spectrum gives an opportunity to image cell nuclei. As certain morphological changes such as size and shapes irregularities in the nuclei are known indicators of various cancers [35, 71], this system may also be useful for cell nuclei studies as well.

1.2. Optical tweezers

Optical tweezers (OTs) are used for trapping and manipulating small particles after Ashkin pioneered the technique. The momentum transfer of light to the particle generates radiation pressure, and when it is tightly focused, sufficiently large forces can be exerted on the particle to confine it near the focus [72]. Initially trapping of dielectric particles from nanometer to micrometer sizes are demonstrated, and rapidly the research has expanded to trap organic materials such as eukaryotic cells, bacteria, viruses, and even to organelles within cells [73]. Currently, it is possible to trap not only dielectric particles but also metallic nanoparticles through exploiting their plasmonic response [74].

The basic operation principle of optical tweezers is grounded on the change in the momentum of a photon, due to an alteration in its direction by reflection, refraction, or scattering during interaction with a particle. In the presence of no external forces, conservation of momentum implies that the particle should undergo an equal and opposite momentum change in compliance with Newton's second law whose rate produces a force acting on the particle. The momentum of light is expressed as, $p = h/\lambda$, where h is Planck's constant and λ the wavelength of the light.

The forces can be classified into two types: scattering and gradient force. The former is proportional to the intensity of the light and pushes the particle towards beam center in the case that refractive index of the particle is bigger than of the medium $n_p > n_m$. The latter is towards the beam axis due to the gradient in the

intensity of light as in the Gaussian profile, the light at the center is more intense than the edges. Figure 1.2a shows gradient and Figure 1.2b scattering forces with different directions. [3].

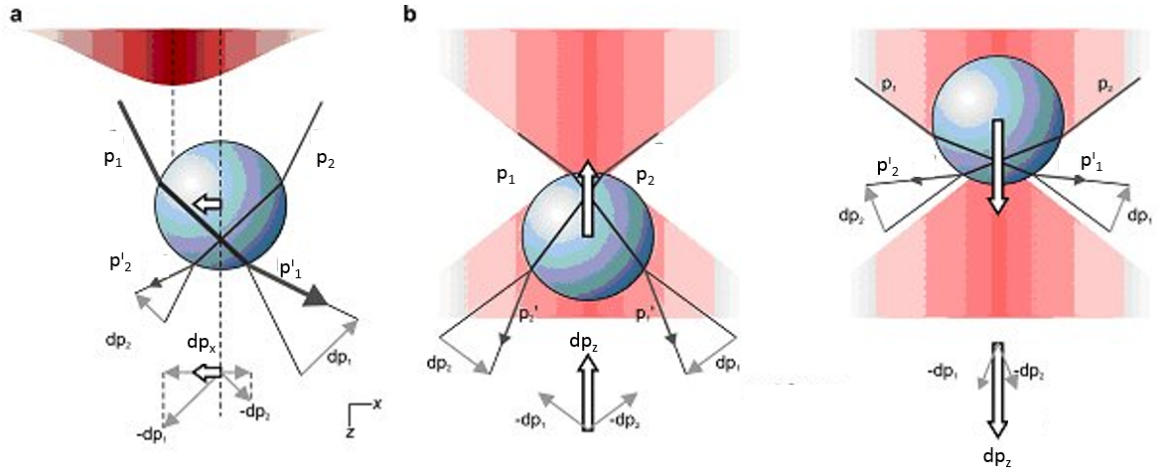

Figure 1.2. a) Gradient, b) scattering forces acting on a particle in a trap [3].

Based on the comparison of the wavelength of light to the dimension of the particle, the theoretical explanation of optical trapping utilizes some approximations referred as the Rayleigh and the Mie scattering regime. In the Mie scattering regime, the diameter of the particle is much larger than the wavelength of the light, $d >> \lambda$ and ray optics model can be applied. For the particles with diameters smaller than the trapping wavelength, $d << \lambda$, Rayleigh regime holds, and electromagnetic theory can be used to treat particles as point dipoles [72, 75, 76].

1.2.1. Ray Optics Regime

In this regime, the forces on a spherical particle with refractive index larger than the surrounding medium that is uniform and non-dispersive can be calculated directly by geometric optics as following [77]:

$$F_{scat} = \frac{n_m.P}{c}(1 + Rcos(2\theta_R) - \frac{T_F^2(cos(2\theta_R - 2\theta_T) + Rcos(2\theta_R))}{1 + R^2 + Rcos(2\theta_T)} \tag{1.1}$$

and

$$F_{grad} = \frac{n_m.P}{c}(1 + Rsin(2\theta_R) - \frac{T_F^2(sin(2\theta_R - 2\theta_T) + Rcos(2\theta_R))}{1 + R^2 + Rcos(2\theta_T)} \tag{1.2}$$

Here n_m, P, c, R, T_F, θ_R, and θ_T are refractive index of the medium, power of the ray, speed of light, Fresnel reflection, transmission coefficients and angles, respectively.

1.2.2. Rayleigh Regime

In the case that the wavelength of trapping laser is much bigger than the diameter of the particle, geometric optics regime is not valid, light can not be represented as rays. However, forces can be determined by using electromagnetic theory by behaving the particle as a point dipole. Lorentz force acts on the dipole as a result of spatially varying intensity in the electromagnetic field and can be expressed as following

$$\vec{F} = -\vec{\nabla}U \tag{1.3}$$

Electrostatic potential due to the interaction between dipole with an electrostatic field, $\vec{E}$, is defined as a vector product with dipole moment, $\vec{p}$.

$$U = -\vec{p}.\vec{E} \tag{1.4}$$

By using some vector identities, the force becomes

$$\vec{F} = \vec{\nabla}(\vec{p}.\vec{E}) = \vec{p} \times (\vec{\nabla} \times \vec{E}) + (\vec{p}.\vec{\nabla})\vec{E} \tag{1.5}$$

By using the result of Maxwell's equations in the absence of time-varying magnetic field [78]

$$\vec{\nabla} \times \vec{E} = 0 \tag{1.6}$$

and the linear relationship between the induced electric field and the polarization for the weak fields ignoring the higher orders [79]

$$\vec{p} = \alpha \vec{E} \tag{1.7}$$

where α is the linear polarizability constant, Equation 1.5 becomes

$$\vec{F} = (\alpha \vec{E}.\vec{\nabla})\vec{E} \tag{1.8}$$

The electric polarization of the dielectric can be defined as the electric dipole moment induced per unit volume of the dielectric material. By using the following vector identity

$$\vec{\nabla}\vec{E}^2 = 2(\vec{E}\vec{\nabla})\vec{E} + 2\vec{E} \times (\vec{\nabla} \times \vec{E}) \tag{1.9}$$

gradient force that confines the particle around focus, i.e. Equation 1.8 can be expressed as

$$\vec{F}(\mathbf{r}, t) = \frac{1}{2}\alpha\vec{\nabla}\vec{E}^2(\mathbf{r}, t) \tag{1.10}$$

The particle experiences a time averaged gradient force, the relation $\langle\vec{E}(\mathbf{r}, t)^2\rangle_t = \frac{1}{2}|\vec{E}(\mathbf{r})^2|$ yields the force

$$\vec{F}_{grad} = \langle\vec{F}(\mathbf{r}, t)^2\rangle_t = \frac{1}{4}\alpha\vec{\nabla}|\vec{E}(\mathbf{r})|^2 \tag{1.11}$$

The intensity of light, *i.e.*, power per unit area is related to the square of the magnitude of the electric field is expressed by [80]

$$I(r) = \frac{n_m\epsilon_0 c}{2}|\vec{E}(\mathbf{r})|^2 \tag{1.12}$$

where n_m, ϵ_0, and c are refractive index of the medium, permittivity of free space, and speed of light, respectively. Putting Equation 1.12 into Equation 1.11 the following equation is acquired

$$\vec{F}_{grad} = \frac{1}{2n_m\epsilon_0 c}\alpha\vec{\nabla}I(\mathbf{r}) \tag{1.13}$$

By using Clausius-Mossotti and Lorentz-Lorentz relation for linear polarizability constant α,

$$\alpha = \alpha\prime\prime + i\alpha\prime\prime = 4\pi n_m^2\epsilon_0 r^3(\frac{m^2-1}{m^2+2}) \tag{1.14}$$

where n_p, and r are the refractive index and the radius of the particle with $m = \frac{n_p}{n_m}$, it adheres the following [80] definition of the gradient force:

$$\vec{F}_{grad} = \frac{2\pi r^3 n_m}{c}(\frac{m^2-1}{m^2+2})\vec{\nabla}I(\mathbf{r}) \tag{1.15}$$

The direction of the gradient force is toward the region of highest light intensity which is toward the beam axis in the case of a Gaussian beam profile. The scattering force is expressed as following in this regime [80]:

$$\vec{F}_{scat} = \frac{128\pi^5 r^6 n_m}{c}(\frac{m^2-1}{m^2+2})\vec{\nabla}I(\mathbf{r}) \tag{1.16}$$

1.2.3. Biomedical Applications of Optical tweezers

Optical tweezers have found their place also in bioscience. The possibility of non-invasively trapping and manipulating cells, bacteria, organelles and even single molecules open a cache of opportunities to research their interactions with the environment. For cells, the absorption coefficient of infrared light is low, thus the possibility of damage can be reduced by working in this region. There are many studies show that cells are viable after being tweezed [81, 82].

Optical tweezers are also crucial tools for measuring and applying of subtle such as a few picoNewtons [83]. Interactions in biological systems are made by such weak forces. In this regard, optical tweezers is a versatile technique for biomedical applications [84–88]. Whensoever biological objects themselves can not be trapped, as in the case of DNA or RNA because absorption dominates over scattering, coated and functionalized silica or polystyrene particles are used as handles [89]. Using optical tweezers, the elastic and mechanical properties of DNA and the effect of binding molecules on these features are analyzed [73,85,90–93]. Torsional properties of DNA are explored by many studies [94,95]. Research revealed crucial information about physical properties and the functioning of DNA enzymes. Under small extensions, DNA shows entropic elasticity, yet at higher stretching forces, it exhibits linear, i.e., enthalpic, elasticity [90, 96, 97].

Another critical exploration through optical tweezers is the dynamics of motor proteins as single biological molecules. They play key roles like transportation and packaging inside the cell by transforming chemical energy into mechanical one. Studies include muscle motor myosin that drives muscle contraction, intracellular transport motor kinesin and dynesin that walk the positive and negative end of the microtubule, molecular motor RNA polymerase (RNAP) that transcribes a DNA template into messenger RNA, viral DNA-packaging motor DNA polymerases [98–102]. In addition, optical tweezers served for understanding complex cellular processes including interactions between cells as well as with their environments and adhesion forces. Viscoelastic properties of cell membranes are studied by stretching them. It is also possible to fuse cells with optical tweezers such as bringing T-cells and other cells in order to study immune response. By combining the system with pulsed lasers, microsurgeries are performed [103,104]. Cell division mechanisms are examined by manipulating chromosomes; organelles are also trapped and repositioned [104].

1.3. Photoacoustic Radiation Force

There are numerous biomedical applications of acoustic radiation force (ARF) which is a period-averaged force that is applied by a sound wave on the medium.

Viscoelastic properties of biological tissues including breast, muscles, liver can be evaluated employing ARF [105–110]. Elasticity measurements are valuable for diagnostic reasons since anatomical structures differ for a healthy and abnormal tissue. Microparticles can be manipulated by ARF [111, 112]. Directing such agents to the location of interest is important since they may carry drugs and genes, enhance cell membrane and vascular permeability by being selected through the vasculature due to their size [113]. The acoustic force on microbubbles is widely explored in the literature due to their usage as contrast agents to increase the intensity of scattered echoes [114, 115]. There are many examples of using ARF in a standing wave for manipulation of cells, sorting and separating different particles [116–118].

One of the earliest theoretical explanation on ARF is made by King [119]. He expressed primary ARFs on a rigid, incompressible sphere suspended in a nonviscous ideal fluid. Calculations were based on a plane axisymmetric standing waves. Embelton extended the theory of radiation forces on incompressible spheres for spherical and cylindrical waves [120, 121]. Later, Yosioka and Kawasima derived the equations for compressible bodies whose compressibility is much larger than the fluid they are in [122]. Wu and Du made calculations for a compressible particle placed in the focus of the acoustic beam where is a stable point [123]. Utilizing a different model, Gor'kov obtained forces for an arbitrary sound field which is in a complete harmony with King's model [124]. The effect of the primary and the secondary radiation force on a microbubble is studied by Leighton and Dayton *et al.* both theoretically and experimentally [125, 126].

In contradistinction for conventional piezoelectric acoustic sources, short laser pulses may induce acoustic waves in a more efficient way [127, 128]. Zharov *et al.* presented a force expression for this kind of impact [129]. They introduced photoacoustic tweezers, based on the generation of forces because of the change in the density of time-averaged kinetic and potential energy. They also conducted experiments and controlled the movement of particles and cells inside an absorbing medium by means of forces induced by thermal and pressure gradients. This thesis puts its emphasis on acoustic

radiation forces produced by photoacoustic waves in which high spatial control of the applied force is assured by smaller focal spots through optics. Photoacoustic radiation force is critical for detection of ultrasound waves with the hybrid optical tweezers and photoacoustic microscopy system.

1.4. Proton Therapy

The main advantages of proton therapy are the finite range of the beam with a maximum dose at the end of this range and the sharp dose falloff at the distal edge [130]. Energy deposition and the speed of proton beams remain constant through medium until a depth where particles start to slow down which leads to an increase in the corresponding linear energy transfer (LET). Just before the end of protons' track, LET reaches to a maximum value when maximum energy deposition occurs, which is called as the Bragg peak [131]. In conventional photon therapy, *i.e.*, radiotherapy, the use of X-rays may cause damage to healthy tissue as a result of exponentially decaying dose along the beam path. However, if proton therapy is used, radiation dose is highly accumulated at the Bragg peak and consequently, the damage in the healthy tissue is minimized [132].

Nevertheless, real-time non-invasive monitoring of the radiation dose distribution still remains elusive. To address this issue, positron emission tomography (PET) has been suggested [133, 134]. However, low spatial resolution and unattainable real-time application of PET adversely affect its use [130]. Detection of gamma rays that are produced as a result of inelastic interaction between incoming protons and nuclei at the target site is another proposed method for dose monitoring [135, 136]. The main advantage of using gamma rays for this purpose is its real-time operation. However, lack of optimized gamma detectors renders its utilization limited [130]. Besides, conventional single positron emission tomography (SPECT) cameras cannot deal with the high energy gamma rays produced in proton therapy. Detection of these rays with a Compton camera has shown promise in range verification, yet minimum dose requirements should be satisfied to acquire adequate signal [137].

Short and varied lifetimes of isotopes, high cost, and complexity of the system are other drawbacks for the configuration [138]. In addition to the above-mentioned modalities, magnetic resonance imaging (MRI) is also used for *in vivo* range verification due to its high spatial resolution. However, further studies are needed to understand the role of MRI in proton therapy [139–141]. In summary, all of these approaches have their own obstacles. The difficulty of integration of imaging systems such as PET and MRI within the proton therapy facilities is another stumbling block on the way to practical applications of real time monitoring. As an alternative approach, dose monitoring through acoustic waves during the radiation therapy has been emerging.

The generation of acoustic waves induced by proton beams has been studied using simulations and verified with experimental studies. Sulak *et al.* [142] explained theoretical background in detail and performed an experimental verification. Hayakawa *et al.* [143] and Tada *et al.* [144] monitored pressure waves created in both water and animal muscle by pulsed proton beam. Hayakawa *et al.* [145] detected acoustic pulses from a hepatic cancer patient during treatment that showed up the possibility of monitoring dose distribution through acoustic signals. Space–time structure of hydroacoustic field was analyzed by Albul [146] and thermoelastic model was verified through both pulsed and continuous beams by Graf *et al.*, Terunuma *et al.*, and DeBonis, respectively [147–150]. Bychkov *et al.* [150] simulated proton induced acoustic waves with different methodologies and showed a consistency of their simulations with experimental data. Pressure waves generated from pre-Bragg peak heated region were also simulated by [151].

In 2015, many studies were presented regarding proton induced acoustic waves [138, 152–154]. Ahmad *et al.* [152] investigated the detection limits on proton-acoustic signals of distinct pulse durations for various beams of different energy, and spot size by using semi-empirical analytical model presented by Pedroni *et al.* [155]. They not only analyzed thermal noise of transducers' detection threshold but also reported the frequency and bandwidth of the acoustic signals to emphasize the importance of selection of transducers in proton-acoustics applications. Alsanea *et al.* [153] studied the

feasibility of using proton induced acoustics to measure the range and Bragg peak dose sensitivity by using Monte Carlo simulations based on computed tomographic methods. Assman *et al.* [154] varied proton beam pulse intensity and length in pursuance of determining an achievable position resolution of proton acoustics. Jones [138] observed acoustic waves generated by proton beams from a hospital-based proton therapy unit in which source current was modulated by a function generator to acquire desired spill time envelope.

Recently, Patch [156] correlated the Bragg peak location with target structure through overlaying the location of the Bragg peak onto its ultrasound image by simultaneously acquiring proton induced acoustic signals with a clinical ultrasound array at low energy. Jones [157] conducted simulation studies about the effects of pulse characteristics on the determination of proton-beam range.

One of the difficulties for the translation of this technique in clinical arena is the low amplitude of proton acoustic signals. Selection of the acoustic transducer is of paramount importance in this regard. The magnitude of the acoustic signal is strongly related to proton beam characteristics such as beam energy, pulse duration, and beam diameter [144, 152, 158]; hence, it is important to investigate the effect of these parameters. For this purpose, we first present an analytic solution of the proton-acoustic wave equation based on our previous work [159]. Secondly, we combine this solution with an analytical approximation of the Bragg curve established by Bortfeld [158]. This manuscript focuses on providing an analytical model that explicitly connects properties of proton beam and the acoustic wave. In general, the spatial and temporal profiles are described by Dirac delta point distributions. In our work, we use Gaussian spatiotemporal profiles to elucidate the relation between the parameters of the proton beam and the acoustic wave. We believe that our systematic study of different variables can be useful in studies of monitoring dose distribution through acoustics.

1.5. Thesis Outline

In Chapter 2, the stages of fiber laser system development for photoacoustic microscopy system is explained. Before the construction, an analytical solution of photoacoustic wave equation is obtained to reveal the relationship between the laser parameters and the photoacoustic signal. In the light of these analyses, specifications are determined, and a design of the laser that can be seen in sections of the chapter is put forward. The reason for building a custom made laser is to have flexibility on the parameters. Commercial lasers have built-in properties that can not be tuned or altered. Chapter 3 focuses on photoacoustic microscopy setup by using the home-made laser. Subsequently, determination of lateral resolution and various multiwavelength applications including cell studies in microfluidic devices take part under its sections. Conventionally, piezoelectric transducers are used to detect photoacoustic waves. In this thesis, trapped particle via an optical tweezers system is aimed to be utilized as a sensor. By this way, it is possible to put detector as close as a few microns to the absorber which is not possible with any other currently existing detection mechanisms. Photoacoustic radiation force is applied on the trapped particle which causes some changes in the position of it. By following the displacement of the particle, ultrasound waves could be detected. In Chapter 4, theoretical analysis regarding photoacoustic radiation force is shown, and then the results of experiments that are in harmony with the theory are exhibited. Chapter 5 is about detection of the sound waves originating from a source having the control on the amplitude and the frequency for calibrating studies. Subsequently, construction of the hybrid photoacoustic microscopy and optical tweezers system is explained, and then the results of experiments are presented. Apart from the hybrid system, this thesis has a final chapter which is about proton-induced acoustic waves. The motivation here is not only to focus on a system built for diagnostic purposes but also to monitor radiation therapy through acoustics. The physics behind proton induced acoustic waves is similar to that of photoacoustics, for this reason in Chapter 6, an analytic solution for the proton-induced acoustic wave is presented to reveal the dependence of the signal on the beam parameters; then it is combined with an analytic approximation of the Bragg curve. The influence of the beam energy,

pulse duration and beam diameter variation on the acoustic waveform are investigated. Further analysis is performed regarding the Fourier decomposition of the protonacoustic signals.

2. DEVELOPMENT OF A NOVEL FIBER LASER FOR PHOTOACOUSTIC MICROSCOPY SYSTEM

2.1. Oscillator and Pre-amplifier

An Yb-doped fiber is backwardly pumped by a 976 nm diode laser that can deliver 540 mW power at the furthest. The reason for the backward pumping is to reduce amplified spontaneous emission (ASE) rate. As a seed source, a 1064 nm diode laser is used and driven by a nanosecond diode driver (PicoLas, LDP – V03–100 UF V3). For harmonic generation, pulses with narrow bandwidths are beneficial, because longer crystals induce more efficient wavelength conversion; yet, the length of the crystal results in phase shifts in proportion to the bandwidth of the laser, a situation that decreases the efficiency. Therefore, diode laser is chosen to have a very narrow bandwidth of 0.3 nm. The driver is controlled through a field programmable gate array (FPGA) circuit (BASYS2, Xilinx). FPGA is chosen for its high-speed performance to generate pulses with durations of a few nanoseconds which is a requirement for photoacoustic imaging. 15 ns long pulses are generated with a repetition rate of 65 kHz and sent to the gain fiber. Pulse repetition rate can be adjusted electronically by means of FPGA and may go up to 1 MHz. Pulse duration may also be tuned in the same way, shorter pulse durations produce photoacoustic waves with greater amplitudes [160]. In front of the seed source, initially a directional isolator is used to block 1064 nm of light and then an omnidirectional ASE filter is used to prevent spontaneous emissions reaching back to it. The signal is combined with the pump through a wavelength division multiplexer (WDM) and sent to preamplifier.In the first stage, the pump is divided by a 30:70 coupler, 70% of the output pumps another Yb-doped fiber for further amplification. An average power of the output power of 170 mW is measured at the end of the second stage. An isolator with a maximum power handling of 2 W protects the stages from back reflections. Figure 2.1 shows the schematics of oscillator and pre-amplifier.

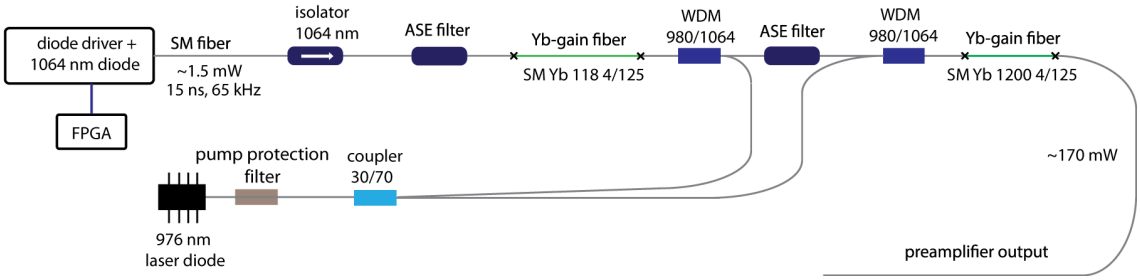

Figure 2.1. Schematic of oscillator and preamplifier. SM: Single mode fiber FPGA: Field-programmable gate array, WDM: Wavelength division multiplexer, and ASE: Amplified spontaneous emission.

At the end of the preamplifier, a 30:70 coupler allocates the signal. For supercontinuum generation 30% of the signal is utilized and 70% of that is used for free space harmonic generation.

2.2. Supercontinuum Generation

For the amplification of the signal that has an average power of 45 mW, a high power laser diode that can deliver a maximum power of 18 W and a double clad (DC) Yb-doped fiber (Yb-1200 20/125 PM, nLight Liekki) are used. A multipump combiner (MPC) (10-125, 2+1, 976/1064 nm) conjoines the signal and the pump just before the gain fiber. Figure 2.2 shows the schematics of supercontinuum generation.

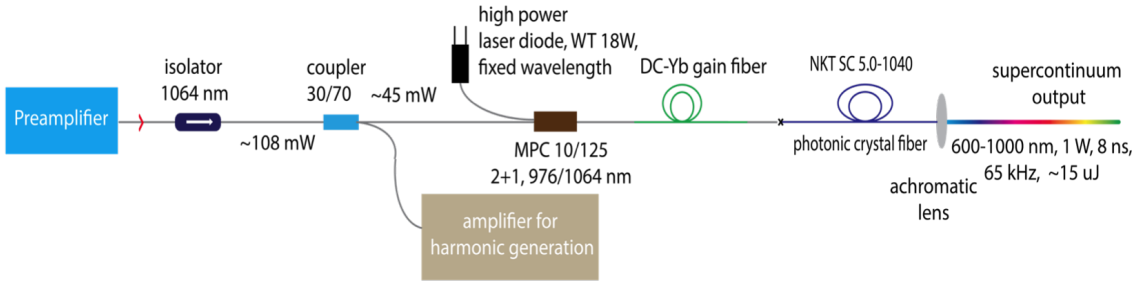

Figure 2.2. Schematic of supercontinuum generation. MPC: Multiple pump combiner.

A 15 m long photonic crystal fiber (PCF, SC 5.0–1040, NKT) with 5 μm core size is spliced to the end of the gain fiber for supercontinuum generation. As the length of the PCF increases, supercontinuum can be generated more efficiently [reference].The core size of the DC-Yb-doped fiber is larger than of PCFs', for this purpose, a special splice is utilized in between them. A splicer (FSM-100M, Fujikura) is used in which the positions of the fibers in front of the arc welds can be manually adjusted. Whenever, the splicer adjusts the positions automatically, the hexagonal structure of PCF may be ruined at the entrance of the PCF, and supercontinuum may not be produced. Total output power of supercontinuum is measured over 1 W with visible output power around 270 mW with a powermeter (S314C, Thorlabs) at 65 kHz repetition rate that corresponds to 17 μJ total and 4 μJ visible energy. Optical spectrum of the supercontinuum is measured by two optical spectrum analyzers (OSA) with different wavelength ranges; OSA 1 (Avaspec-3648-VIS, Avantes) and OSA 2 (QE65 Pro, Ocean Optics). The acquired spectra are digitally combined in a single plot (Figure 2.3).

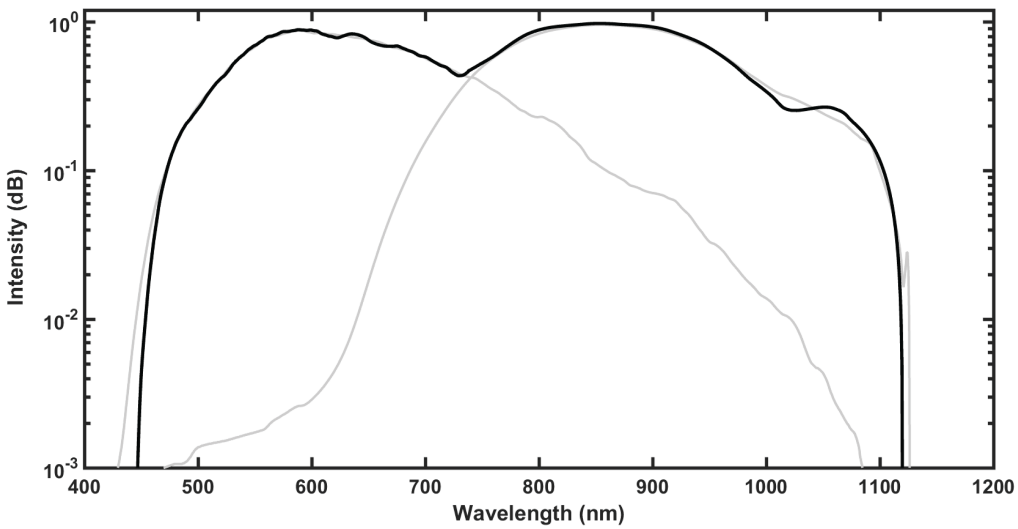

Figure 2.3. Optical spectrum of the supercontinuum output (acquired by OSA 1 and OSA 2, respectively).

In the first spectrum, the intensity of near infrared region appears lower than its actual level due to the decrease in the response of the analyzer while approaching

to the edges of the measurable spectra region. It may also be caused by the difficulty of collecting all the beam with broad spectrum which is collimated by a single lens. Although the lens is an achromatic lens, it may still not be enough to eliminate slight divergence for different wavelengths and thus amplitude measurement variation throughout this broad spectrum range. In the second one, the intensity of the region between 450 to 650 nm lowered to noise level as a result of using neutral density filters in order to prevent saturation of the detector for the remaining spectrum.

2.3. Harmonic Generation

Polarization of light is crucial for frequency multiplication; thus, 70% of the allocated signal is passed through a polarizer and all fiber components beyond this point are polarization maintaining. Figure 2.4 shows general schematics of harmonic generation including the final amplification.

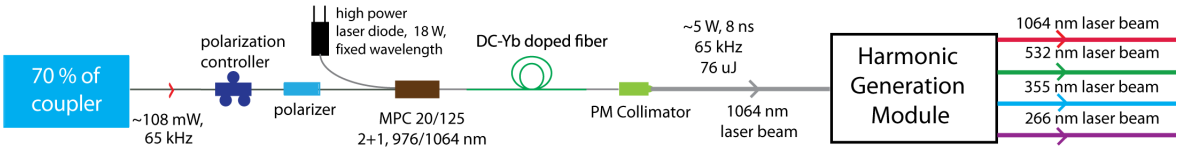

Figure 2.4. Schematic of harmonic generation.

A 976 nm diode laser is used and a multi-mode pump combiner (MPC) combines the pump and signal. A polarization maintaining double cladding Yb-doped (PM-DC-Yb) fiber is spliced to the end of the MPC for amplification of the signal and pulses with 8 ns duration with an average power of 3 W at 65 kHz repetition rate are acquired. Figure 2.5a shows the optical spectrum and Figure 2.5b shows the temporal profile of a pulse at the end of the amplification. In the temporal profile, the leading edge of the pulse is sharpened, or self-steepened, as the gain is partially saturated by each individual pulse and consequently less gain is available for the trailing edge. The temporal structure in the trailing edge is a static structure, which does not vary from

pulse to pulse, originating primarily from the dynamically varying impedance of the semiconductor diode that seeds the system.

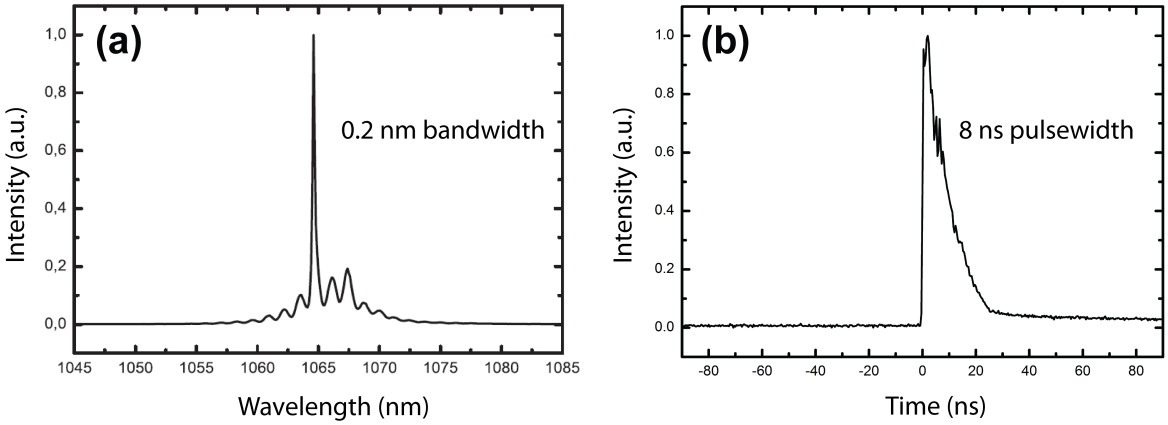

Figure 2.5. a) Optical spectrum and b) temporal profile typical pulse at the end of PM-DC-Yb fiber.

For frequency multiplication process, a half wave plate is employed to match the polarization between the isolator and crystals. An anti-reflection coated (for 1064 nm wavelength) lens with a focal length of 30 mm is used to focus light into crystal. For SHG, a 20 mm long Lithium Triborate (LBO) crystal (Eksma, LBO-405) is used. For non-critical phase matching (NCPM), a crystal oven and a proportional−integral (PI) controller is added to maintain the temperature at 150.8 °C that results in maximum power. The light is passed through an anti-reflection coated (for 532/1064 nm) lens for collimation. Two dichroic mirrors separate the generated SHG beam (532 nm light) from the 1064 nm beam. Here, the output power is measured as 500 mW for 532 nm light. A mirror hold including a dichroic mirror reflecting 532 nm wavelength is added to the system. When the mirror is flopped, beam including 532 and 1064 nm wavelengths pass through a lens to enter a crystal (Eksma LBO-407) for THG. The crystal is maintained at 40 °C for NCPM. The output power is around 3 mW for 355 nm light. Another flip mirror mount with a dichroic mirror that is transmitting 1064 nm and reflecting 532 nm beam is added to direct the beam toward a lens with a focal distance of 30 mm. This lens focuses the beam into a Barium

Borate (BBO) crystal (Eksma BBO-700, thickness = 6 mm) that generates second harmonic of the 532 nm beam (fourth harmonic generation), which results in around 10 mW of 266 nm light. The output of the crystal is filtered via a dichroic mirror reflecting 266 nm light and collimated by using a UV-coated lens with a focal distance of 50 mm. Figure 2.6 shows the schematics of harmonic generation module.

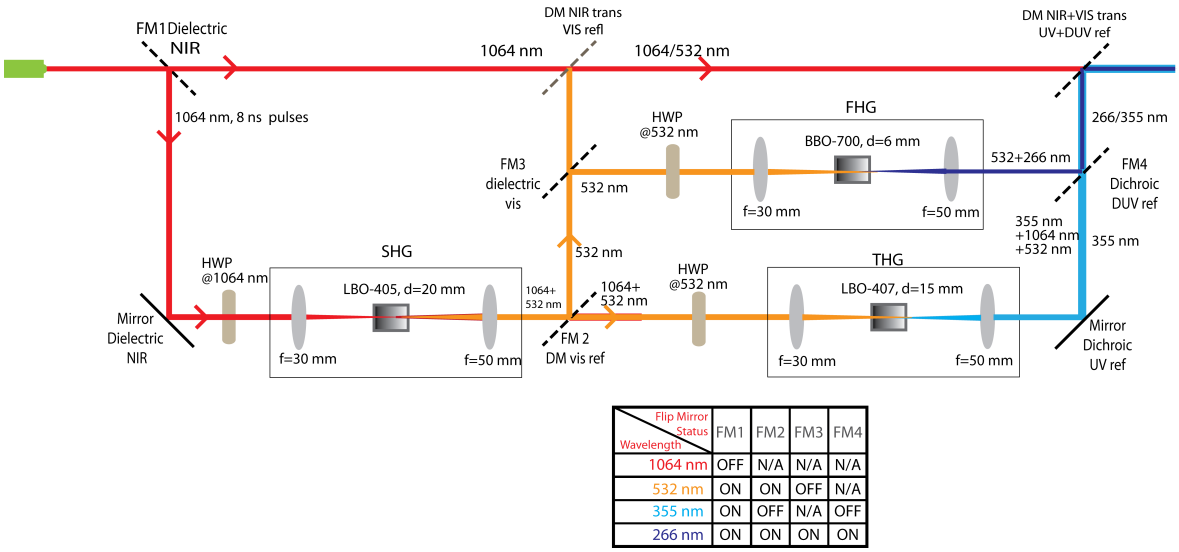

Figure 2.6. Schematic of harmonic generation module.

The optical spectrum of SHG is shown in Figure 2.7a and of THG in Figure 2.7b. The spectra are acquired with OSA 2 and OSA 1, respectively. The photographs showing the outputs of supercontinuum and harmonic generation units can be seen in Figure 2.8a and Figure 2.8b, respectively.

The developed laser system has a total supercontinuum output power over 1 W and visible output power around 270 mW at 65 kHz repetition rate corresponding to 4 μJ pulse energy. At the harmonic generation unit, average power of 532, 266, and 355 nm outputs are 500, 10, and 3 mW respectively. Table 2.1 summarizes these specifications with related pulse energies.

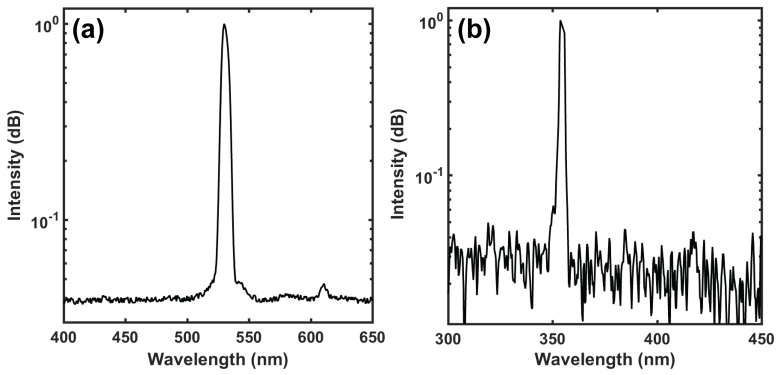

Figure 2.7. Optical spectrum of the a) SHG (acquired by OSA 2), and b) THG (acquired by OSA 1).

For photoacoustic imaging, desired wavelength is filtered from supercontinuum. Some of average power and pulse energy values can be seen at Table 2.2 after using several bandpass filters with both small and large bandwidths.

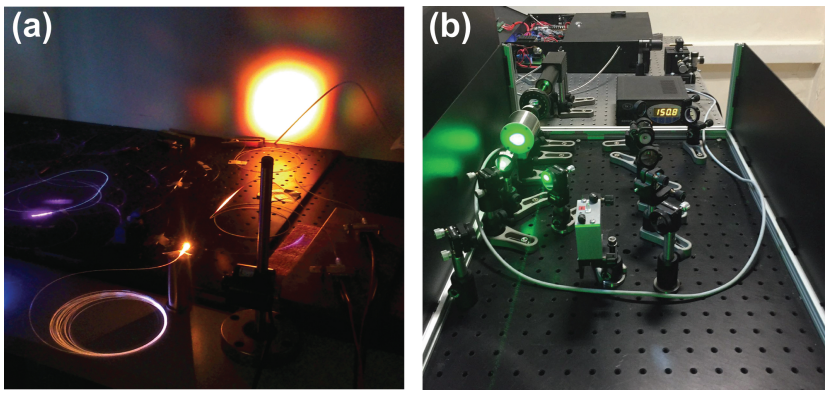

Figure 2.8. The photographs showing the outputs of a) supercontinuum and b) harmonic generation units.

Table 2.1. Output specifications of the fiber laser system.

	Average Power	**Pulse Energy (at 65 kHz)**
Supercontinuum	Total: 1 W	15 μJ
	Visible: 270 mW	4 μJ
Harmonic Generation	1064 nm: 5 W	76 μJ
	532 nm: 500 mW	7.7 μJ
	266 nm: 10 mW	150 nJ
	355 nm: 3 mW	46 nJ

Pulse energy values on the order of tens of nanojoules are sufficient for photoacoustic microscopic applications. The amount of energy increases towards the near infrared region since the wavelength broadens towards visible region from 1064 nm having the most intense power peak.

Table 2.2. Average power and pulse energy values for several outputs of supercontinuum.

Wavelength (nm)	**Bandwidth (nm)**	**Average Power (mW)**	**Pulse Energy (at 65 kHz)**
650	80	92	1.4 μJ
680	10	5	76 nJ
732	68	82	1.3 μJ
830	10	10	150 nJ
880	70	142	2.2 μJ

3. PHOTOACOUSTIC MICROSCOPY SYSTEM

The schematics of experimental setup for transmission mode OR-PAM system by using the irradiation source explained previously (Chapter 2) is shown in Figure 3.1.

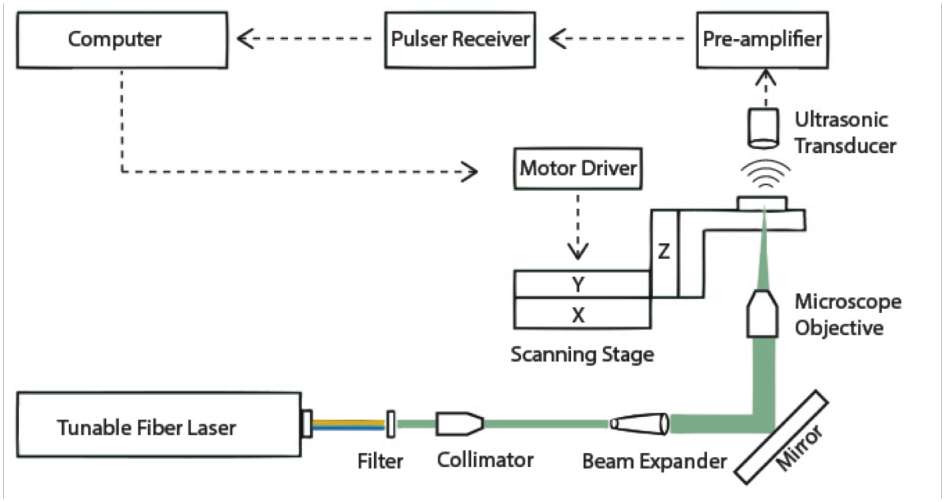

Figure 3.1. The schematic of experimental setup for transmission mode OR-PAM system.

A standardized resolution test target (USAF-1951, Thorlabs) was imaged for determination of the lateral resolution of our OR-PAM system. A transducer (V384, Panametrics) with a 3.5 MHz center frequency was used to acquire photoacoustic signals at the optical wavelength of 1064 nm filtered from the supercontinuum output. For focusing the light, a 5x objective (LMH-5x−1064, Thorlabs) was used. The target was immersed in water, then 2D raster scanning by a motorized linear translation stage (LNR50SEK1, Thorlabs) along the x-y plane in steps of 1 μm for an area of 300 $\times$ 330 μm^2 was performed. The acquired signals were averaged over 128 consecutive signal cycles. The trigger signal from the field programmable gate array (FPGA) of the laser was used to trigger a data acquisition card (DAQ) for synchronization. Following the triggering of each laser pulse, photoacoustic signals were initially amplified by 40 dB using a pre-amplifier (5678, 40 MHz bandwidth, Olympus) and then 39 dB

via a pulser/receiver (5073PR, Olympus). The signals were digitized through a DAQ (Razor Express CompuScope 1422, Gage Applied Technologies, Inc.), then data processing and reconstruction were performed. Figure 3.2a shows the optical microscopy image and Figure 3.2b presents the maximum amplitude projection (MAP) image of the scanned area (Group 6 and 7) of the test target. The lateral full width at half-maximum (FWHM) value from the imaged highlighted well resolved bars (Group 7, Element 6) was determined as 2.68 μm, as shown in Figure 3.2d.

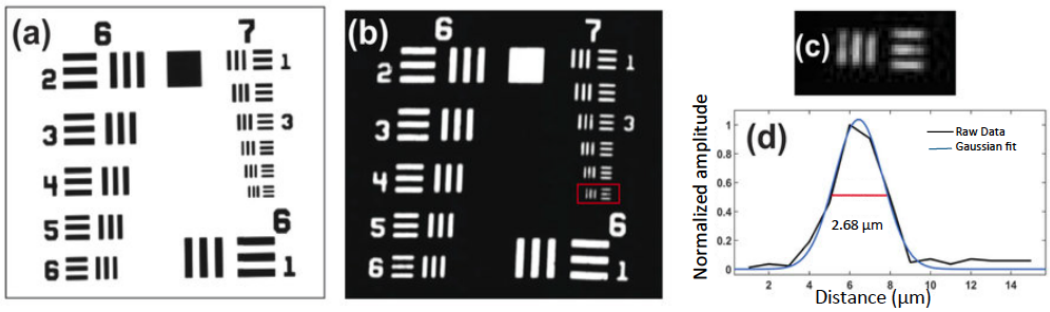

Figure 3.2. a) Optical microscopy image, b) photoacoustic microscopy image of USAF resolution test target (Group 6 and 7). c) Photoacoustic microscopy image of Group 7 Element 6. d) FWHM of a line at Group 7 Element 6 from Gaussian fit (blue) of raw data (black).

3.1. Phantom Studies

For the demonstration of our multiwavelength PAM system, Group 5 Element 6 of the test target were also imaged with six different wavelengths of 532, 650, 697, 732, 785, and 880 that can be seen in Figure 3.3a, 3.3b, 3.3c, 3.3d, 3.3e, and 3.3f respectively. These wavelength values except from 532 nm which was obtained by second harmonic generation (SHG), were filtered from the supercontinuum output of the laser for each experiment. A 10x objective (Plan Achromat, 0.25 NA, Olympus) was used to focus

light to the relevant area.

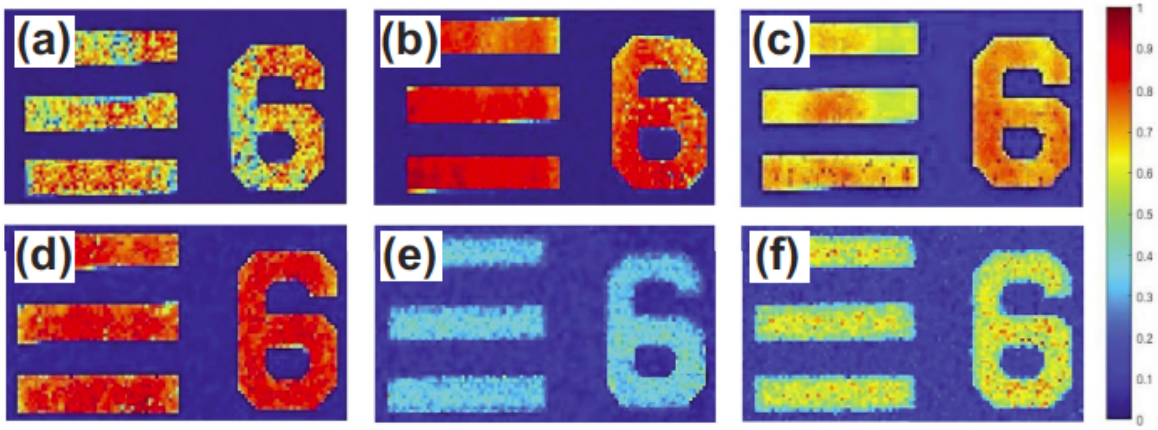

Figure 3.3. The PA image of Group 5 Element 6 scanned within an area of 56 × 101 μm^2 with steps of 1 μm acquired at optical wavelength a) 532 nm from harmonic generation unit, b) 650 nm, c) 697 nm, d) 732 nm, e) 785 nm, and f) 880 nm, respectively; from supercontinuum output.

Each data set is normalized internally and the same colour palette is used, but the variation in the absolute optical signal is about 15%.

3.1.1. Microfluidic Device Studies

Novel tissue-simulating phantoms should be utilized before conducting animal experiments. Materials with stable optical and acoustic properties are required to create phantoms. Some tissue-mimicking phantoms such as gelatin based and bovine gelatin phantoms are constructed by adding India ink, whole blood, copper/nickel chloride and fluorescent dyes (Direct Red 8, Evans blue) to provide optical absorbing for both pre-clinical and clinical applications of combined PA and US imaging [161–164]. Although these hydrogel-based materials are optically transparent, easy to prepare, and the speed of sound inside of them is similar to that in biological tissue, these types of phantoms have a limited re-usability capability. The reason for this is their low-temperature stability which may result in structural integrity loss [162]. Another drawback of using agar or agarose gel as a phantom is that the inhomogeneity of

concentration during preparation causes some changes in the speed of sound along the sample. Moreover, some absorbers such as copper or nickel ions were discovered to react with aqueous gels [164].

Polyvinyl alcohol (PVA) gels were described as solid photoacoustic breast phantoms [165]. A variety of procedures were employed for gel reinforcement by an increase in the cross-linking between the polymer chains to construct a higher dimensional network structure. However, the phantom which is only sensitive to humidity takes a long time to prepare through repeated freeze-thaw cycling [166]. Instead of using water-based materials (gelatin, agarose) and PVA gels as phantoms, polyvinyl chloride-plastisol (PVCP) that is synthesized from vinyl chloride monomers and insoluble in water is considered as an alternative phantom material. Spirou et al. first presented the utility of PVCP phantoms in a PA context [167]. The PVCP based tissue-mimicking phantom has a long-term stability with structural rigidity, as well as its Gruneisen parameter is greater than expected in tissue, which causes an increase the signal-to-noise ratio of the photoacoustic measurements. However, it has higher acoustic attenuation than tissue, and its preparation is not trivial [163]. Polydimethylsiloxanes (PDMS), a silicone-based polymer, can be incorporated into phantoms for photoacoustic applications. Creating microchannels within hydrogel structures is a challenge, yet the elastomeric properties and optical transparency of PDMS make it possible to design microfluidic channels and chambers with various geometries by using soft lithographic techniques. PDMS stiffness and hardness could be adjusted by changing the ratio of pre-polymer base to curing agent. Therefore, PDMS-based microfluidic devices are regarded as promising tools for phantom studies of photoacoustic microscopy [168–171].

For our studies, we used several microfluidic devices prepared by soft lithography. Figure 3.4 shows photographs of some of them which are different in thickness. Figure 3.5 belongs to the optical microscopy image of the channels of the devices.

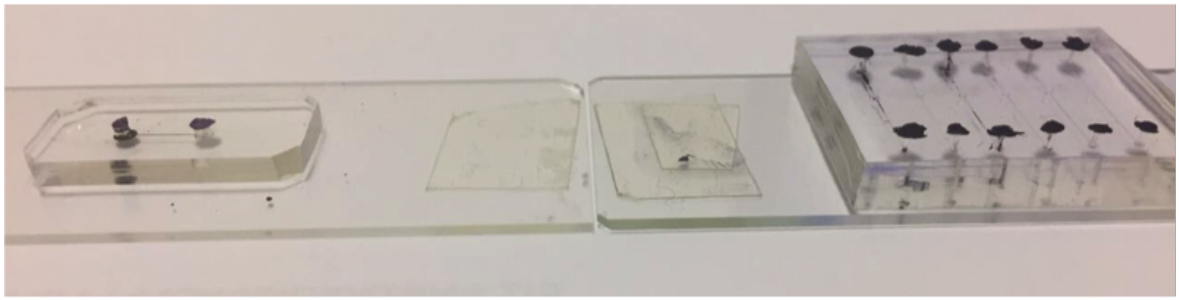

Figure 3.4. Photographs of microfluidic devices with different thicknesses.

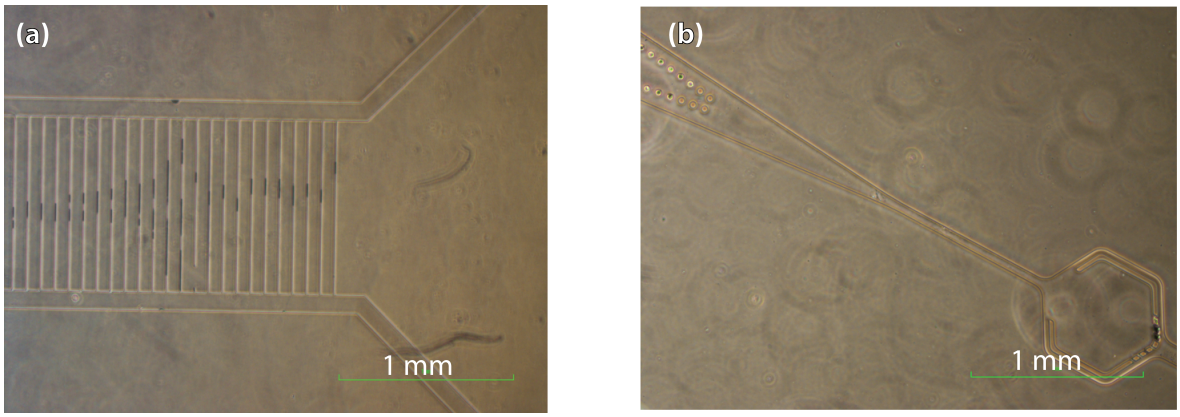

Figure 3.5. Optical microscopy image of the microfluidic devices' channels.

Photoacoustic image of a microfluidic device loaded with black ink was acquired for the PDMS thickness of 6 mm as can be seen in Figure 3.6. A transducer with a 3.5 MHz center frequency was used to acquire photoacoustic signals at the optical wavelength of 1064 nm filtered from the supercontinuum output. The device is immersed in water, then 2D raster scanned for an area of 4×1 mm^2 was performed. The acquired signals were averaged over 128 consecutive signal cycles. The resolution of the image is estimated to be around 5 μm which is the dimension of the pillars as they can barely be distinguished.

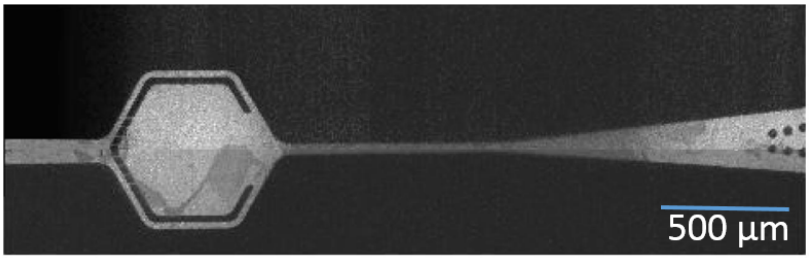

Figure 3.6. Photoacoustic image of a microfluidic device loaded with black ink for an area of 4 × 1 mm^2.

A microfluidic device loaded with red blood cells were also imaged with the photoacoustic microscopy system. Figure 3.7a shows the results of scanning for an area of 600 × 600 μm^2. A transducer with a 10 MHz center frequency was used acquire the photoacoustic image. Figure 3.7b and Figure 3.7c belong to CCD and optical microscopy images, respectively; for the comparison.

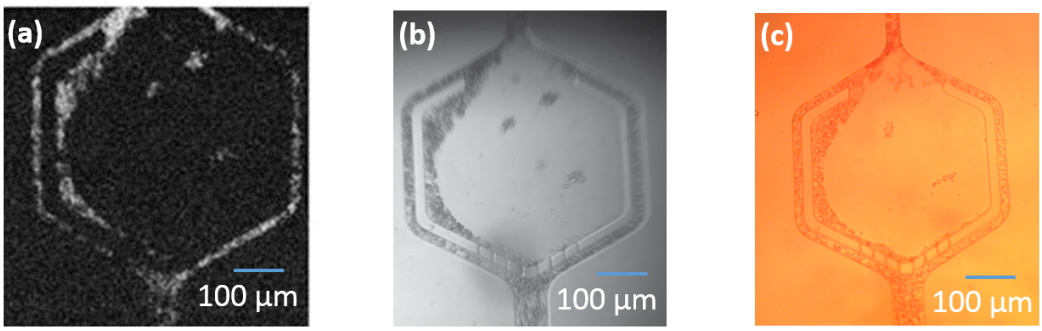

Figure 3.7. a) Photoacoustic, b) CCD, and c) optical microscopy image of a microfluidic device loaded with red blood cells.

Signal to noise ratio of the photoacoustic image is low since acoustic attenuation in PDMS is relatively high when compared to the tissue [172].

4. PHOTOACOUSTIC RADIATION FORCE

4.1. Photoacoustic Radiation Force on Compressible Spheres

Microbubbles may be considered as compressible microspheres so that primary radiation force is the time averaged product of the volume of the bubble and the gradient in the acoustic pressure as follows [125, 126]:

$$F_{primary} = \langle V \nabla p(r,t) \rangle \tag{4.1}$$

where V and ∇ are the volume of the bubble and gradient in space, respectively. The secondary radiation force is negligible compared to the primary force. In the case that the acoustic pressure matches the resonant frequency of the microbubble, the force expression can be simplified as

$$F = \frac{2\pi P_A^2 R_b \tau \nu_{PRF}}{\delta_{tot} \rho \nu \omega_0} \tag{4.2}$$

where P_A, R_b, τ, ν_{PRF}, δ_{tot}, ν, ρ, and ω_0 represents the pressure amplitude, radius of the bubble, pulse duration, pulse repetition frequency, density of surrounding medium, total damping constant, speed of sound, and resonant frequency, respectively [126]. It is noteworthy that Equation 4.2 is applicable when the center frequency of the acoustic wave and the resonant frequency of the bubble are equal. Moreover, Equation 4.2 is derived for a narrowband acoustic wave, yet the photoacoustic wave is generally broadband. However, the photoacoustic wave is reported as narrowband when the pulse duration of the laser is long [173]. For these reasons, the pulse duration is taken sufficiently long as $\tau = 1/2\omega_0$ which equates the center frequency of the photoacoustic wave to the resonant frequency. Table 4.1 summarizes the resonant frequencies and the corresponding pulse duration values used in calculations for three commercial microbubbles; Sovonue, Albunex, and Quantison that have 5 μm diameter.

Table 4.1. Resonant frequency ω_0 and corresponding pulse duration, $\tau = 1/2\omega_0$ for the microbubbles with diameter of 5 μm.

Microbubble	Resonant frequency ω_0 (MHz) [174]	Pulse duration $\tau = 1/2\omega_0$ (ns)
Sovonue	2.2	227.3
Albunex	5.2	96.1
Quantison	11.0	45.4

Table 4.2 summarizes the resonant frequencies and the corresponding pulse duration values used in calculations for microbubbles for three commercial microbubbles; Sovonue, Albunex, and Quantison that have 10 μm diameter.

Table 4.2. Resonant frequency ω_0 and corresponding pulse duration, $\tau = 1/2\omega_0$ for the microbubbles with diameter of 10 μm.

Microbubble	Resonant frequency ω_0 (MHz) [174]	Pulse duration $\tau = 1/2\omega_0$ (ns)
Sovonue	0.9	555.5
Albunex	1.9	263.1
Quantison	4.0	125.0

In order to calculate the force on a microbubble, firstly the pressure amplitude is obtained by using Equation 4.14, and then the radiation force on each microbubble with respect to the radial distance is investigated. For the wavelengths of 970, 596, and 578 nm, the absorption coefficients of whole blood are taken as $\mu_a = 6.9$, 44.8, and 268 cm^{-1}, respectively [10,175]. Parameters of the absorber are Γ= 0.2 with fluence F = 15 mJ/ cm^2. The density and the speed of sound are taken as $\rho = 1000$ kg/m^3 and ν_s= 1480 m/s, respectively [126,176]. Figure 4.1a shows the change of the force on the microbubbles with a diameter of 5 μm with respect to distance from the absorber. The

resonant frequencies of previously specified microbubbles are 2.2, 5.2, and 11 MHz. Figure 4.1b shows the change of the force on the bubbles with a diameter of 10 μm and resonant frequencies of 0.9, 1.9, and 4 MHz, as summarized in Table 4.2. For these graphs, the absorption coefficient of whole blood μ_a is taken as 6.9 cm^{-1}. Total damping constant is taken, δ_{tot}= 0.15 for both mircobubble types with 5 or 10 μm diameter [174].

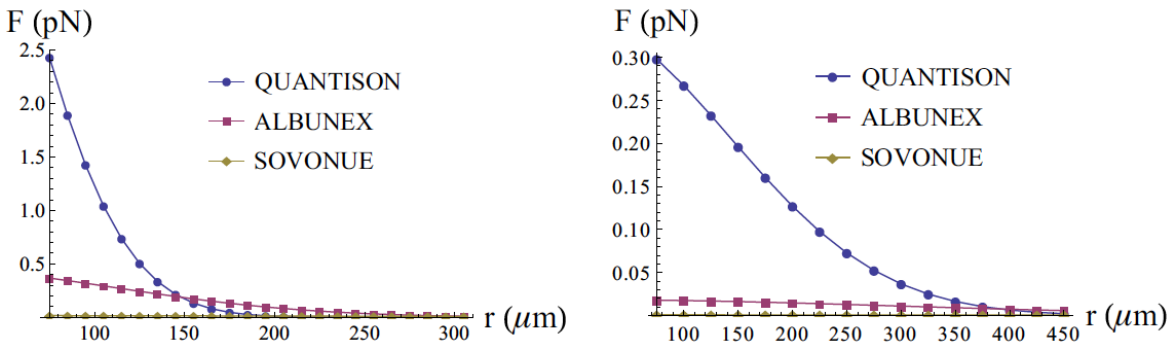

Figure 4.1. Primary radiation force F (in units of pN) on Sovonue, Albunex, and Quantison vs position r (in units of μm) for the diameters of the microbubbles (a) 5 μm with the resonant frequencies of ω_0 = 2.2, 5.2, and 11.0 MHz, respectively; and (b) 10 μm with the resonant frequencies of $\omega_0 = 0.9, 1.9$, and 4.0 MHz, respectively; where the pulse duration $\tau = \frac{1}{2\omega_0}$, the absorption coefficient of whole blood μ_a = 6.9 cm^{-1}, pulse repetition frequency v_{PRF} = 1 MHz, and beamwidth σ = 70 μm.

The results show that the force on the microbubble is decreasing with the distance between the bubble and the absorber. As can be seen from Figure 4.1 higher resonance frequency leads to a higher force. According to the Equation 4.2, the force is inversely proportional to the resonant frequency. However, adjusting the pulse duration according to the resonant frequency leads to a higher amplitude and force.

Figure 4.2, recurrently, illustrates the change of the force on the microbubbles as a function of the position of the bubbles for the same parameters except for the absorption coefficients of the whole blood that are μ_a = 44.8, and 268 cm^{-1} for wavelengths of

596 and 578 nm, respectively. Here the pulse repetition frequency and the beamwidth are $\nu_{PRF} = 1$ MHz and $\sigma = 70$ μm, respectively.

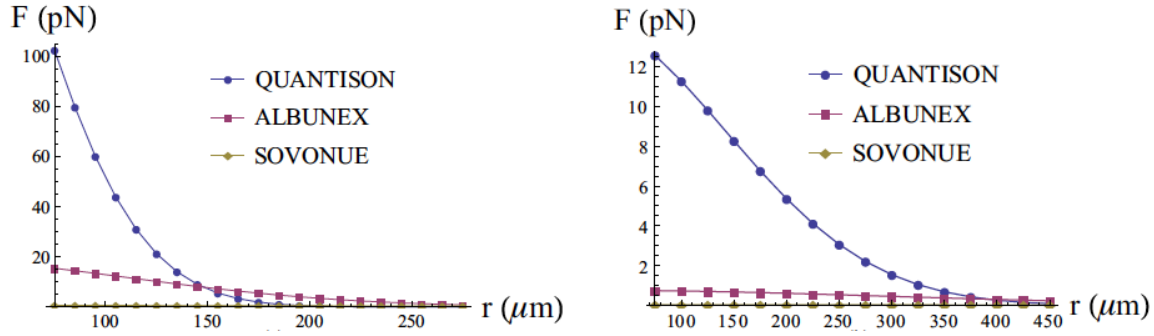

Figure 4.2. Primary radiation force F (in units of pN) on Sovonue, Albunex, and Quantison vs position r (in units of μm) for the diameters of the microbubbles (a) 5 μm with the resonant frequencies of $\omega_0 = 2.2$, 5.2, and 11.0 MHz, respectively; and (b) 10 μm with the resonant frequencies of $\omega_0 = 0.9$, 1.9, and 4.0 MHz, respectively; where the pulse duration $\tau = \frac{1}{2\omega_0}$, the absorption coefficient of whole blood $\mu_a = 44.8$ cm^{-1}, pulse repetition frequency $v_{PRF} = 1$ MHz, and beamwidth $\sigma = 70$ μm.

A comparison among Figures 4.1, 4.2, and 4.3 reveals the significant influence of the absorption coefficient on the force. Near the visible wavelength of 578 nm, the force increases dramatically. The absorption coefficient can also be increased by using contrast agents. For example, the optical absorption coefficient of whole blood for a wavelength of 800 nm is around 4 cm^{-1} but it is ten fold more than blood for ICG (43 cm^{-1}) [21]. On the other hand, it should be noted that when the absorption coefficient increases, penetration depth in tissue decreases. There is a compromise between the increase in force and penetration depth via absorption coefficient adjustment. Figure 4.2 and Figure 4.3 indicate that the force can reach to the orders of 100 and 1000 pN. Application of the force at this scale makes the manipulation and confinement of the microbubbles possible to enhance the image quality and drug delivery. At least forces of a few hundred piconewtons are needed to manipulate the microbubbles in biological applications [177,178]. In addition, considerably small forces (< 10 pN) can be utilized to measure viscoelastic properties of the microbubbles [178]. As the microbubble is

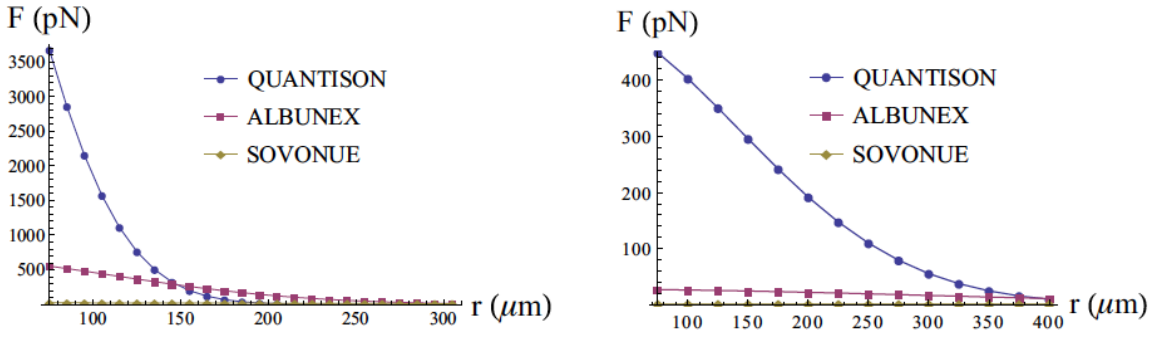

Figure 4.3. Primary radiation force F (in units of pN) on Sovonue, Albunex, and Quantison vs position r (in units of μm) for the diameters of the microbubbles (a) 5 μm with the resonant frequencies of $\omega_0 = 2.2$, 5.2, and 11.0 MHz, respectively; and (b) 10 μm with the resonant frequencies of $\omega_0 = 0.9$, 1.9, and 4.0 MHz, respectively; where the pulse duration $\tau = \frac{1}{2\omega_0}$, the absorption coefficient of whole blood $\mu_a = 268$ cm^{-1}, pulse repetition frequency $v_{PRF} = 1$ MHz, and beamwidth $\sigma = 70$ μm.

farther away from the absorber, the force decreases as expected. These results are in a good agreement with Zharov's and Hernot's experimental results [113, 129].

Pulses generated by piezoelectric transducers have repetition rates are on the order of kHz. In our case, the pulsed laser is used to create an acoustic wave by means of the photoacoustic effect. Thus, repetition rates up to the order of MHz are utilized in order to adjust the radiation force. Figure 4.4 shows the upsurge in the force as the pulse repetition rate increases from $\nu_{PRF} = 250$ kHz, 500 kHz, and 1 MHz, respectively. The effect of the beamwidth on the radiation force is also investigated at r = 75 μm for a microbubble with a diameter of 5 μm. The pulse duration of the laser is 45.4 ns matching the resonant frequency of the microbubble which is 11 MHz.

The reason for the increase in the force with the beamwidth is that the laser pulse with a large beamwidth is absorbed by the larger part of the absorber. The impact of pulse duration on the wave is also shown for various beamwidths. It is already well known that the amplitude of the photoacoustic wave decreases as the pulse duration

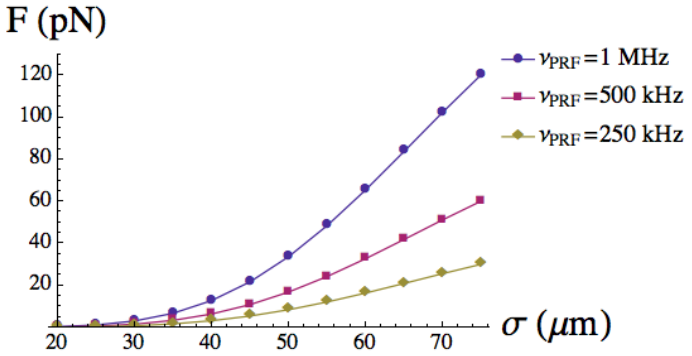

Figure 4.4. Primary radiation force F (in units of pN) on Quantison vs beamwidth σ (in units of μm) for the pulse repetition frequencies of ν_{PRF} = 250 kHz, 500 kHz, and 1 MHz, respectively; at r = 75 μm, where ω_0 = 11 MHz, the pulse duration $\tau = \frac{1}{2\omega_0}$, the absorption coefficient of whole blood is μ_a = 44.8 cm^{-1}, and the diameter of the microbubble 5 μm.

gets longer. The peak power is inversely proportional to the pulse duration if the pulse energy of the laser is constant. Therefore, shorter pulse durations yield larger wave amplitudes accompanied by a deterioration in depth resolution. In Figure 4.5, as the beamwidth decreases the signal decreases slightly because the radial profile becomes very sharp approaching a Dirac δ function. Therefore, the explicit laser parameter dependence disappears.

For a very large pulse duration, the wave diminishes since the stress and thermal confinement conditions are violated.

4.2. Photoacoustic Radiation Force on Incompressible Spheres

4.2.1. Theory

The scalar potential of the velocity field φ, can be obtained from the pressure field p_i by the following integration [128]:

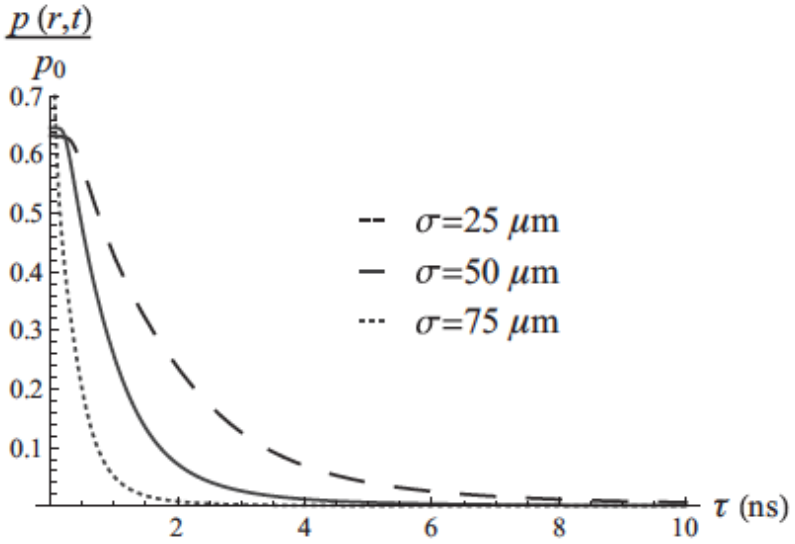

Figure 4.5. Normalized amplitude of photoacoustic wave $p(r,t)/p_0$ versus pulse duration, τ for the beamwidths σ = 25, 50, and 75 μm, where r = 100 μm.

$$\varphi(r,t) = -\frac{1}{\rho}\int p_i(r,t)dt \tag{4.3}$$

where ρ is the density of the medium. The velocity field, v_i, is the gradient the scalar potential [128],

$$\nu = \vec{\nabla}\varphi \tag{4.4}$$

Time-averaged kinetic ($\overline{V_i}$) and potential ($\overline{T_i}$) energy densities in the acoustic wave could be expressed as [124]

$$\overline{V_i} = \frac{1}{2}\rho\overline{\nu_i^2} \tag{4.5}$$

and

$$\overline{T_i} = \frac{1}{2}\frac{1}{\rho v^2}\overline{p_i^2} \tag{4.6}$$

Here v is the speed of sound in the medium, $\overline{\nu_i^2}$ and $\overline{p_i^2}$ are the time-averaged squares of the pressure and the velocity field of the acoustic wave at the point of the incompressible sphere's position and can be denoted as

$$\overline{\nu_i^2} = \frac{1}{T}\int_0^T \nu(r,t)^2 dt \tag{4.7}$$

and

$$\overline{p_i^2} = \frac{1}{T}\int_0^T p(r,t)^2 dt \tag{4.8}$$

where T is the characteristic acoustic pulse duration which is the twice of the laser pulse duration, T = 2τ. The acoustic field generates a force on the particle whose potential function can be described by the following expression [124, 129]:

$$U = 2\pi r_s^3 \rho(\frac{\overline{p_i^2}}{3\rho^2 v^2} f_1 - \frac{\overline{v_i^2}}{2} f_2) \tag{4.9}$$

where r_s is the radius of the particle, f_1 and f_2 are related to the physical parameters of speed of sound and the density of both medium and the particle that are defined as [124, 129]

$$f_1 = 1 - \frac{\nu^2 \rho}{\nu_s^2 \rho_s} \tag{4.10}$$

and

$$f_2 = 2\frac{\rho_s - \rho}{2\rho_s + \rho} \tag{4.11}$$

where ν^2 and ρ are the square of the speed of sound and the density inside the medium, respectively; ν_s^2 and ρ_s are the square of the speed of sound and the density inside the incompressible particle, respectively.

The potential function can be expressed in terms of time-averaged kinetic ($\overline{V_i}$) and potential ($\overline{T_i}$) energy densities [129]

$$U = 2\pi r_s^3 (\frac{2}{3} f_1 \overline{T_i} - f_2 \overline{V_i}) \tag{4.12}$$

The force acting on the particle can be expressed in terms of the spatial gradients of the potential, $F_1 = -\nabla \overline{T_i}$ and the kinetic energy $F_2 = \nabla \overline{V_i}$ of the acoustic field

$$F = 2\pi r_s^3 (\frac{2}{3} f_1 F_1 - f_2 F_2) \tag{4.13}$$

For force simulations, initially scalar potential of the velocity field is obtained by using the analytic expression of the pressure wave that belongs to our previous

work [159] as

$$p(r,t) = \frac{p_0\sigma^2}{4r(\sigma^2+\tau^2v_s^2)^{3/2}}\exp[-\frac{2R(r-v_st)+2(r-v_st)^2+R^2}{2\tau^2v_s^2}-\frac{R^2}{2\sigma^2}]$$
$$\times\{\sqrt{2\pi}\sigma(r-v_st)\times\mathrm{erf}[\frac{\sigma^2(-r+R+v_st)+R\tau^2v_s^2}{\sqrt{2}\tau\sigma v_s\sqrt{\sigma^2+\tau^2v_s^2}}]$$
$$\times\exp[\frac{(r+R-v_st)^2}{2\tau^2v_s^2}+\frac{\sigma^2(r-v_st)^2}{2\tau^2v_s^2(\sigma^2+\tau^2v_s^2)}+\frac{R^2}{2\sigma^2}]$$
$$+\mathrm{erf}[\frac{\sigma^2(r+R-v_st)+R\tau^2v_s^2}{\sqrt{2}\tau\sigma v_s\sqrt{\sigma^2+\tau^2v_s^2}}]\exp[\frac{\frac{(\sigma^2(r+R-v_st)+R\tau^2v_s^2)^2}{\sigma^2(\sigma^2+\tau^2v_s^2)}+(r-v_st)^2}{2\tau^2v_s^2}]]$$
$$-2\tau v_s\sqrt{\sigma^2+\tau^2v_s^2}\exp[\frac{(r-v_st)^2}{2\tau^2v_s^2}][\exp[\frac{2R(r-v_st)}{\tau^2v_s^2}]-1]\}\theta(r-\mid R-v_st\mid)\theta(-r+R+v_st) \tag{4.14}$$

From this pressure field, we obtain analytic solution for the scalar potential of the velocity distribution and the velocity field by using Equation 4.3.

Figure 4.6 shows the velocity field simulated by using Equation 4.4. Here the medium is water ($v_s = 1500$ m/s and $\rho = 1000$ kg m^{-3}) that includes trypan blue with an absorption coefficient, $\mu_a = 0.1$ cm^{-1}, the radius of the absorber is R = 5 μm. The pulse duration of the laser is 4 ns having a pulse energy of 1.5 μJ.

Regardless of the non-dimensional time, the time-averaged potential energy monotonically decreases as can be seen in Figure 4.7. For smaller non-dimensional time, the decline is sharper. The outcome of this behavior is that this component of the photoacoustic radiation force is always positive and reaches to a maximum value around the variance of the laser beam. Figure 4.8 shows normalized gradient of the potential energy for different non-dimensional times, $\tau_L = \frac{v\tau}{R} = 2.4$, 1.7, and 0.8, respectively; versus non-dimensional radial distance. Figure 4.9 shows normalized time averaged-kinetic energy, ($\overline{T_i}$) obtained analytically from scalar potential for different non-dimensional times, $\tau_L = \frac{v\tau}{R} = 2.4$, 1.7, and 0.8, respectively; versus non-dimensional radial distance.

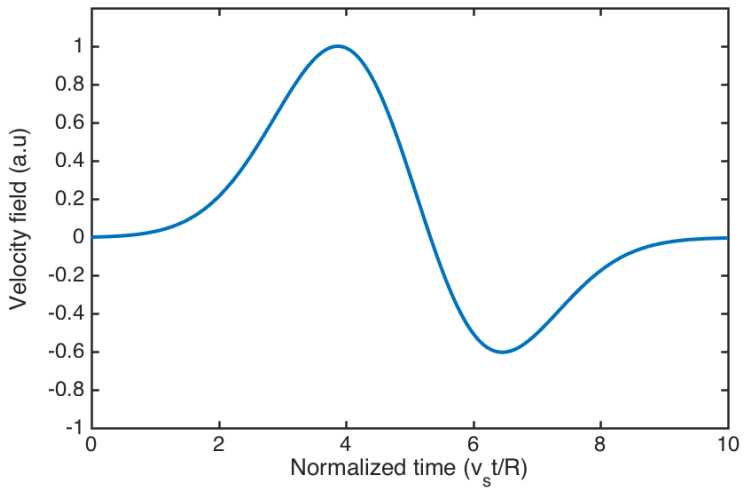

Figure 4.6. The velocity field versus normalized time ($v_s t$/R) for the medium of water (v_s = 1500 m/s and ρ = 1000 kg m^{-3}) that includes trypan blue with an absorption coefficient, μ_a = 0.1 cm^{-1}, the radius of the absorber is R = 5 μm. The pulse duration of the laser is 4 ns having a pulse energy of 1.5 μJ.

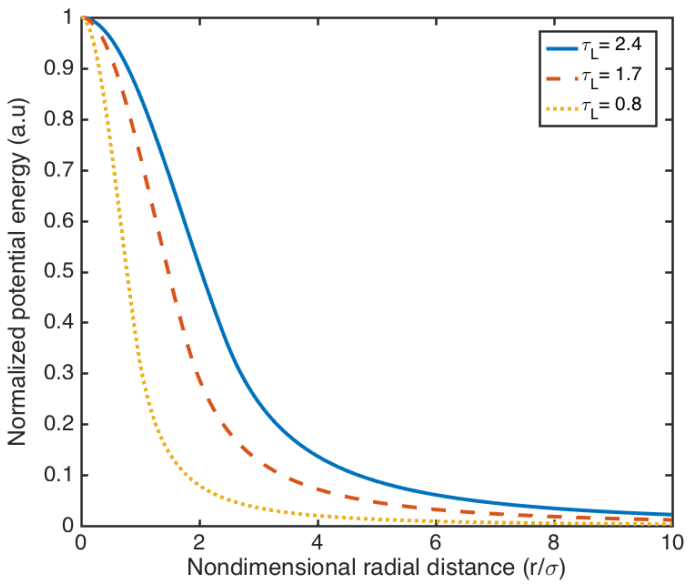

Figure 4.7. Normalized time averaged-potential energy, ($\overline{V_i}$) for normalized times, τ_L = $\frac{\nu\tau}{R}$ = 2.4, 1.7, and 0.8, respectively; versus non-dimensional radial distance (r/σ).

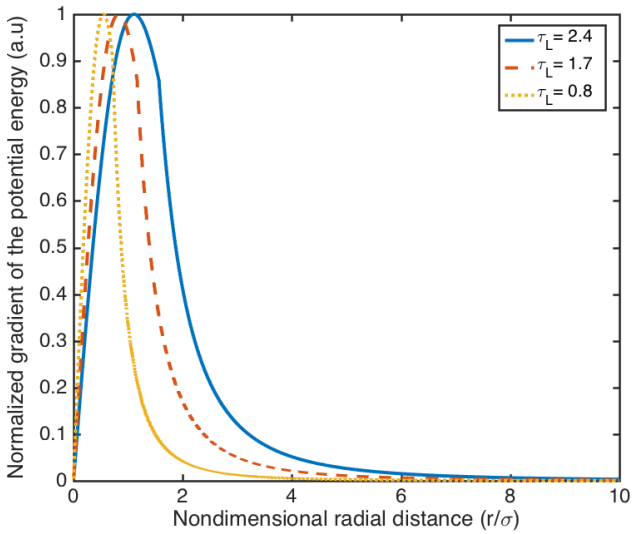

Figure 4.8. Normalized gradient of the potential energy, $(\nabla\overline{V_i})$ for different non-dimensional times, $\tau_L = \frac{v\tau}{R} = 2.4$, 1.7, and 0.8, respectively; versus non-dimensional radial distance (r/σ).

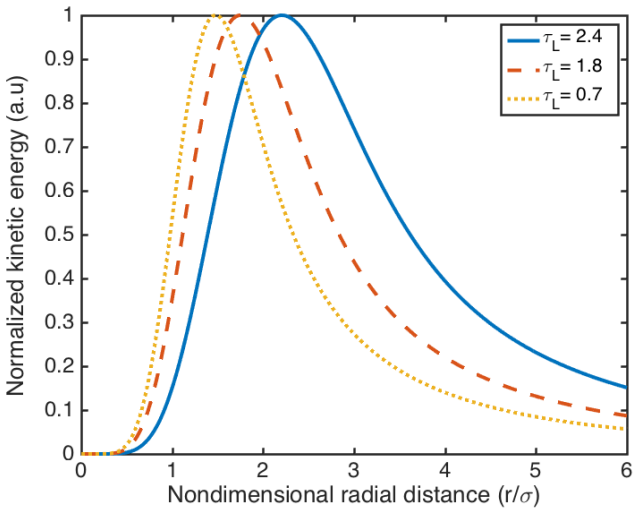

Figure 4.9. Normalized time averaged-kinetic energy acquired analytically from scalar potential for different non-dimensional times, $\tau_L = \frac{v\tau}{R} = 2.4$, 1.7, and 0.8, respectively; versus non-dimensional radial distance (r/σ).

As can be seen in Figure 4.9, the position of the maximum of kinetic energy depends on the non-dimensional time. Figure 4.10 shows normalized gradient of the kinetic energy for different non-dimensional times, $\tau_L = \frac{v\tau}{R} = 2.4$, 1.7, and 0.8, respectively; versus non-dimensional radial distance. This component of the photoacoustic radiation force reaches to its maximum value and then becomes zero.

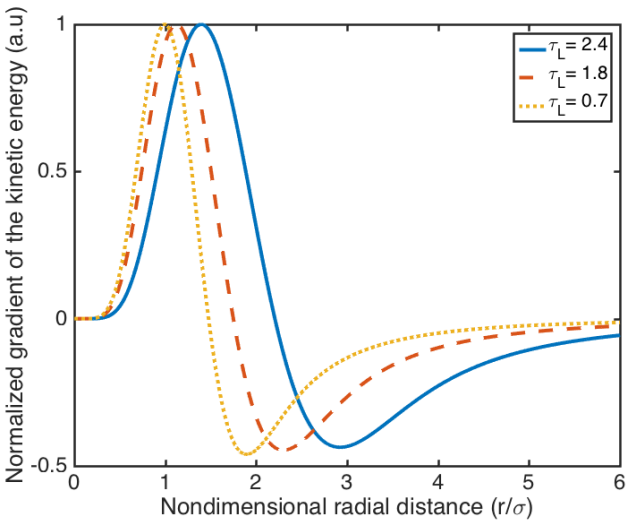

Figure 4.10. Normalized gradient of the kinetic energy for different non-dimensional times, $\tau_L = \frac{v\tau}{R} = 2.4$, 1.7, and 0.8, respectively; versus non-dimensional radial distance (r/σ).

The photoacoustic radiation force is estimated on a small silica particle with the following parameters: speed of sound inside the particle, $\nu_s = 5968$ m/s and density of the particle, $\rho_s = 2650$ kg m^{-3}, speed of sound inside the medium, $\nu = 1500$ m/s and density of the medium, $\rho = 1000$ kg m^{-3}, $f_1 = 0.9762$, $f_2 = 0.5238$, total absorption coefficient of trypan blue and the water, $\mu_a = 0.1$ cm^{-1}, the radius of the particle is $r_a = 2$ μm. The pulse duration of the laser is 4 ns with a pulse energy of 1.5 μJ. Figure 4.11 shows the force resulted from the gradient of the potential energy (blue) and kinetic energy (red) by using these variables versus radial distance (in units of μm).

By using Equation 4.13, total photoacoustic radiation force on a silica particle with a radius, $r_a = 2$ μm is evaluated and it is presented in Figure 4.12.

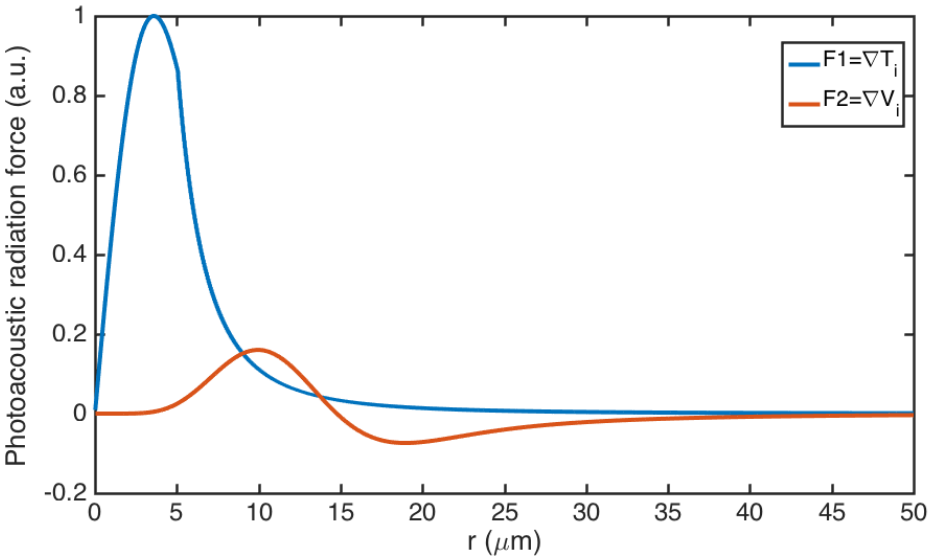

Figure 4.11. Photoacoustic radiation force (in units of pN) due to the gradient of the potential energy (blue) and kinetic energy (red) on a silica particle with a radius, r_a = 2 μm versus radial distance (in units of μm).

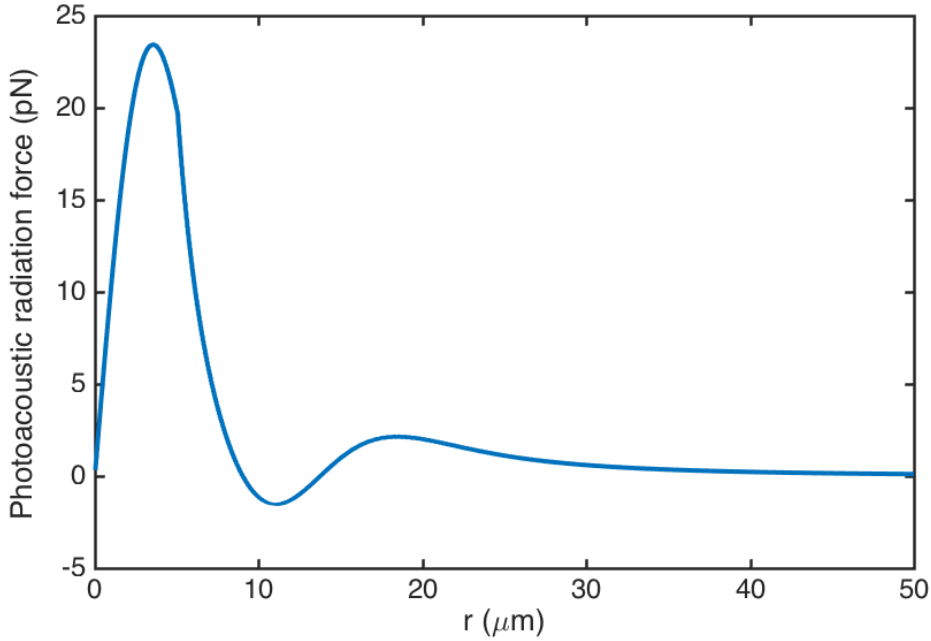

Figure 4.12. Total photoacoustic radiation force (in units of pN) on a silica particle with a radius, r_a= 2 μm versus radial distance (in units of μm).

For these parameters, there is a strong repulsive force up to a radial distance of 9 μm, the force is attractive in between 9-16 μm and finally becomes a weak repulsive force and then vanishes. The position of the attraction and the amplitude of the photoacoustic radiation force depend on medium, particle and excitation parameters. In some cases, the force is only repulsive.

4.2.2. Experiments

For experimental studies, silica particles with various diameters, (1, 2 and 4 μm) and polystyrene beads (diameter, 4 μm) were used. The particles were suspended in a solution consisting 1-67 % trypan blue to increase absorption. These objects were placed in a cavity between the microscope slide and the cover slip. The laser beam was focused with a 100x oil immersion objective. The position of the laser focus in the x-y plane was fixed, controllable in the z, the relative position of particles was adjusted with the microscopy stage on the same plane.

The photoacoustic waves were monitored with the presence of a water immersion transducer with a central frequency of 3.5 MHz upon the microscope slide. Figure 4.13 shows the position of the transducer contacted to the microscope slide with an ultrasound gel to prevent impedance mismatch between the glass and the air.

We showed that it is possible to move particles with the photoacoustic radiation force. Silica beads with diameters of 4 μm and density, $p_s = 2650$ kg/m^3 are used for this experiment. Figure 4.14a shows the positions of particles just after the laser shot (532 nm, pulse energy around 1.5 μJ), Figure 4.14b shows the positions after 3 frames, with a video recording of 15 frames/s that corresponds to 0.2 seconds later.

Green and red arrows show the initial and final positions of silica particles. Remote particles (farther from 25 μm) were not affected by the photoacoustic radiation force as theoretical studies show that the magnitude of the force around these distances is insignificant.

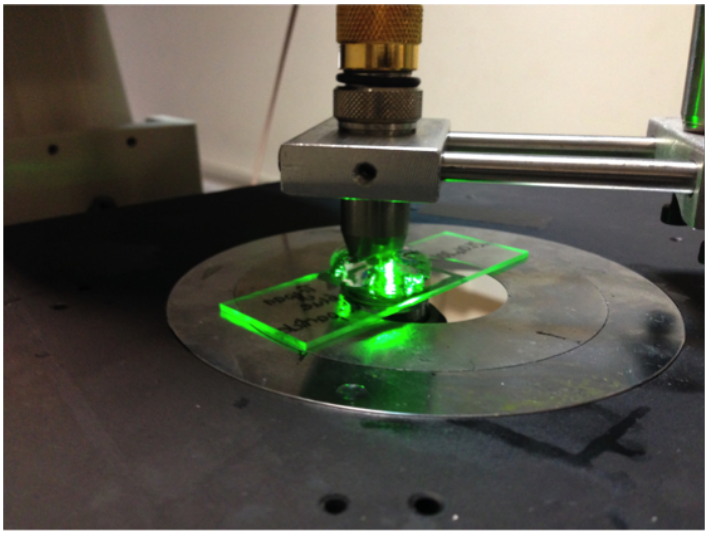

Figure 4.13. Acoustic wave monitoring via a 3.5 MHz transducer contacted to a microscope slide with an ultrasound gel to prevent impedance mismatch between glass and air.

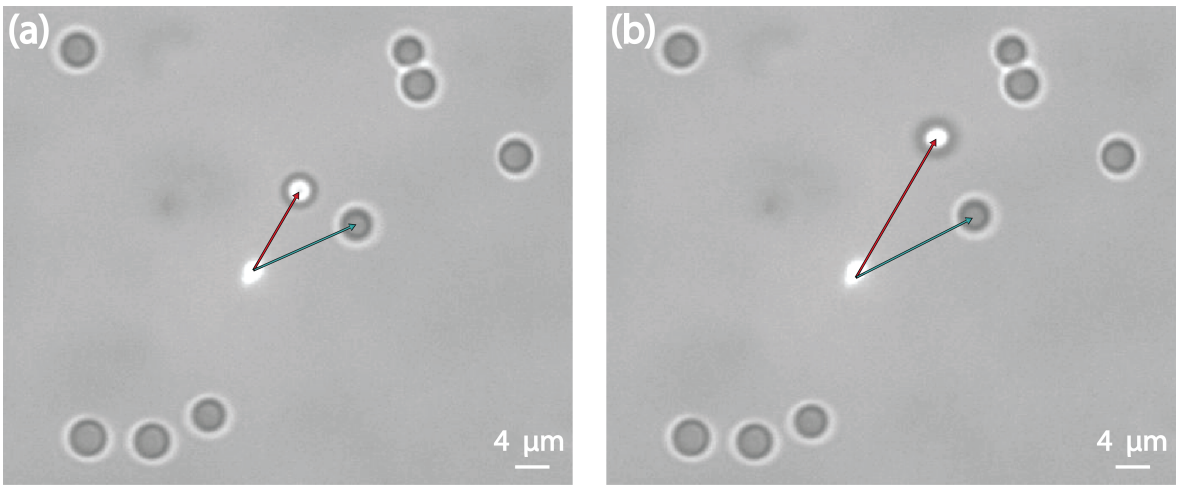

Figure 4.14. The position of silica particles with diameters of 4 μm a) just after b) 3 frames later than the laser shot (λ = 532 nm; pulse duration, 8 ns; energy, 1.5 μJ; beam diameter, $\sim$ 2 μm) in a solution of 67% trypan blue. Bright spot belongs to the position of the laser beam.

Our simulation studies showed that the force is repulsive for the relative distance between the laser focus and the particle is in the range of 2.5-7.5 μm, attractive between 7.5-10 μm and repulsive for the rest but with a very small magnitude. Figure 4.15a shows the positions silica particles just before the laser shot ($\lambda = 532$ nm; pulse duration, 8 ns; energy, 1.5 μJ; beam diameter, ~ 2 μm). Figure 4.15b displays separation of four attached particles that are very close to the focal spot of the laser beam. At these distances attractive photoacoustic radiation force is in action, as can be seen in Figure 4.15c and Figure 4.15d particles get close to the focus, then they start to move away with the effect of repulsive photoacoustic radiation force that can be seen in Figure 4.15d and Figure 4.15f. All the pictures here are snapped with an interval of 3 frames. Because of the relatively slow CCD camera ($<$ 24 frames/s), it can not capture the speedily moving particles and some of them seem blurred.

In the other set of experiments, silica beads with diameters of 2 μm and density, $p_s = 2650$ kg/m^3 are used. Figure 4.16a shows the positions of particles just before the laser shot (532 nm, pulse energy around 1.5 μJ), Figure 4.16b, 4.16c, and 4.16d show the positions after 5 frames from each other, with a video recording of 15 frames/s that corresponds to 0.33 seconds later.

Green and red arrows show the positions of silica particles at each frame. A very similar experiment is conducted on red blood cells to illustrate that cells can also be manipulated. Figure 4.17a shows the positions of particles just before the laser shot (532 nm, pulse energy around 1.5 μJ), Figure 4.17b, 4.17c and 4.17d show the positions after 2 frames from each other. It is observed that membrane of cells rupture when they intersect with the laser beam. Bright spot belongs to the laser beam which is scattered by the constituents of the blood.

An analysis regarding the effect of repetition rate of chopper is conducted. Thus, the affect of bursts on the motion of the particle is also performed. Figure 4.18 shows the general scheme for bursts generated with a chopper that operates in between 10-80 Hz for the fiber laser that has a repetition rate of 65 kHz. In the Figure 4.18, the time

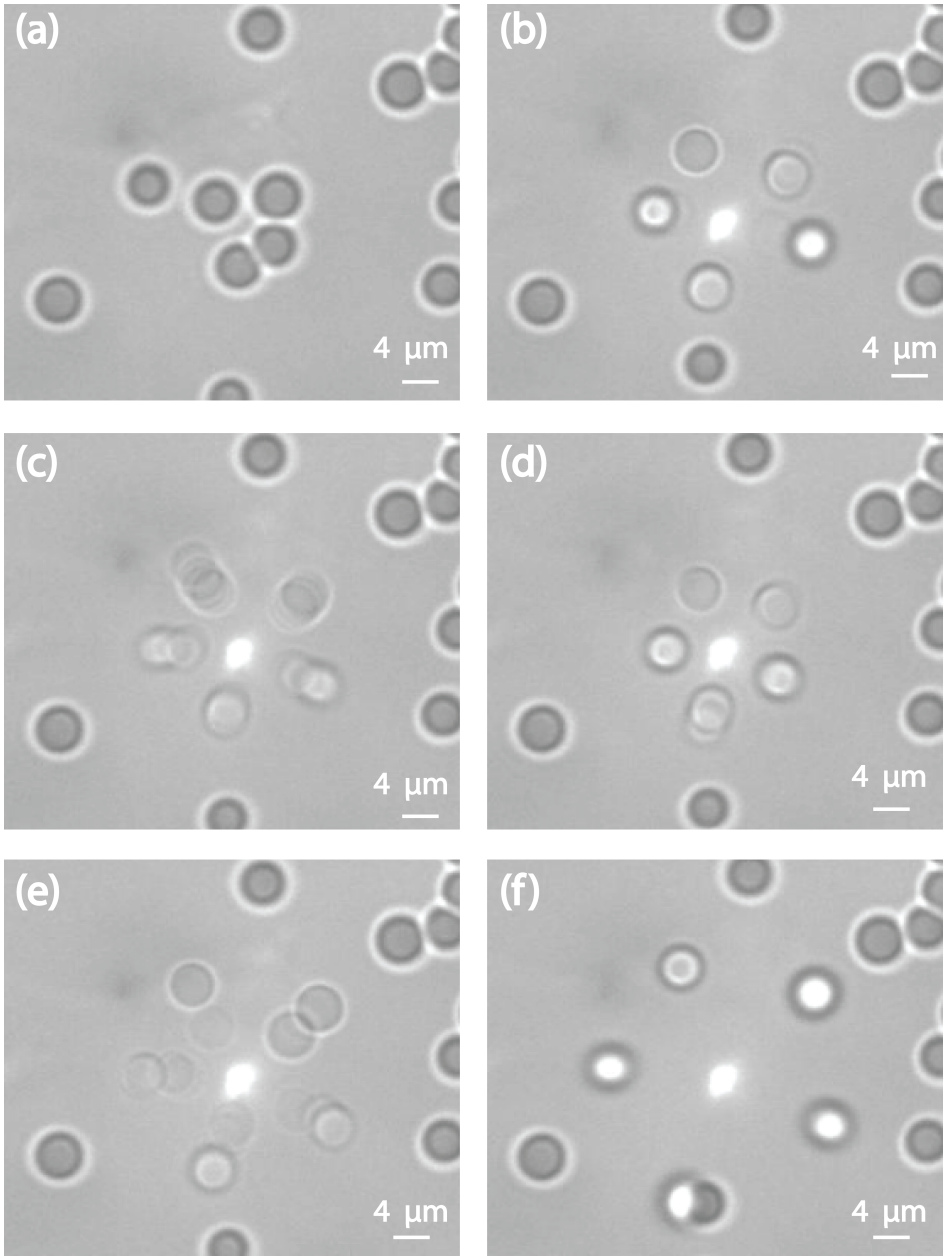

Figure 4.15. a) The positions of silica particles just before the laser shot ($\lambda = 532$ nm; pulse duration, 8 ns; energy, 1.5 μJ; beam diameter, ~ 2 μm), b) separation of four attached particles with repulsive photoacoustic radiation force c) and d) getting particles close to the focus with the effect of attractive photoacoustic radiation force d) and f) departing of particles with the effect of repulsive photoacoustic radiation force.

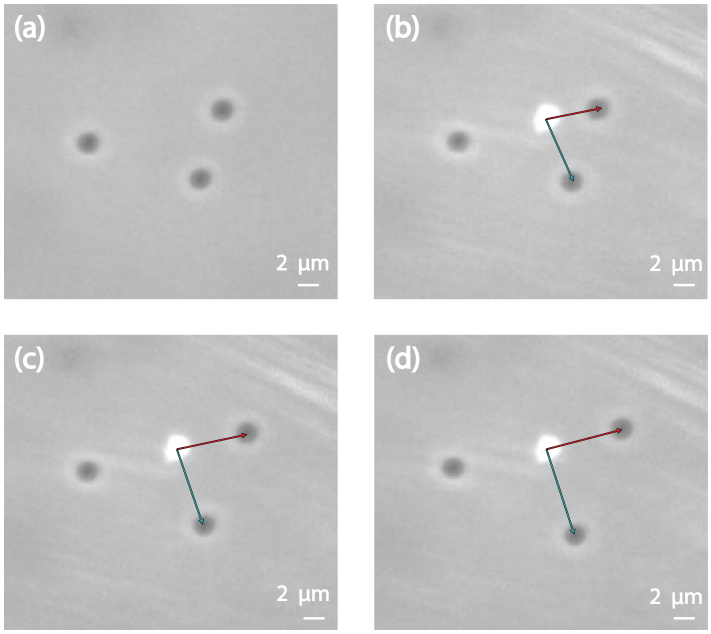

Figure 4.16. The positions of silica particles with diameters of 2 μm a) just before the laser shot (λ = 532 nm; pulse duration, 8 ns; energy, 1.5 μJ; beam diameter, $\sim$ 2 μm) b), c), and d) 5 frames later than each other in a solution of 67% trypan blue.

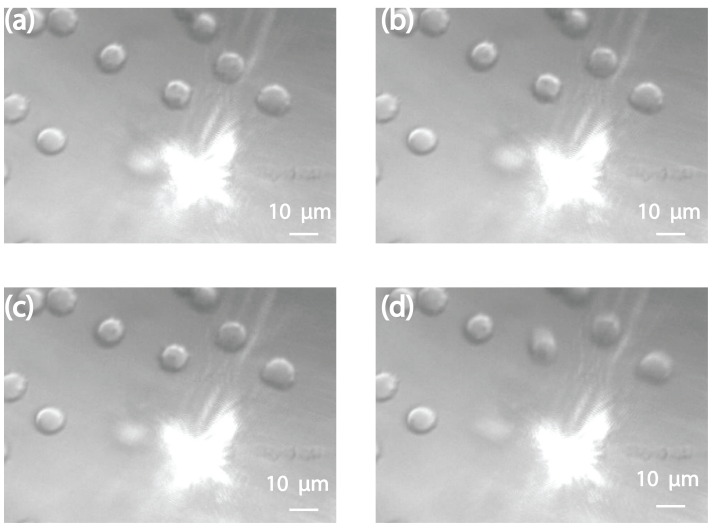

Figure 4.17. The positions of red blood cells a) just after the laser shot (λ = 532 nm; pulse duration, 8 ns; energy, 1.5 μJ; beam diameter, $\sim$ 4 μm) b), c), and d) 2 frames later than each other in their serum.

difference between bursts (top) depends on the repetition rate of chopper and time difference between intra-burst peaks (bottom) are determined by the fiber laser.

Figure 4.19 shows the displacement of particle (in units of μm) versus repetition rate of chopper (in units of Hz).

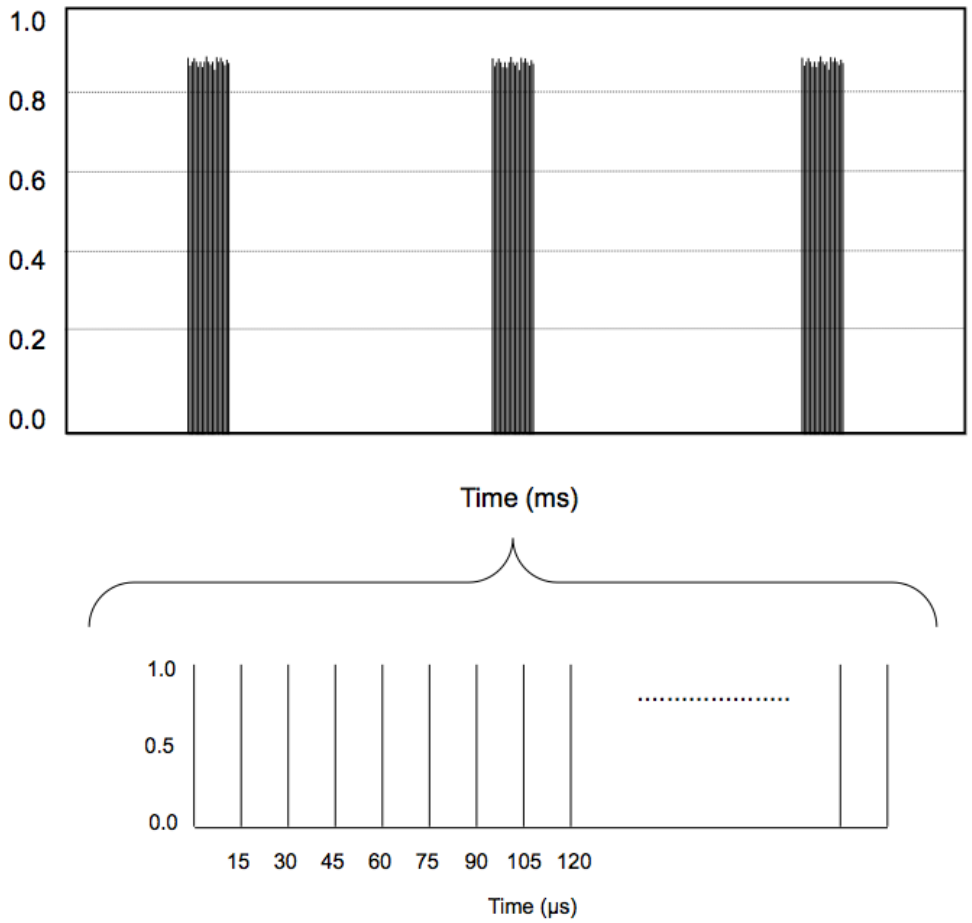

Figure 4.18. General scheme for bursts generated with a chopper that operates in between 10-80 Hz for the fiber laser that has a repetition rate of 65 kHz. Top: the time difference between bursts (depends on the repetition rate of chopper), bottom: time differences between intra-burst peaks.

As can be seen, from Figure 4.19 as the number of individual peaks increases in the burst, the distance that the particle can travel also increases. Working in the burst mode may increase the sensitivity in detection of photoacoustic radiation forces.

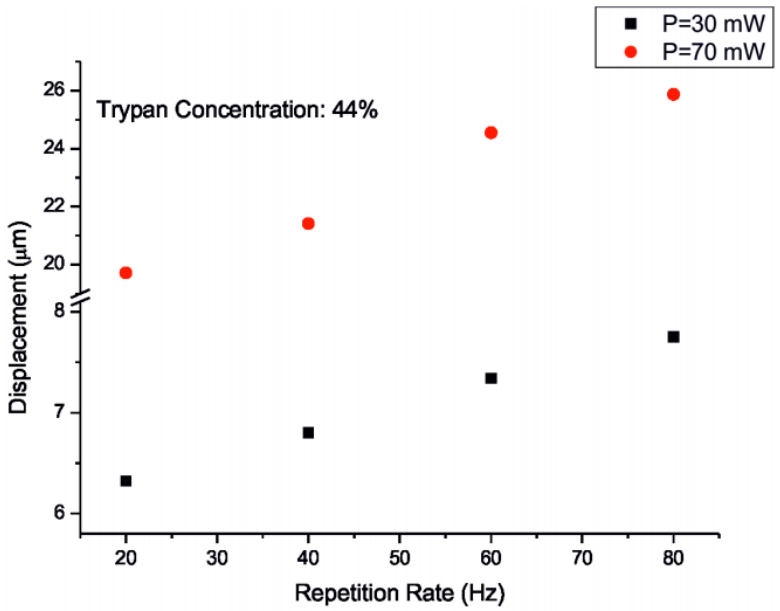

Figure 4.19. The displacement of particle (in units of μm) versus repetition rate of the chopper (in units of Hz).

5. HYBRID OPTICAL TWEEZERS AND PHOTOACOUSTIC MICROSCOPY SYSTEM

In the hybrid optical tweezers and photoacoustic microscopy system, trapped particle is used to detect photoacoustic waves. In this sense, it is critical to understand the dynamics and the calibration techniques of optical tweezers. The following sections includes these know-hows.

5.1. Optical tweezers

The motion of a Brownian particle is slower than the atoms of the fluid that it is immersed in when the dimension of the particle is larger than those atoms. This motion is a result of random collisions with the atoms of the fluid because of density fluctuations [179]. Time scales in a colloidal system vary, for instance the relaxation time for the Brownian particle, *i.e.*, the momentum relaxation time is expressed as following:

$$\tau_m = \frac{m}{\gamma} \tag{5.1}$$

where γ is the particle friction coefficient for a spherical particle of radius R moving in a fluid with viscosity η, is determined by Stokes' law [179]

$$\gamma = 6\pi\eta R \tag{5.2}$$

For a particle with radius $R = 1$ μm, mass $m = 11$ pg, in water with viscosity η =0.001 N s m^{-2} at room temperature, momentum relaxation time is $\tau_m = 0.6$ μs [180].

The relaxation time for the Brownian particle, *i.e.*, the time that the particle have diffused its own radius is defined as [179]

$$\tau_m = \frac{R^2}{D} \tag{5.3}$$

where D is the diffusion coefficient as defined [180]

$$D = \frac{k_B T}{\gamma} \tag{5.4}$$

For a particle with radius $R = 1$ μm in water with viscosity $\eta = 0.001$ N s m^{-2} at room temperature, the relaxation time for the Brownian particle is $\tau_r = 5$ s [180]. In general,

$$\tau_m << \tau_r \tag{5.5}$$

The equation of the motion of the particle in a viscous fluid can be described by the following Langevin equation [180]:

$$m\frac{\partial^2}{\partial t^2}r(t) = -\gamma\frac{\partial}{\partial t}r(t) + \chi(t) \tag{5.6}$$

where $\chi(t)$ is the random fluctuation force with zero mean, i.e., $\langle\chi(t)\rangle = 0$. When there is a potential, $U(r)$, such as the presence of an optical trap, Equation 5.6 becomes [180]

$$m\frac{\partial^2}{\partial t^2}r(t) = -\frac{\partial}{\partial r}U(r) - \gamma\frac{\partial}{\partial t}r(t) + \chi(t) \tag{5.7}$$

here, the force acting on the particle is $F(r) = -\frac{\partial}{\partial r}U(r)$, under such a potential.

The *Reynolds number* is defined as the ratio of the inertial forces to the viscous forces [180]

$$R_e = \frac{Inertial\,Force}{Viscous\,Force} = \frac{Rv\rho}{\eta} \tag{5.8}$$

In the low *Reynolds number* regime, viscous force dominates. The inertial term can be ignored in the low Reynolds number regime, then Equation 5.7 becomes

$$\frac{\partial}{\partial t}r(t) = -\frac{1}{\gamma}\frac{\partial}{\partial r}U(r) + \xi(t) \tag{5.9}$$

Here $\xi(t) = \sqrt{2D}W(t)$, where $W(t)$ is the white noise [180].

For a 3D optical trap, Equation 5.9 can be utilized to express Langevin equation for each dimension as following [180]:

$$\begin{aligned}
\frac{dx(t)}{dt} &= -\frac{\kappa_x}{\gamma}x(t) + \sqrt{2D}W_x(t) \\
\frac{dy(t)}{dt} &= -\frac{\kappa_y}{\gamma}y(t) + \sqrt{2D}W_y(t) \\
\frac{dz(t)}{dt} &= -\frac{\kappa_z}{\gamma}z(t) + \sqrt{2D}W_z(t)
\end{aligned} \tag{5.10}$$

where x and y represent the position of the particle in a plane that is perpendicular to the beam propagation direction z, k_x, k_y, and k_z are the stiffness of trap in that direction, $W_x(t), W_y(t)$, and $W_z(t)$ are independent white noises.

5.2. Calibration Techniques

For calibrating an optical trap, the traditional approach is to determine the stiffness of the trap [181], and hence the force which is proportional to the stiffness and displacement of the trapped particle with respect to the center of the trap can be determined. Calibration is also important in determining the conversion factor, β, to transform measurement units into real displacements. Generally, these units are pixels (*e.g.*, for CCD) and volts (*e.g.*, for QPD) that are required to be converted to determine absolute positions [180].

Various techniques can be employed to perform calibration. There are passive and active calibration techniques. In the passive ones, trajectory of the particle is measured inside a fixed trap whereas in the active ones, the effect of a known force is examined on the trapped particle. Passive techniques include the potential analysis, the equipartition method, the mean square displacement analysis, the autocorrelation function analysis and the power spectrum analysis and these techniques will be explained in the following sections [182–184].

5.2.1. Potential Analysis

The trapped particle is in thermal equilibrium with the molecules of fluid that behaves as a heat-bath, therefore Maxwell-Boltzmann distribution gives the probability distribution of the trapped particle inside a potential as following [184]:

$$p(x) = \frac{exp(\frac{-U(x)}{k_B T})}{\int_a^b exp(\frac{-U(x)}{k_B T})dx} \tag{5.11}$$

By solving Equation 5.11, the expression for $U(x)$ can be obtained [182]

$$-U(x) = k_B T log[p(x)] + U_0 \tag{5.12}$$

Utilizing the histogram of the position, probability distribution, $p(x)$ can be approximated, and then the trapping potential $U(x)$ can be acquired.

Figure 5.1a shows the position histograms of a silica particle with a diameter of 1 μm trapped inside water by a laser diode operating at 976 nm wavelength with a power of 10 mW at the sample. Figure 5.1b shows the acquired potential by using Equation 5.12.

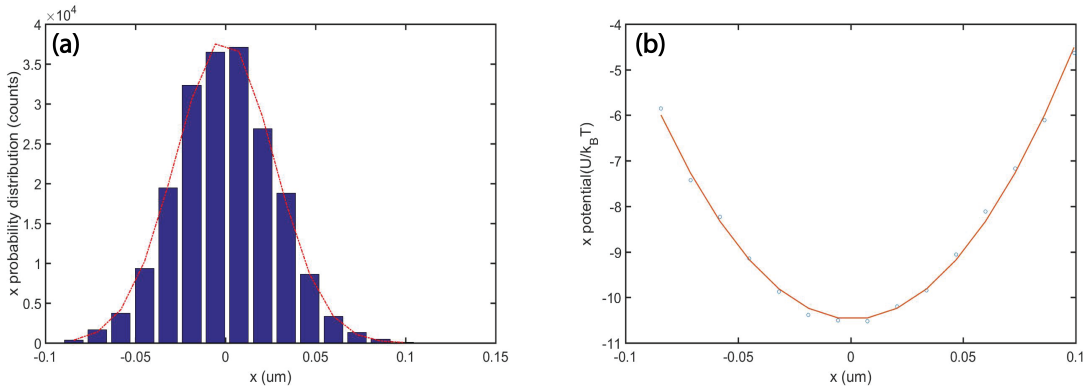

Figure 5.1. a) The position histogram, b) potential corresponding to an optically trapped silica particle with a diameter of 1 μm by a 2.3 mW laser power.

In the presence of harmonic potential, the probability distribution is Gaussian, whenever the potential is not harmonic, the distribution can be used to characterize the potential by using Equation 5.12. However, this method has some drawbacks such as low-frequency noise appear in the wings of the histogram and may overspread the distribution [184].

5.2.2. Equipartititon Theorem

A trapped particle makes thermal fluctuations and moves continuously because of the heat of solution. The fluctuations are balanced with potential which can be assumed as harmonic [182]

$$U(x) = \frac{1}{2}\kappa_x([x - x_{eq}])^2 \tag{5.13}$$

where κ_x is the trap stiffness, x is the displacement of the particle from its trapped equilibrium position, x_{eq}. The potential variance can thus be used to calibrate the optical tweezers. Langevin equation with this assumption becomes [180]

$$\frac{dx(t)}{dt} = -\kappa_x[x(t) - x_{eq}] + \sqrt{2D}W_x(t) \tag{5.14}$$

By using Equation 5.11, the probability distribution becomes Gaussian

$$p(x) = p_0 exp(-\frac{[\kappa_x([x - x_{eq}])^2]}{2k_BT}) \tag{5.15}$$

The equipartition theorem that states every degree of freedom has an average energy of $\frac{1}{2}k_BT$, which makes the following equation applicable: [183]

$$\langle U(x)\rangle = \frac{1}{2}\kappa_x\langle([x - x_{eq}])^2\rangle = \frac{1}{2}k_BT \tag{5.16}$$

For sufficient number of independent data points, x_l, (that do not need to be acquired at fixed intervals), the position variance is estimated as [180]

$$\sigma_x^{2,(ex)} = \frac{1}{L}\sum_{i=1}^{L}(x_l - x_{eq}^{(ex)})^2 \tag{5.17}$$

and the trap stiffness by following:

$$\kappa_x^{(ex)} = \frac{k_B T}{\sigma_x^{2,(ex)}} \tag{5.18}$$

The method is advantageous in that stiffness can be determined without the need to know the shape of the particle and the viscosity of the medium. The parameters affect the distribution implicitly. Yet, the approach is prone to errors since low-frequency noise increases the overall variance, and may decrease the stiffness. The errors can be reduced by repeating the experiments and averaging the results [185].

5.2.3. Mean Squared Displacement Analysis

It is also possible to calibrate the optical trap by mean squared displacement (MSD) analysis. The MSD which is a quantification of a particle's movement from its initial position is given by [180]

$$MSD_x = \overline{(x(t+\tau) - x(t))^2} \tag{5.19}$$

where $\tau_{ot_x} = \frac{\gamma}{\kappa_x}$ is the trap characteristic time. For short times, $\tau << \tau_{ot_x}$ MSD is linearly proportional to t as in the free diffusion case and for long time scales, $\tau >> \tau_{ot_x}$ within the confinement of the optical trap it reaches a plateau. In this situation, MSD can be related to the position autocorrelation function [182]

$$MSD_x = 2\sigma_x^2 - 2\langle x(t)x(t+\tau)\rangle \tag{5.20}$$

σ_x^2 is the variance of the displacement data set, the angle brackets represent averages over all time values. MSD takes the following form for timescales much longer than the inertial time scale [180]

$$MSD_x = 2\frac{k_B T}{\kappa_x}(1 - \exp^{-\frac{|\tau|}{\tau_{ot_x}}}) \tag{5.21}$$

The diffusion coefficient can also be extracted from the analysis. Data acquired from experiments is not in the units of lengths, it is pixel for CCD and voltage for QPD. It is necessary to obtain a conversion factor

$$S_x^{(ex)} = \sqrt{\frac{\gamma}{\gamma^{(ex)}}} \tag{5.22}$$

where $\gamma^{(ex)}$ is the experimental friction coefficient acquired from fitting. Figure 5.2 shows MSD for a trapped silica particle with 2.3 mW laser power in the absence of an external sound source.

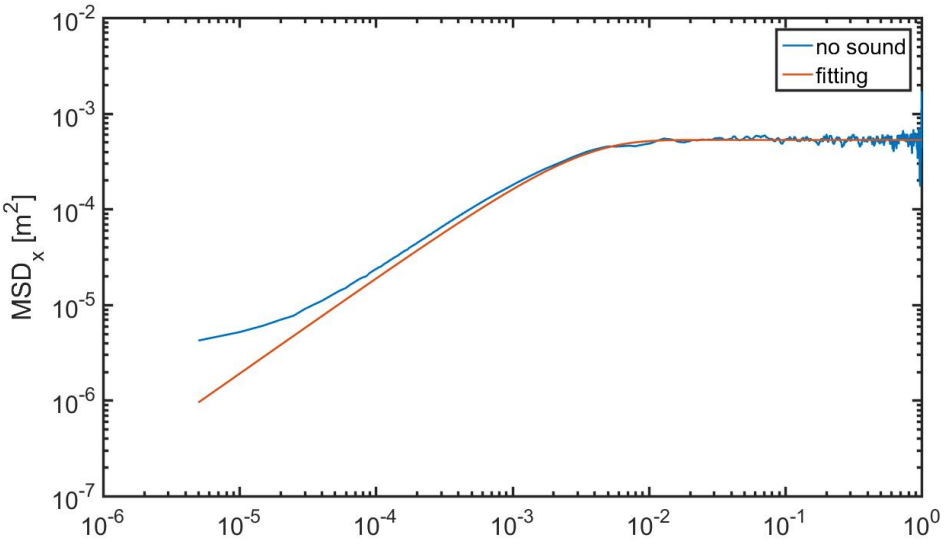

Figure 5.2. Mean square displacement analysis corresponding to an optically trapped silica sphere with a diameter of 1 μm by a 2.3 mW laser power in the absence of a sound source.

5.2.4. Autocorrelation Analysis

Another data analysis tool for calibration of optical tweezers is the autocorrelation function (ACF). This method measures the bead's position with respect to itself after a later time, and it is an indicator of the required time for the particle to be uncorrelated from its initial position. It can be calculated as [182]

$$C_x(\tau) = \langle x(t)x(t+\tau)\rangle \tag{5.23}$$

Here the angle brackets represent an average over all times, t, and τ is the lag time. Evaluation of the Equation 5.24 gives [180]

$$C_x(\tau) = \frac{k_B T}{\kappa_x}(\exp^{-\frac{|\tau|}{\tau_{otx}}}) \tag{5.24}$$

For $\tau >> \tau_{ot_x}$, the positions that are measured sufficiently far enough in time are independent of each other. This technique is very useful when worked with non-spherical particles [182]. Figure 5.3 shows ACF for a trapped silica particle with 2.3 mW laser power without any external sound source.

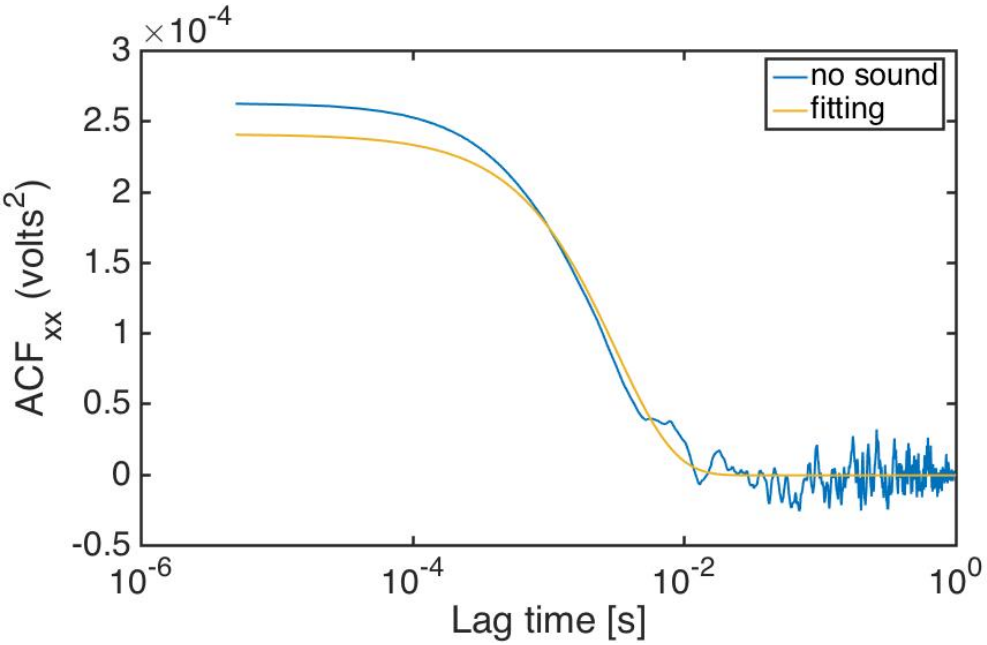

Figure 5.3. Autocorrelation function analysis belongs to an optically trapped silica sphere with 2.3 mW laser power in the absence of a sound source.

5.2.5. Power Spectrum Analysis

Power spectrum distribution (PSD) is considered as the most reliable method for calibration of an optical tweezers. Its advantage is a result of working in the frequency domain. Mechanical drifts and electrical noise can clearly be identified since they appear as peaks in the spectrum. PSD gives the power of the motion that contributes

to each frequency [185]. The Langevin equation of motion can be redesigned as [180]

$$\frac{dx(t)}{dt} + 2\pi f_{c,x} x(t) = \sqrt{2D} W_x(t) \tag{5.25}$$

by introducing the corner frequency,

$$f_{c,x} x(t) = \frac{\kappa_x}{2\pi\gamma} \tag{5.26}$$

Taking the Fourier transform, Equation 5.25 becomes [182]

$$2\pi(f_{c,x} - if)\tilde{X}(f) = \sqrt{2D}\tilde{W}_x(f) \tag{5.27}$$

where $\tilde{X}(f)$ and $\tilde{W}_x(f)$ are Fourier transforms of $X(t)$ and $W_x(t)$. By squaring the modulus of Equation 5.27, the particle's movements are expressed in terms of a power spectrum [180]

$$P_x(f) = |\tilde{X}(f)|^2 = \frac{\frac{D}{2\pi^2}}{f_{c,x}^2 + f^2} \tag{5.28}$$

where D is the diffusion coefficient.

It is required to obtain a conversion factor to transform acquisition units to length

$$S_x^{(ex)} = \sqrt{\frac{D^{(ex)}}{D}} \tag{5.29}$$

Figure 5.4 shows PSD for a trapped silica particle with 2.3 mW laser power without any sound source inclusion.

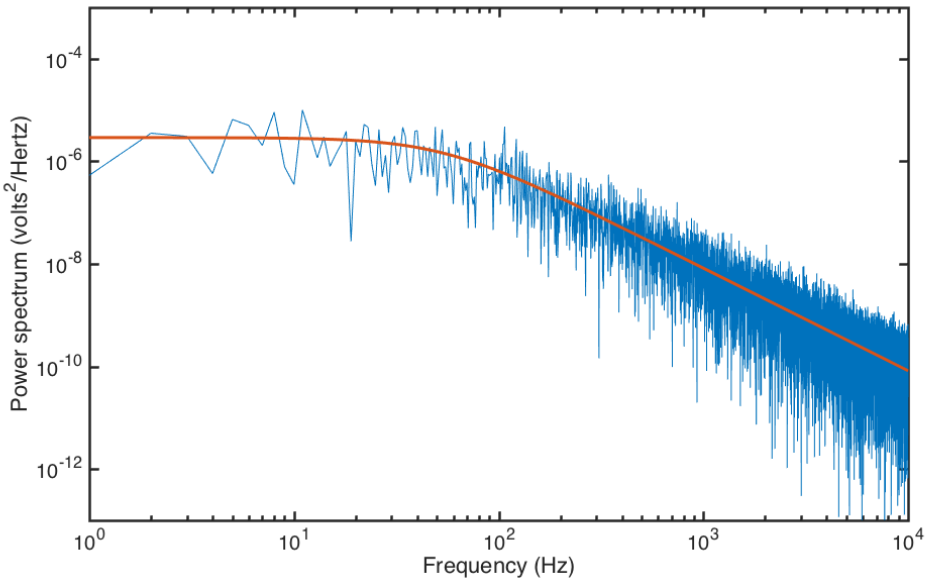

Figure 5.4. Power spectrum analysis belongs to an optically trapped silica sphere with a diameter of 1 μm by a 2.3 mW laser power in the absence of a sound source.

5.3. Sound Wave Detection via Optical tweezers System

The optical setup based on an inverted bright-field microscope coupled with a diode laser operates at 976 nm to trap silica particles. The laser beam is broadened by a telescope built with two plano-convex lenses to overfill the back aperture of an oil-immersion microscope objective (Nikon 100x, NA 1.3). The positions of the trapped particle are recorded with a CCD camera at 25 frames per second with sound switched off and on. The back reflected light from the trapped particle is also collected with a QPD for more sensitive acquisition. The translational stage of the microscopy body is used to move particles with respect to the objective. As a sound source, an earplug drived by a function generator is used. By this way, the frequency and the amplitude of the sound wave is controlled. A petri dish with a base plate of thickness 170 μm

is used as a vessel to suspend particles and to place the earplug. Figure 5.5 is the photograph that shows the location of earplug inside a petri dish.

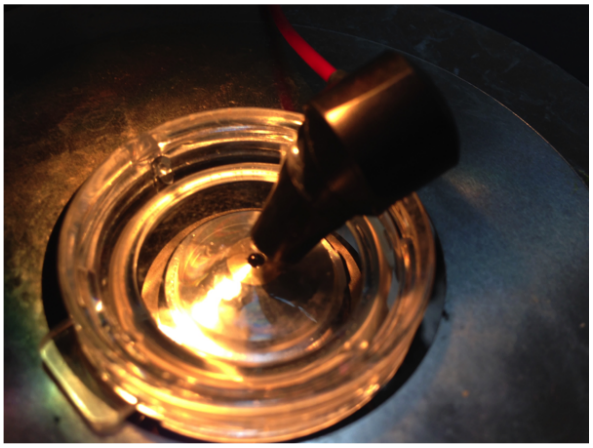

Figure 5.5. The photograph showing the location of the earplug inside a petri dish.

5.3.1. Results of the Earplug Experiments

The trajectory of the x displacement of a trapped particle was tracked with QPD with the sound off and on, respectively; and analyzed. Figure 5.6a displays the voltage values that can be converted to the particle positions in the absence of any sound. Figure 5.6b, Figure 5.6c, and Figure 5.6d show the voltage values acquired through an oscilloscope when there exists a sound wave with 300, 500, and 1000 Hz frequency, respectively.

In the condition that no sound wave is present the position of the particle randomly fluctuates in time around its equilibrium position. In the presence of a sound wave, the particle explores mostly the edges of the potential well. As the frequency of the sound wave increases the change from opposite edges becomes more frequent. Figure 5.7a exhibits Fourier transformation of the trajectory of a particle when sound is off. Figure 5.7b, Figure 5.7c, and Figure 5.7d show the trajectory in the frequency domain when a sound wave is generated with 300, 500, and 1000 Hz frequency, respectively.

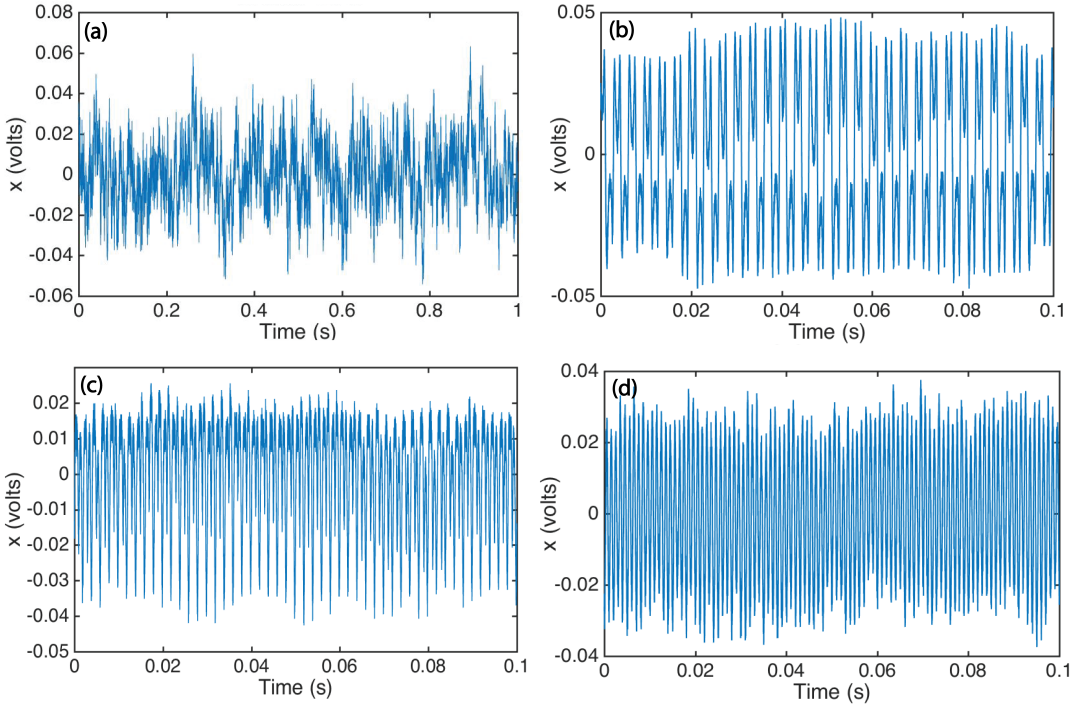

Figure 5.6. Positions of particle (from QPD) versus time, when there is a) no sound, a sound wave with b) 300, c) 500, and d) 1000 Hz frequency.

Further analysis was made in the frequency domain, as well. In the trajectories recorded with no sound, all possible frequencies were observed in the Brownian motion of the particle with a peak on its angular frequency.

When the sound is on, peaks at the frequency of the sound source emerged, and if the amplitude of the sound wave was high enough, as in the case of 300 Hz harmonics of the frequencies could also clearly be seen.

Several analyses were also performed including mean square displacement, autocorrelation function and power spectrum analysis. Figure 5.8a, Figure 5.8b, Figure 5.8c, and Figure 5.8d belong to the graphs of mean square displacement analysis when there is a sound wave with 100, 300, 500, and 1000 Hz frequency, respectively.

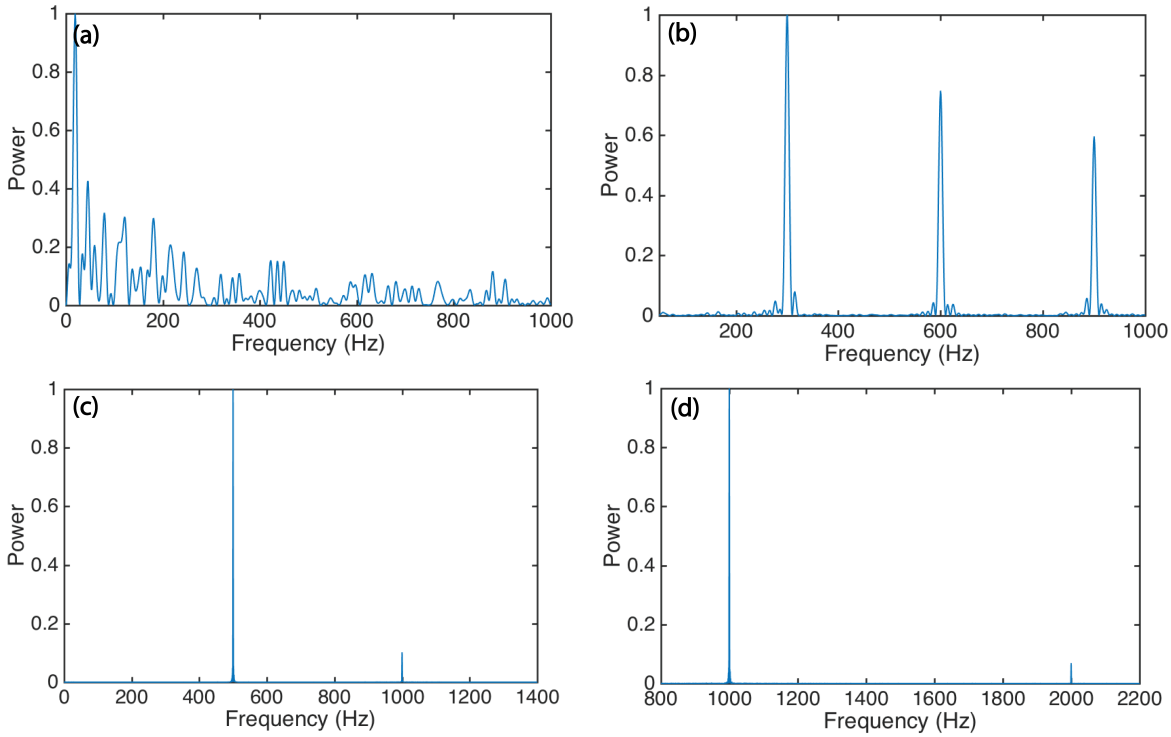

Figure 5.7. Fourier transformation of the trajectory of a particle, when there is a) no sound, a sound wave with b) 300, c) 500, and d) 1000 Hz frequency.

As distinct from no sound case (Figure 5.2), at the climb of the graphs there were undulations due to the force applied by the sound wave that compelled the particle to visit mainly the borders of the potential well. The raise in the frequency of the sound wave brought about the change from opposite edges more frequent.

Figure 5.9a, Figure 5.9b, Figure 5.9c, and Figure 5.9d demonstrate the graphs of autocorrelation function analysis when there is a sound wave with 100, 300, 500, and 1000 Hz frequency, respectively.

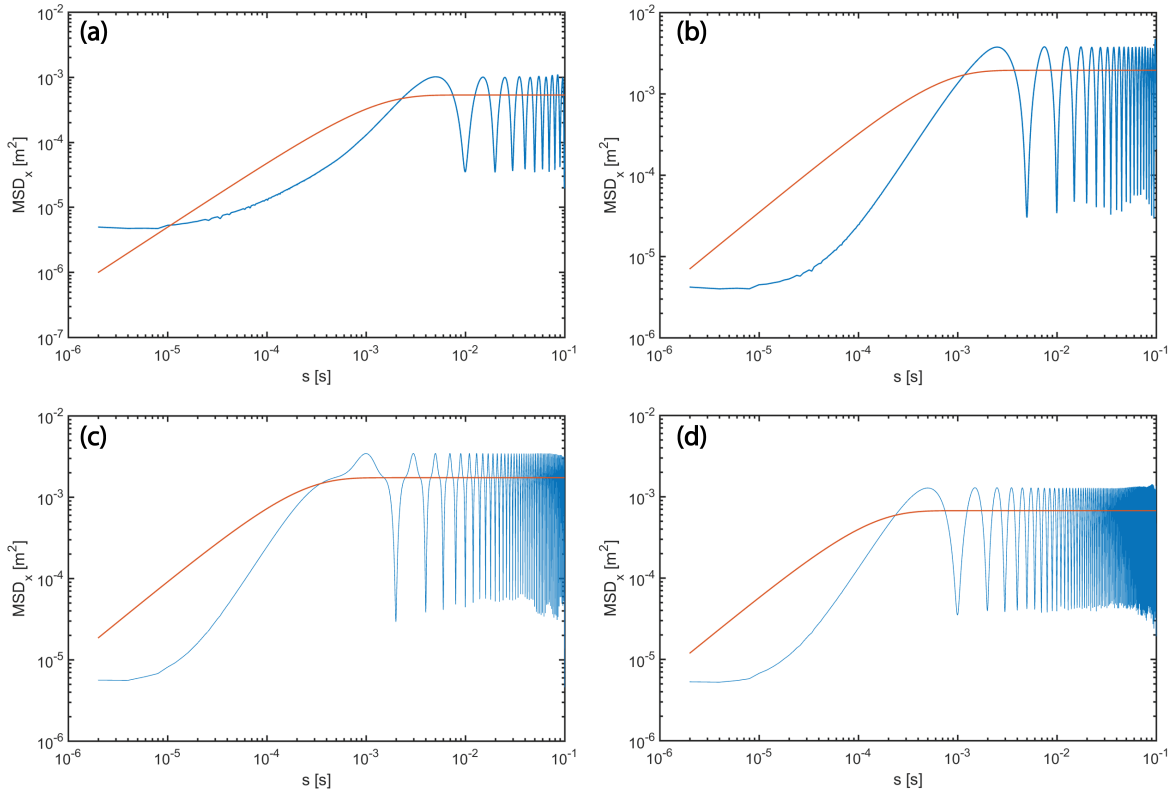

Figure 5.8. Mean square displacement analysis when there is a sound wave with a) 100, b) 300, c) 500, and d) 1000 Hz frequency.

Similar to Figure 5.3 which is the case for no sound, ACF also converged to zero in the existence of sound waves. In like manner to mean square displacement analysis (Figure 5.8), the raise in the frequency of the sound wave caused an escalation on the recurrence of moving between the edges. It was also observed that the change in the lag time of the particle was insignificant. The difference in the amplitude of voltage values may be a result of taking data for different particles, the disparity in the relative position of sound source and the particle, the attenuation differences of the sound wave as a result of difference in path, variations at the angle of sound source with respect to the bead.

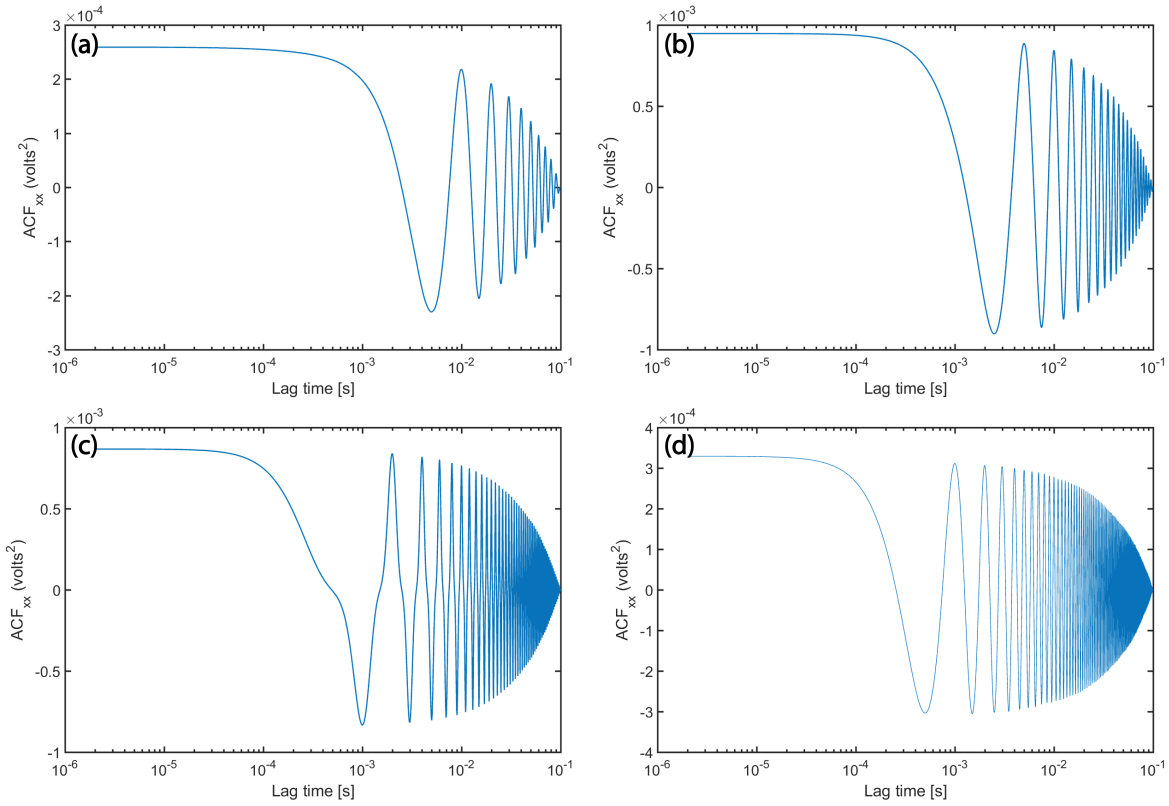

Figure 5.9. Autocorrelation function analysis when there is a) no sound, a sound wave with b) 300, c) 500, and d) 1000 Hz frequency.

Figure 5.10a, Figure 5.10b, Figure 5.10c, and Figure 5.10d illustrate the graphs of power spectrum analysis when there is a sound wave with 100, 300, 500, and 1000 Hz frequency, respectively. The peaks that belong to the central frequency of the sound source and its harmonics can clearly be seen.

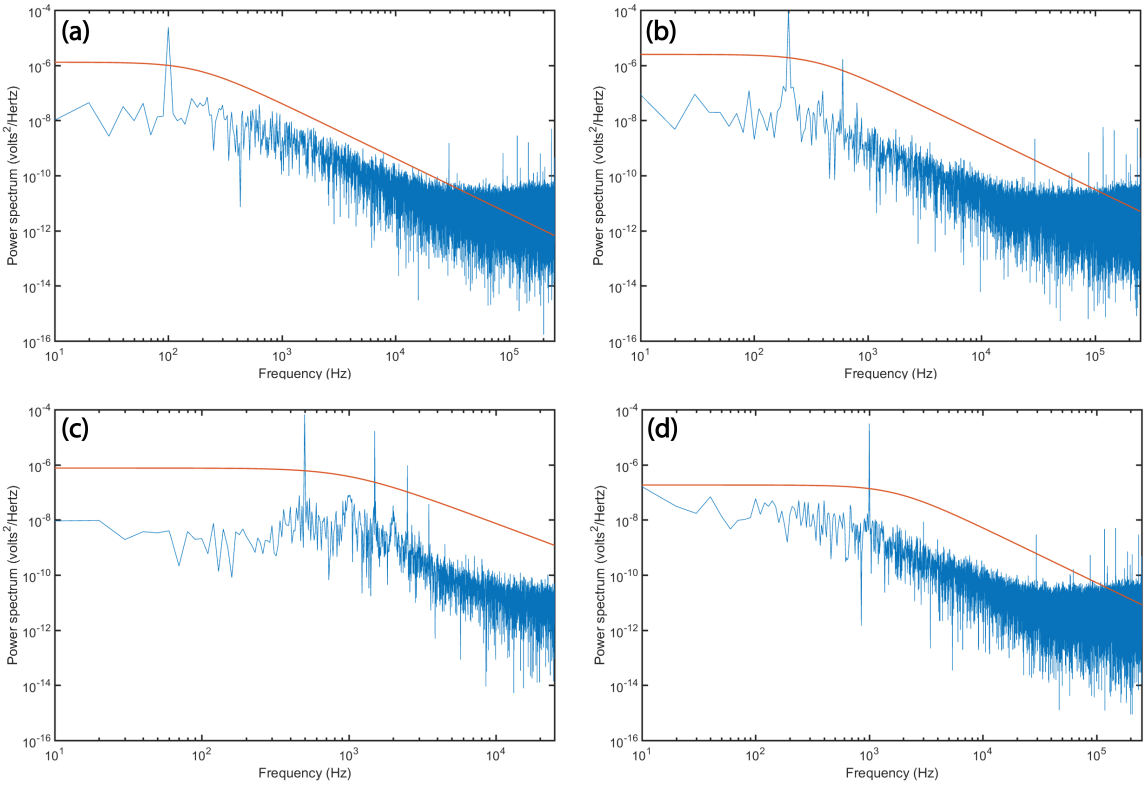

Figure 5.10. Power spectrum analysis when there is a) no sound, a sound wave with b) 300, c) 500, and d) 1000 Hz frequency.

5.4. Photoacoustic Wave Detection with Hybrid Photoacoustic Microscopy and Optical tweezers System

5.4.1. Simulations

For simulations, Equation 5.9 is solved with Finite-difference method, by the replacement below

$$\frac{dr(t)}{dt} \rightarrow (r_i - r_{i-1})/\Delta t \tag{5.30}$$

and the following equations are acquired [180]:

$$\begin{aligned} x_i &= x_{i-1} - \frac{\kappa_x}{\gamma} x_{i-1}\Delta t + \sqrt{2D\Delta t} w_{x,i} \\ y_i &= y_{i-1} - \frac{\kappa_y}{\gamma} y_{i-1}\Delta t + \sqrt{2D\Delta t} w_{y,i} \\ z_i &= z_{i-1} - \frac{\kappa_z}{\gamma} z_{i-1}\Delta t + \sqrt{2D\Delta t} w_{z,i} \end{aligned} \tag{5.31}$$

5.4.2. Properties of the White Noise

A white noise W(t) has the following properties [180]:

1. $\langle W(\mathrm{t}) \rangle = 0$ for each t;

2. $\langle W(t)^2 \rangle = 1$ for each t;

3. $W(t_1)$ and $W(t_2)$ are independent of each other for $t_1 \neq t_2$.

An open source library is used for simulation studies [180]. The library is written in object-oriented programming and includes Brownian motion of a particle. For this thesis, photoacoustic radiation force is modeled theoretically (Chapter 4) and added as an external force to Equation 5.6. Then simulations are made accordingly. Figure 5.11 shows the trajectories of a single particle under random walk (blue) and with the influence of a photoacoustic radiation force (red) having a maximum value of 20 pN.

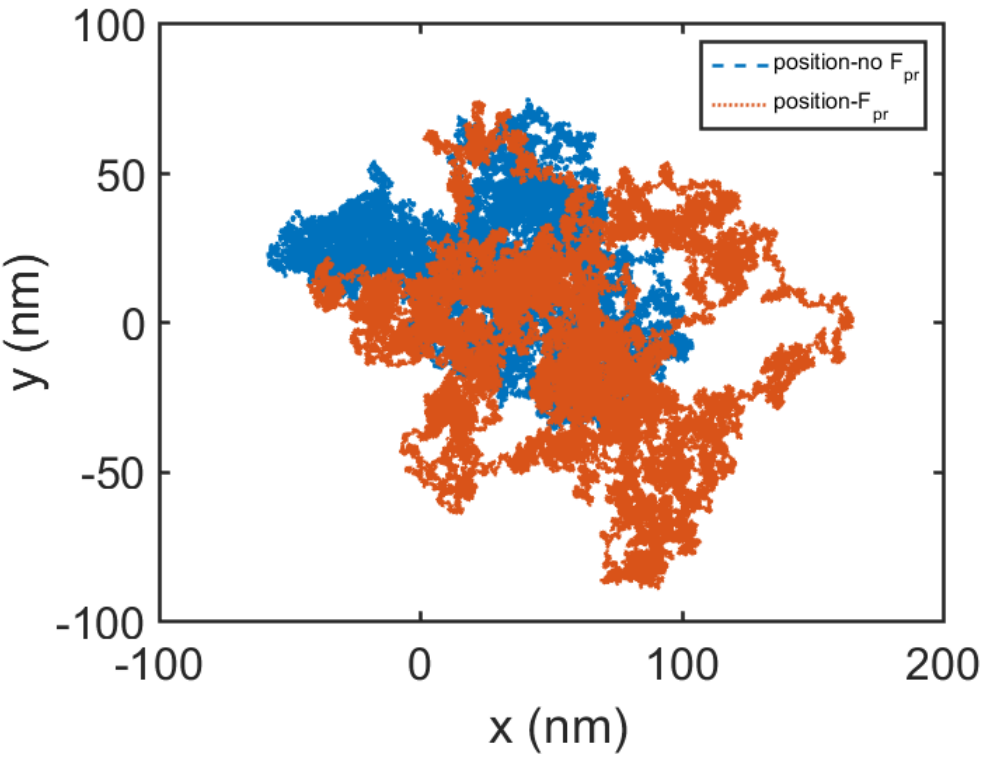

Figure 5.11. The trajectories of a single particle under random walk (blue) and the influence of a photoacoustic radiation force (red) having a maximum value of 20 pN.

The data shown here belong to a particle with 2 μm radius in water, with a diffusion coefficient, D = 1.0987×10^{-13} m^2/s, friction coefficient, $\gamma = 3.7699 \times 10^{-8}$ kg/s released at t=0 second from r =0 μm. Spring constants are taken as $k_x = 2 \times 10^{-6}$ N/m and $k_y = 2 \times 10^{-6}$ N/m. Equilibrium point is taken as, r_{eq} = [0,0]. Time intervals for simulations are, dt = 100 ns, for a total number of 10^6 data points corresponding to a total time of 0.1 seconds. There is no significant variance difference between the

two trajectories. Figure 5.11 shows the positions of a single particle under random walk (blue) and with the influence of a photoacoustic radiation force (red) having a maximum value of 40 pN under the same parameters summarized above.

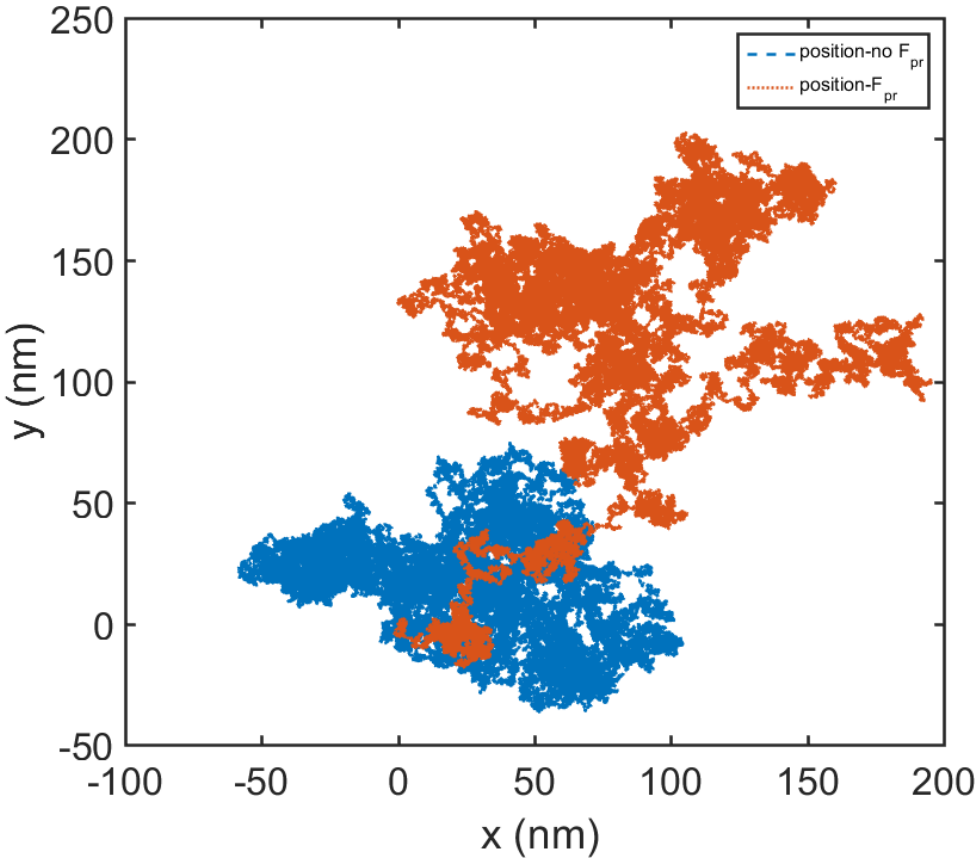

Figure 5.12. The trajectories of a single particle under random walk (blue) and the affect of a photoacoustic radiation force (red) having a maximum value of 40 pN.

Although there is no significant difference in the variance, random walks are cumulated around a 100 nm far from the equilibrium point. The influence of photoacoustic radiation force is felt by the particle especially in the beginning of trajectory before settling down. Further analysis is performed by taking Fast Fourier transform (FFT) of the positions. Figure 5.13 shows the comparison of FFT analysis for the trajectories of the particle when there is no photoacoustic wave (yellow), a photoacoustic wave with an initial pressure, $p_0 = 130$ kPa (red), and $p_0 = 180$ kPa (blue).

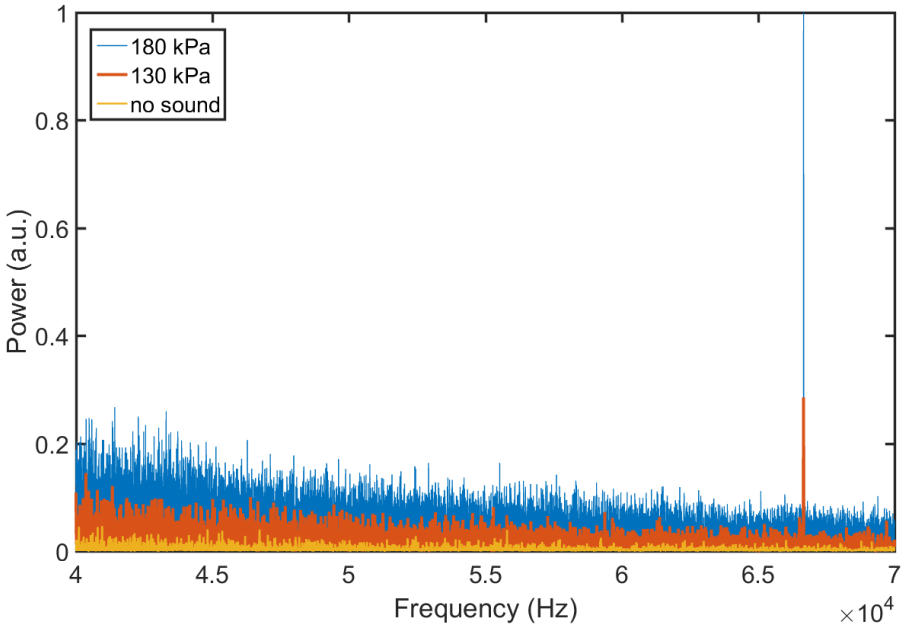

Figure 5.13. FFT analysis for the trajectories of the particle when there is no photoacoustic wave (yellow), a photoacoustic wave with an initial pressure, $p_0 = 130$ kPa (red), and $p_0 = 180$ kPa (blue).

The repetition frequency of the excitation source (fiber laser) and its harmonics can clearly be seen which shows the existence of a photoacoustic wave. It is important to note that the amplitude of the frequency component increases as the the amplitude of the photoacoustic wave, thus the amount of photoacoustic radiation force increases. It is possible to get information about the amplitude of photoacoustic wave from its intensity in the power spectra.

5.4.3. Experiments

An inverted free microscope body (Nikon Eclipse) is used to combine photoacoustic microscopy and optical tweezers system that can be seen in Figure 5.14. A continuous wave laser diode that operates at 976 nm wavelength delivering a maximum power of 600 mW is used for trapping.

A shortpass dichroic mirror (805 nm) reflects the laser beam and transmits the visible wavelengths to CCD camera for visualization, manipulation, and tracking of the particles. A 50-50 beam splitter is used right after the dichroic mirror for the separation of back reflected light from trapped particle to be monitored by the CCD and also a QPD. Two different configurations are used for the hybrid system. Figure 5.15 shows the schematic of the experimental setup in its first configuration. A 100X oil immersion (NA, 1.3) is used to focus the laser beam. For illumination of the sample a led flashlamp is used with some angle in this configuration.

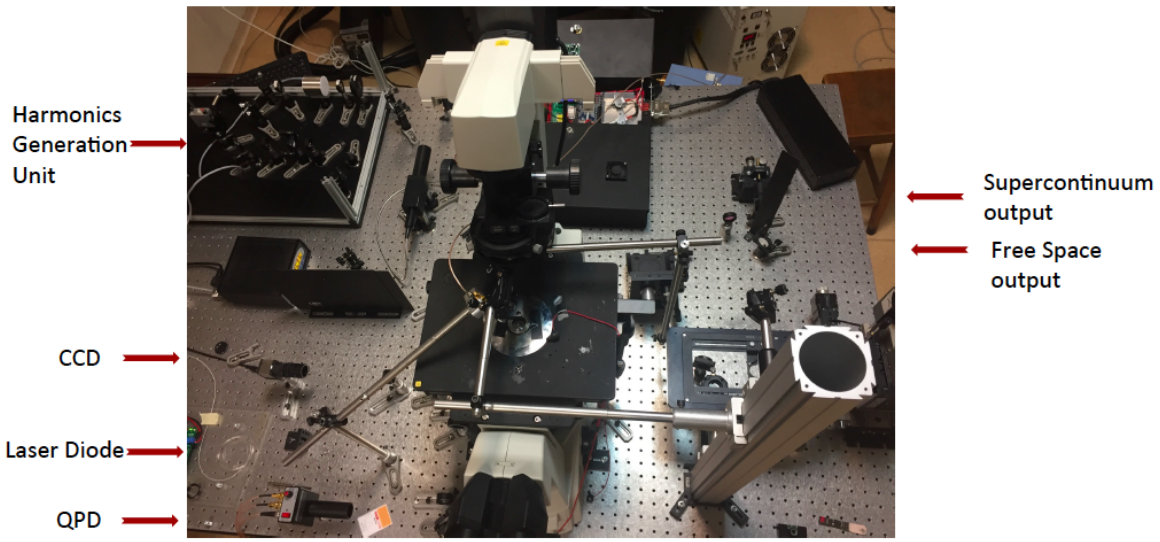

Figure 5.14. The photograph of the hybrid photoacoustic microscopy and optical tweezers system.

In the photoacoustic microscopy part, the laser source is a custom designed tunable fiber laser which provides pulses at a repetition rate of 65 kHz with a wavelength-tuning range of 600 to 1100 nm also with the harmonics of 1064 nm that are 532, 355, and 266 nm. The preferred wavelength is filtered through a bandpass filter, then the beam is expanded through a home built telescope. A 10X objective is used to focus the light.

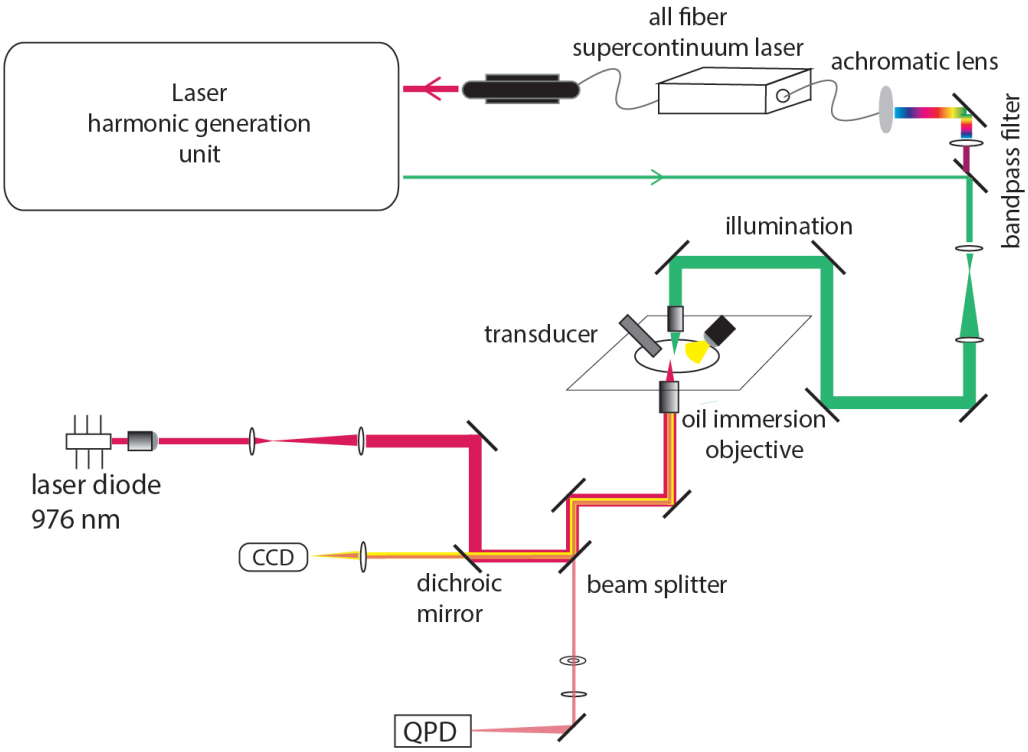

Figure 5.15. The schematics of the hybrid photoacoustic microscopy and optical tweezers system in its first configuration.

The laser beam for the generation of photoacoustic waves is coupled to the hybrid system from the top of the XY stage of the microscope since optical trapping is only possible against the gravity. A 3.5-MHz unfocused ultrasonic transducer is attached to the surface of a slide to monitor photoacoustic waves. The signals are initially amplified by 40 dB using a pre-amplifier (5678, 40 MHz bandwidth, Olympus) and then 39 dB via a pulser/receiver (5073PR, Olympus). Then they were digitized through a DAQ (Razor Express CompuScope 1422, Gage Applied Technologies, Inc.). Because of the difficulties in the illumination and acoustic monitoring , the hybrid system is also built in a second configuration whose schematic can be seen in Figure 5.16.

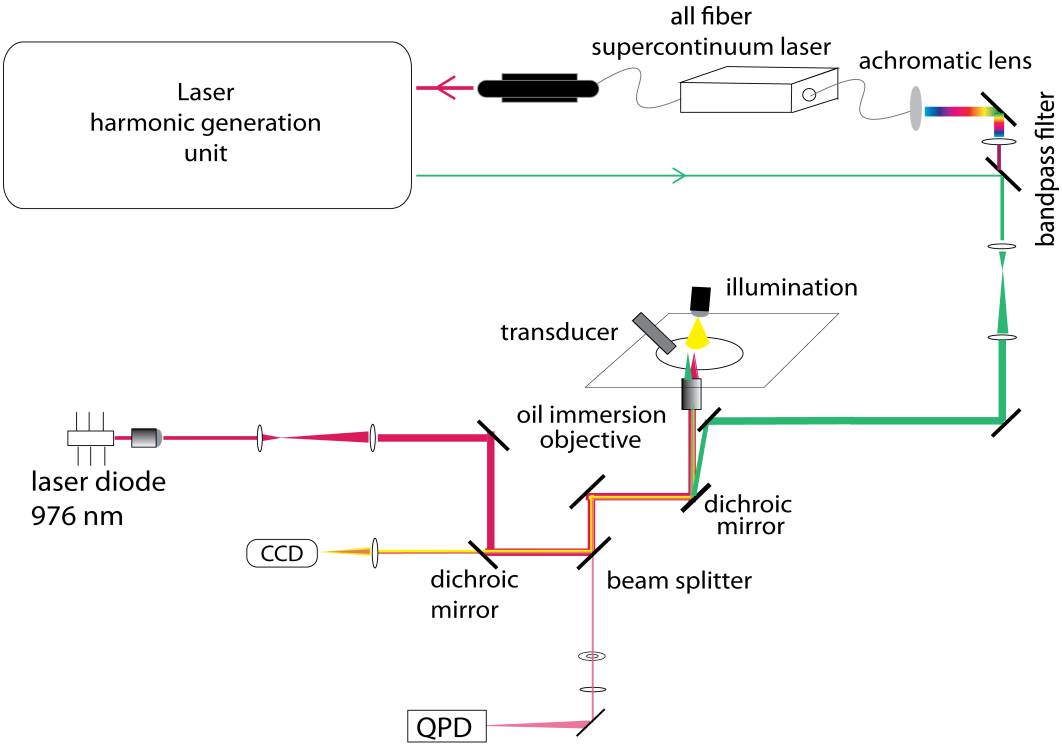

Figure 5.16. The schematic of the hybrid photoacoustic microscopy and optical tweezers system in its second configuration.

The photograph of the optical tweezers part of the hybrid system is shown in Figure 5.17. The laser beam couples to the system being transmitted via a short-pass filter (DMSP 1000, Thorlabs) and enters the microscope body from its backward port. Afterwards, a dichroich mirror (DMLP 550, Thorlabs) reflects the beam to a conjoint sample plane.

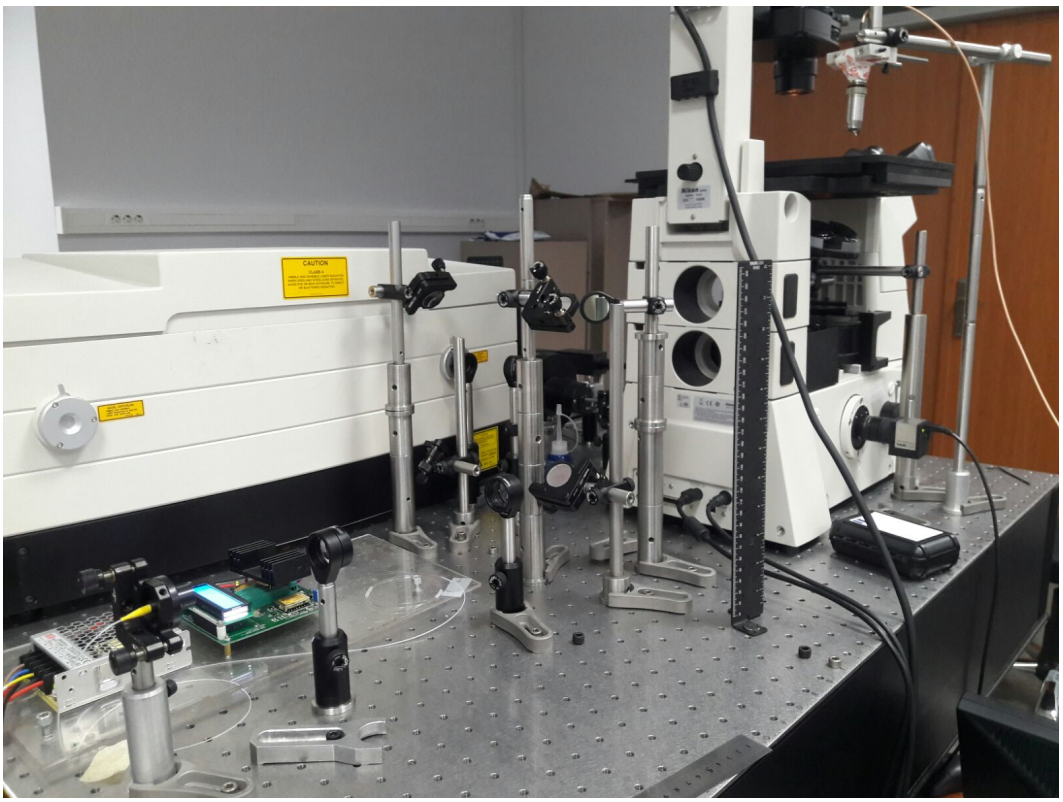

Figure 5.17. The photograph that belongs to the optical tweezers part of the hybrid system (second configuration).

The photograph of the photoacoustic microscopy part of the hybrid system is shown in Figure 5.20. The laser beam couples to the system being reflected via a short-pass filter (DMSP 1000, Thorlabs) and enters the microscope body from its backward port. Afterwards, a dichroich mirror (DMLP 550, Thorlabs) reflects the beam to the conjoint sample plane.

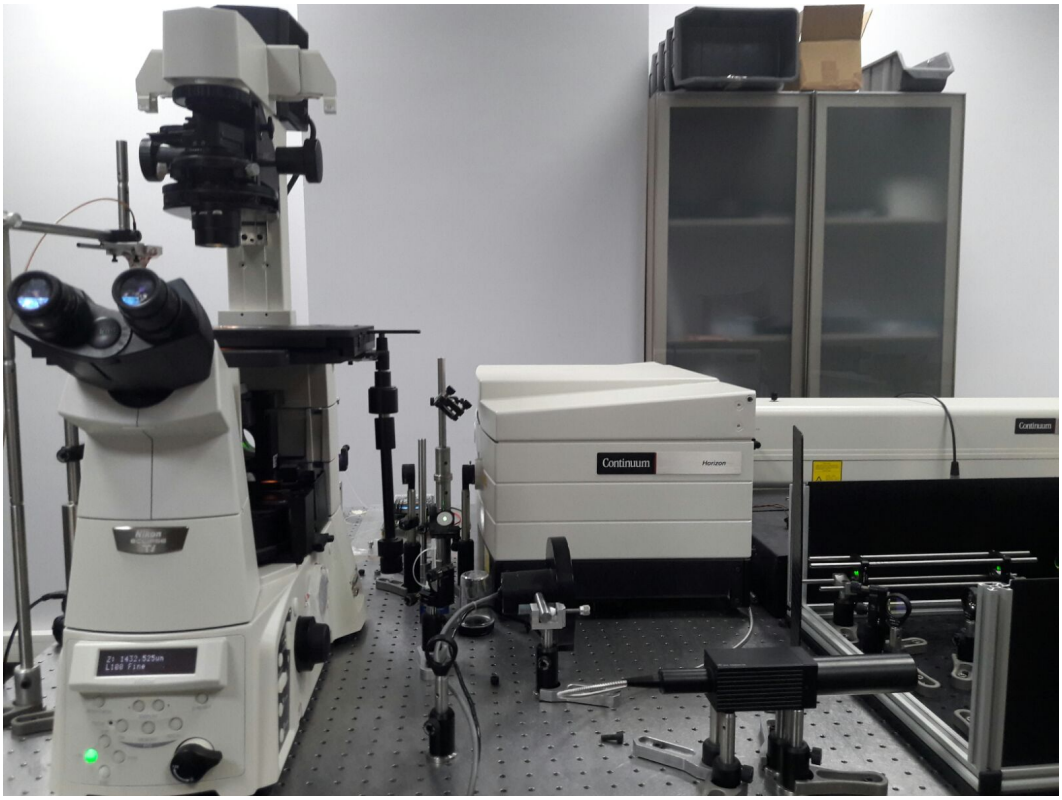

Figure 5.18. The photograph that belongs to the photoacoustic microscopy part of the hybrid system (second configuration).

When the laser pulse is absorbed by a target, thermoelastic expansion induces acoustic signals which then cause a change in the behavior of the trapped particle. Figure 5.19 illustrates the usage of a bead as a photoacoustic wave detector.

All of the analysis are done by tracking the trapped particle either by a CCD or a QPD. For the camera tracing, an algorithm that follows the most intense pixel at the center of the particle is used. Figure 5.20 shows the image of a silica particle with a radius of 2 μm inside a trap with a red circle marking the most intense pixel.

Experiments are conducted to see the affect of the magnitude of pressure on the FFT amplitude of the particle positions. Figure 5.21a shows FFT analysis for the case of photoacoustic wave absence ($P_1 = 0$). Figure 5.21b and 5.21c belong to the same

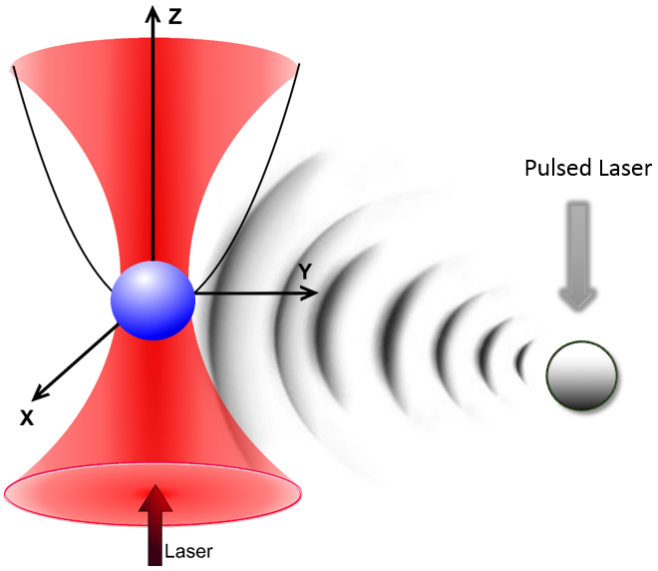

Figure 5.19. The illustration of the bead (blue sphere) as a detector for photoacoustic waves generated by an absorber (grey sphere).

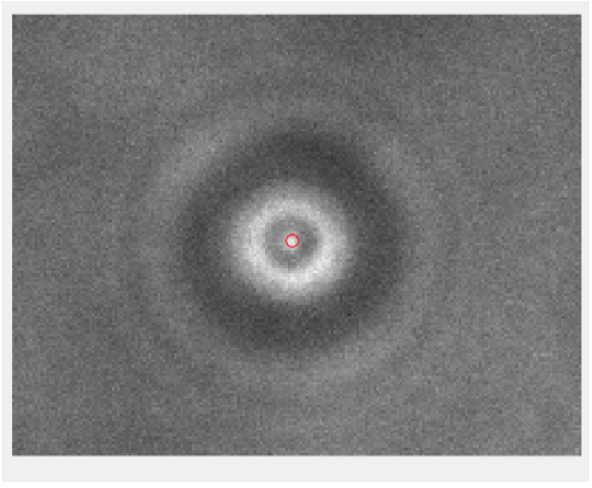

Figure 5.20. The image of a silica particle with a radius of 2 μm inside a trap. Red circle marks the most intense pixel for tracking its positions.

analysis for the laser pulse energies of $P_2 = 0.5$ and $P_3 = 1.5$ μJ, respectively; with the chopper operated at 10.5 Hz.

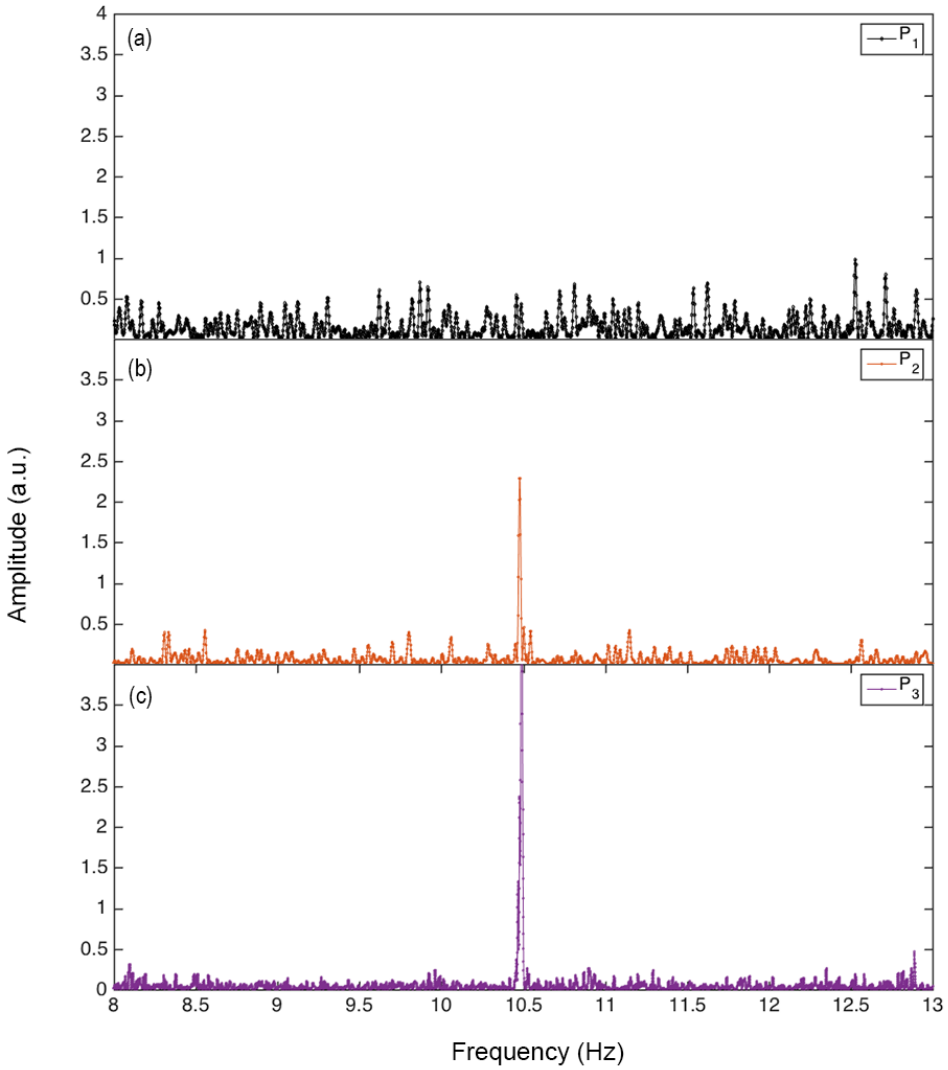

Figure 5.21. FFT amplitude of trapped particle positions versus frequency for the pulse energies of a) $P_1 = 0$, b) $P_2 = 0.5$, and c) $P_3 = 1.5$ μJ, respectively; with the chopper operated at 10.5 Hz.

Additionally, the excitation laser frequency is varied by the chopper revealing that the peak in the FFT precisely follows it. Figure 5.22 shows normalized FFT amplitude of the particle trajectories versus frequency for the chopper frequencies of a) $f_1 = 10.5$, b) $f_2 = 15.6$, and c) $f_3 = 19,6$ Hz, respectively.

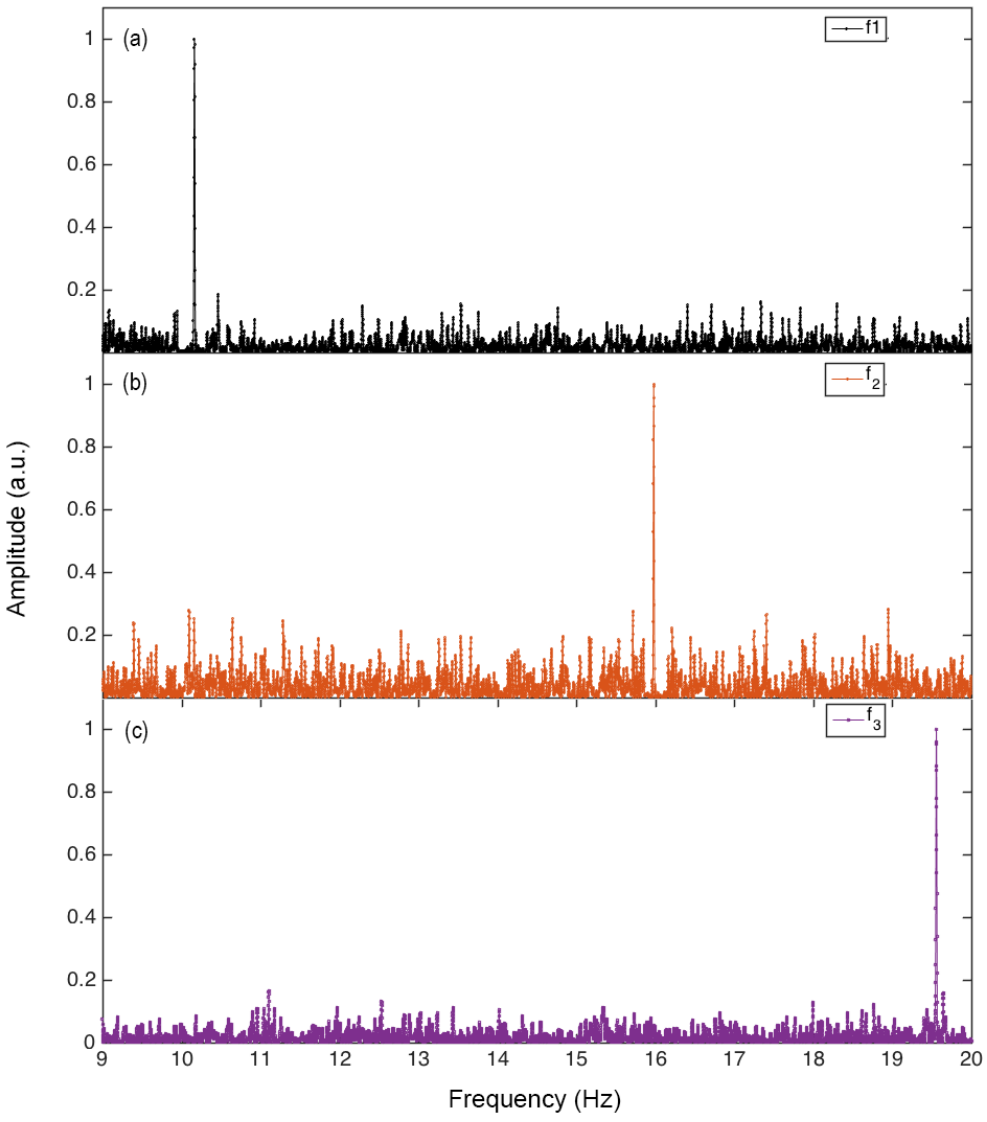

Figure 5.22. Normalized FFT amplitude of the particle trajectories versus frequency for the chopper frequencies of a) $f_1 = 10.5$, b) $f_2 = 15.6$, and c) $f_3 = 19,6$ Hz, respectively.

In the spatial domain, no significant difference is observed between the cases of photoacoustic wave absence and existence. The voltages acquired from CCD versus time for a pulse energy of $P_1 = 1.5$ μJ can be seen in Figure 5.23a. The recordings are made for 2000 frames with a frame rate of 40. Figure 5.23b shows the voltages when there is no sound.

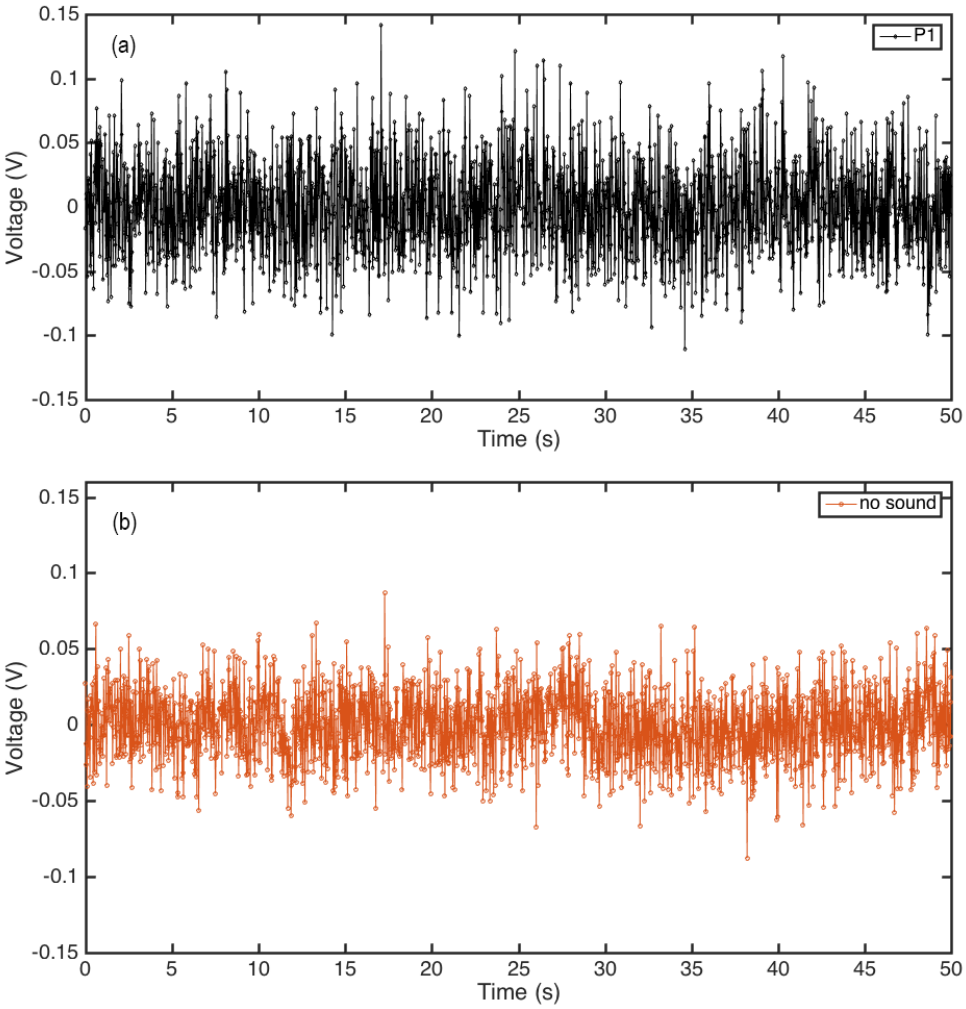

Figure 5.23. The voltages acquired from CCD versus time for a) a pulse energy of $P_1 = 1.5$ μJ and b) the absence of photoacoustic wave.

Figure 5.24 shows the amplitudes of photoacoustic waves (in units of voltage) for different pulse energy values.

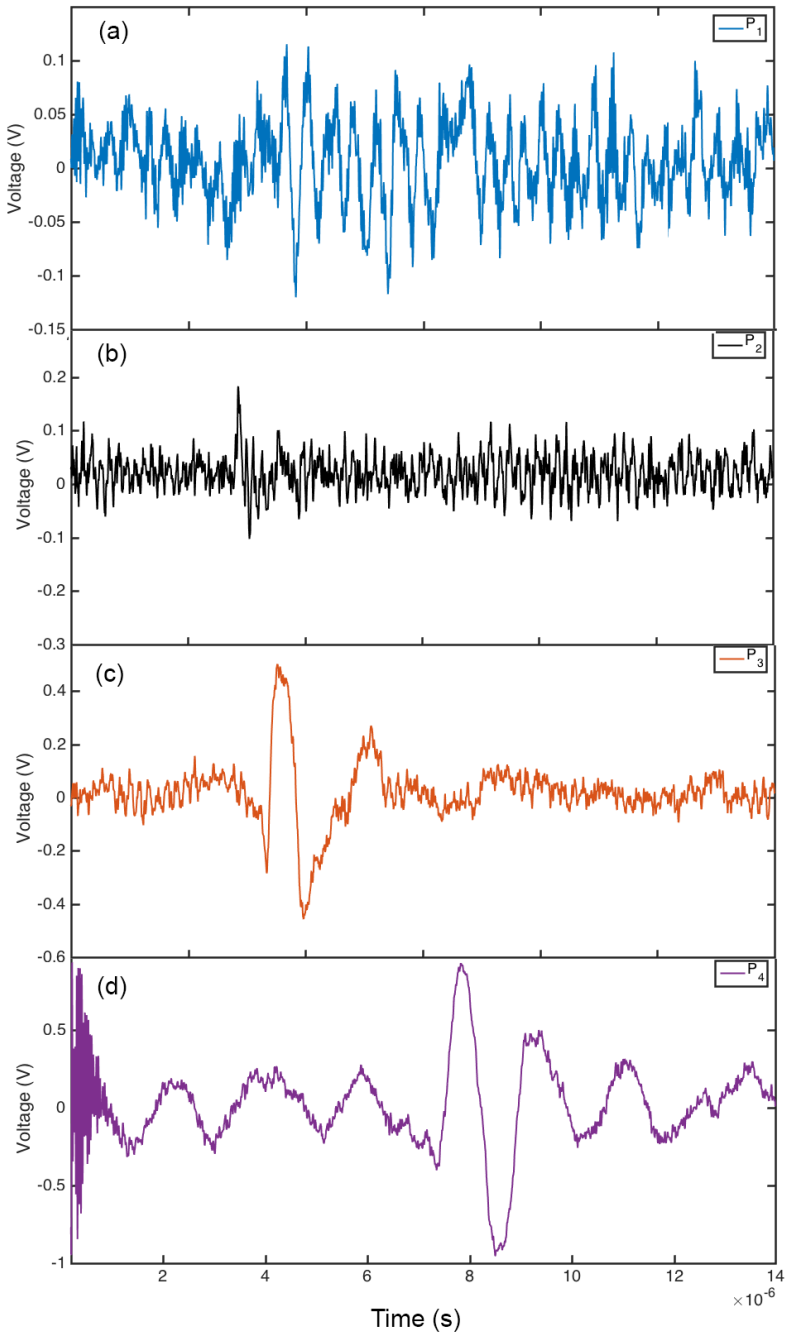

Figure 5.24. The photoacoustic signals (in units of voltage) for different pulse energy values versus time (in units of seconds).

6. PROTON INDUCED ACOUSTIC WAVES

The energy deposited by pulsed proton irradiation causes thermoelastic expansion that induces a pressure wave. The physical mechanism behind protonacoustics is equivalent to that in photoacoustics and X-ray induced acoustics [5, 186]. Therefore, the protonacoustic pressure wave distribution can be approximated by the wave equation:

$$(\nabla^2 - \frac{1}{v_s^2}\frac{\partial^2}{\partial t^2})p(\mathbf{r},t) = -\frac{\beta}{\kappa v_s^2}\frac{\partial^2 T(\mathbf{r},t)}{\partial t^2} \tag{6.1}$$

The left hand side of Equation 6.1 represents the pressure wave $p(\mathbf{r},t)$ at position $\mathbf{r}$ and time t where v_s is the speed of sound while the right hand side of Equation 6.1 stands for the source term. Here, β is the thermal coefficient of volume expansion, κ is the isothermal compressibility, and $T(\mathbf{r},t)$ is the increase in temperature at position $\mathbf{r}$ and time t.

Heat diffusion could be neglected, with the assumption of instantaneous energy deposition, since heating occurs over a shorter period of time than heat relaxation time. Excluding heat conductivity, the change in temperature can be expressed in terms of heating function, i.e., the amount of heat generated by interactions of protons with atoms of tissue per unit volume per unit time, and ρ and C_V denote density and the specific heat capacity at constant volume, respectively,

$$\rho C_V \frac{\partial T}{\partial t} = H(\mathbf{r},t) \tag{6.2}$$

The heating term can be decomposed into a product of radial and temporal components as follows

$$H(\mathbf{r}, t) = A(\mathbf{r})H(t) \tag{6.3}$$

Here, we take the following Gaussian spatiotemporal profiles for the temporal and radial parts, H(t) and A(r), respectively; to obtain explicit dependencies of proton beam parameters (energy, pulse duration and beam width) on the resultant acoustic wave:

$$H(t) = \frac{\exp(-\frac{t^2}{2\tau^2})}{\sqrt{2\pi\tau^2}} \tag{6.4}$$

and

$$A(\mathbf{r}) = \frac{p_0}{v_s^2}\frac{C_P}{\beta}\exp(-\frac{r^2}{2\sigma^2})\theta(r)\theta(-r+R) \tag{6.5}$$

where τ and σ are the pulse duration and beam width of the proton beam, respectively. In the literature, temporal profile of the heating term is generally described by the Dirac delta function [5]. Nevertheless, the solution of the acoustic wave equation for the Gaussian spatiotemporal approximation gives opportunity to directly observe the effect of the proton beam parameters on the pressure wave. The analytic solution of the photoacoustic wave equation presented in our previous work is based on the Fourier transform and Greens' function methods [159]. Firstly, the Fourier transform is applied to reduce the acoustic wave equation to a simple wave equation in frequency domain. Later, using the Greens' function technique, frequency domain solutions are obtained. In other words, the frequency domain solution is found by calculating the following

integral:

$$\tilde{p}(\mathbf{r},\omega) = \int \tilde{G}(\mathbf{r},\mathbf{r}';\omega)\tilde{S}(\mathbf{r}';\omega)d^3r' \tag{6.6}$$

Here, tilde ($\tilde{}$) represents the Fourier transform. In the Equation 6.6, $\tilde{G}(\mathbf{r},\mathbf{r}';\omega)$ is given by [187]

$$\tilde{G}(\mathbf{r},\mathbf{r}';\omega) = -\frac{1}{4\pi \mid \mathbf{r}-\mathbf{r}' \mid}\exp(i\frac{\omega}{v_s} \mid \mathbf{r}-\mathbf{r}' \mid) \tag{6.7}$$

and the Fourier transform of the source term is given by [159]

$$\tilde{S}(\mathbf{r},t) = \frac{i}{\sqrt{2\pi}}\frac{p_0(\mathbf{r})}{v_s^2}\omega\exp(-\frac{\tau^2\omega^2}{2}) \tag{6.8}$$

Finally, using the inverse Fourier transform, the pressure wave is presented by the following comprehensive expression stated in Equation 4.14.

The instantaneous energy deposition caused by the short pulse duration of the proton beam leads to a local rise in pressure immediately after the excitation. The initial pressure rise, p_0, can be expressed in terms of the Grüneisen parameter Γ, and the local energy density u,

$$p_0 = \Gamma u \tag{6.9}$$

The dimensionless Grüneisen parameter Γ is defined as

$$\Gamma = \frac{\beta}{\kappa \rho C_V} \tag{6.10}$$

where β is thermal expansion coefficient, κ is isothermal compressibility modulus, ρ is mass density of the medium, and C_V is heat capacity at constant volume. For soft tissue its value is measured as 0.2 [7].

The energy density is related to dose D and density ρ by $u = D\rho$ [152]. Then, the initial pressure rise, p_0, can be written as

$$p_0 = \Gamma \rho D \tag{6.11}$$

In order to calculate the initial pressure rise, the dose term D in Equation 6.11 needs to be determined from the Bragg curve. An analytic approximation for the Bragg curve provided by Bortfeld is used to calculate the depth-dose distribution [158]. By using that model, the relationship between energy of the beam and beam width is established, then deposited dose values are obtained for various energies. These values are substituted into Equation 4.14 and Equation 6.11 to determine the value of the pressure for various parameters.

In general, the fundamental assumption for the energy distribution is that the beam would be mono-energetic just before it enters the medium. However, in realistic cases, the initial spectral energy distribution has a Gaussian shape rather than a perfect δ-shape. Furthermore, the range of individual protons varies due to statistical differences in energy losses. Thus, the Bragg peak is broadened around R_0 which is

known as range straggling [158]. To consider aforementioned effects, we use a dose calculation algorithm which contains a multiplication of a central axis term, commonly referred as "Bragg curve", and an off-axis term [188].

Beam specifications such as pulse duration, beam diameter, beam width, etc. should be measured with low uncertainty for dose monitoring since they have a considerably significant effect on the acoustic waves. These parameters depend on the type of the accelerator which are summarized in Table 6.1 including pulse repetition frequency (PRF) [189–197]. Parameters on simulations are chosen according to these specifications.

Table 6.1. General specifications of accelerator types.

	Cyclotron	Synchrotron	FFAG	DWA	Linac	Laser Driven
Current (nA)	1-300	1-10	1-100	Very High	1600	$\sim$ 1000
PRF (Hz)	Cont.	0.5-50	100-1000	<1	1-60	1-1000
Pulse Length	Cont.	0.5 μs-3 s	$\sim$ 100 ns	$\sim$ ns	$\sim$ μs	$\sim$ ps

6.1. Results

Firstly, we investigate depth-dose profiles of Bragg curves. Figure 6.1a shows dose distribution as a function of distance through the stopping medium of water, for clinical energy values of proton beam, i.e. 50-200 MeV. Here, the number of protons is $N_p = 4 \times 10^6$, and the beam diameter is taken as 1.50 cm [142,152]. Bortfeld's model is used for calculations of beam width and approximate dose deposition [158]. Afterwards, these calculated values are used for the simulations of induced acoustic waves, which are performed by the MATLAB (MathWorks Inc.) software. For biomedical applications, the mass density of the medium is taken $\rho = 1000$ kg/m^3 which is an acceptable approximation for the soft tissue. The speed of sound in tissue is taken as $v_s = 1480$ m/s [7].

The decrease in the value of the absorbed dose at the Bragg peak and the broadening of the beam width are clearly visible as the energy of individual protons in the beam increases. Figure 6.1b shows that beam width increases with the beam energy. The energy spectrum and range straggling are taken into account for calculations of

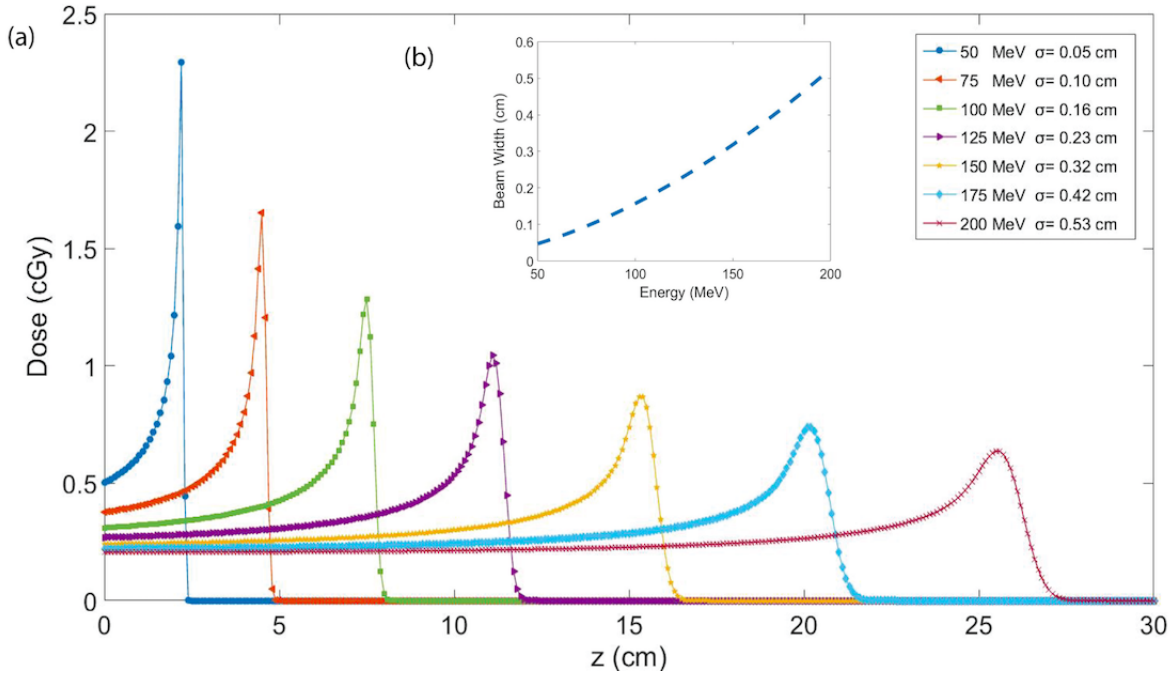

Figure 6.1. a) Dose in units of cGy versus depth in units of cm for energies of 50, 75, 100, 125, 150, 175, 200 MeV with beam widths of 0.05, 0.10, 0.16, 0.23, 0.32, 0.42, 0.53 cm, respectively; for $N_p = 4 \times 10^6$ and a beam diameter of 1.50 cm. b) Beam width vs energy.

beam width and approximate maximum dose. More energetic beams can reach to tumors in the deeper regions of body in the expense of delivered dose per pulse.

The approximate dose delivered to tissue can be seen in Figure 6.2a and 6.2b for beam diameters of 1.50 and 4.00 cm, respectively; for beam energy in the range of 50 to 200 MeV for different number of protons per pulse, $N_p = 4 \times 10^6$, 1×10^7, and 2×10^7, respectively. The decreasing maximum dose corresponding to the increasing energy can clearly be seen in Figure 6.2.

It is crucial to understand the approximations and fitting mechanisms of Bortfeld's study, since it is used to determine the delivered dose [158]. Bortfeld compared the analytical results with measured and numerically calculated depth-dose curves to validate the model [158]. The energy spectrum and range straggling were taken into account for calculations of dose. In order to consider the tail of the energy spectrum, a relatively small fraction, ϵ, to the total fluence in the peak was defined. For the purpose of achieving an optimum fit to the measured data, ϵ, the beam width σ, and range R_0 were varied. To be able to compare with measurements, maximum dose delivered was normalized to 1.0 because no absolute values were available. The comparisons of measurements with and without the proton nozzle in the beam path were also investigated, and concluded that the model is in harmony with measurements, noting that nozzle causes a higher value of ϵ for the fit. Analytical results were also compared with numerically calculated Bragg curves, in this case, normalization was not necessary and the model predicted 5% higher peak dose than the TRIUMF algorithm. The approach was validated so that measured and calculate values could be easily be fitted within the error of measurement. Here, maximum dose delivered without any fitting is used.

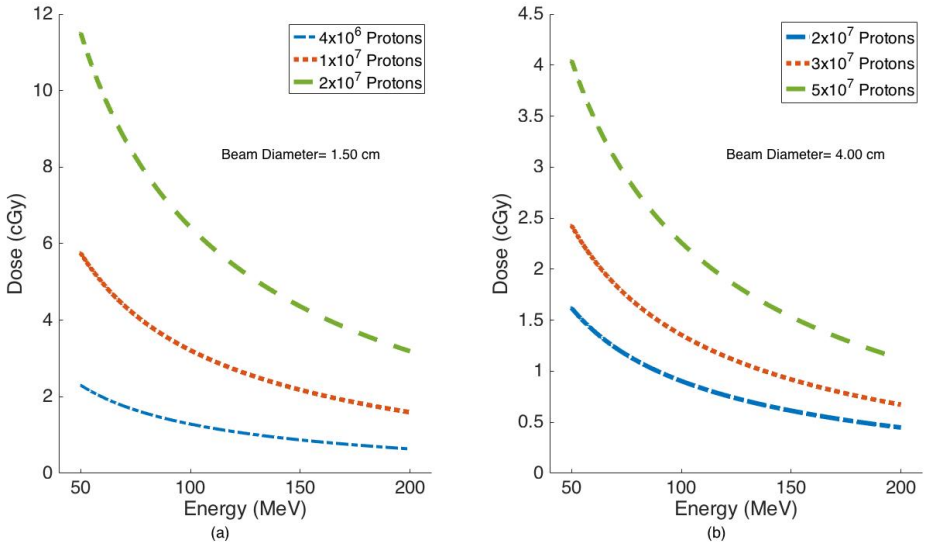

Figure 6.2. The approximate maximum delivered dose to soft tissue in units of cGy vs beam energy in units of MeV a) for $N_p = 4 \times 10^6, 1 \times 10^7, 2 \times 10^7$, respectively; and for a beam diameter of 1.50 cm, b) for $N_p = 2 \times 10^7, 3 \times 10^7, 5 \times 10^7$, respectively; and for a beam diameter of 4.00 cm.

6.1.1. The effect of beam energy on the amplitude of the acoustic wave.

Pressure waves are simulated for various energies to see the effect of the energy of the proton beam on the acoustic wave. Figure 6.3a shows the acoustic waveforms for a 1 μs pulse duration for energies 70, 100, 120 MeV corresponding 87.4, 64.2, 54.3 mGy dose, respectively; by using Eq. 4.14 for the number of protons $N_p = 5 \times 10^7$. Fig. 6.3b shows the acoustic waveforms for the same pulse duration and energies for number of protons $N_p = 4 \times 10^6$ that correspond to 17.5, 12.8, 6.4 mGy dose, respectively. For both simulations, beam diameter is taken as 1.50 cm. On the grounds of spatial widening of the beam width, the amplitude of the pressure rises, albeit the reduction in the delivered dose as energy increases. As the beam width decreases, the radial profile becomes very sharp starting to behave like a Dirac delta function, and acoustic wave convolves to an N-shaped signal.

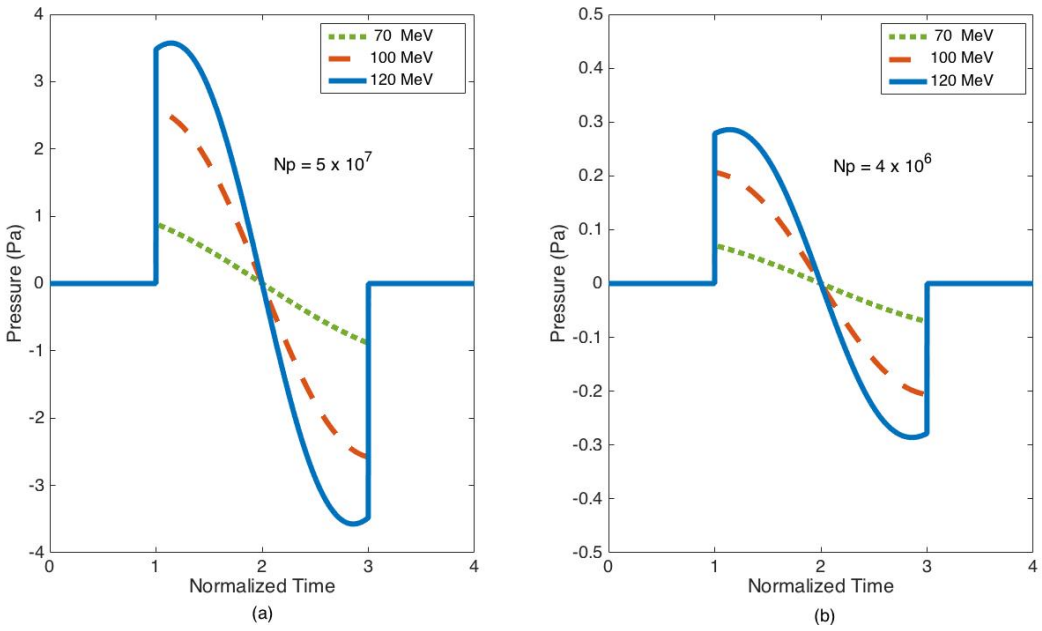

Figure 6.3. Pressure in units of Pa for energy values of 70, 100, 120 MeV, respectively; for r = 2R, the pulse duration $\tau = 1$ μs and a beam diameter of 1.50 cm for number of protons a) $N_p = 5 \times 10^7$ and b) $N_p = 4 \times 10^6$.

6.1.2. The effect of spill time on the amplitude of the acoustic wave.

6.1.2.1. Case 1: Constant proton number. The amplitude of acoustic wave is strongly related to the pulse duration, i.e. spill time of protons. The simulations of the acoustic waveforms for beam energy of 100 MeV are shown in Figure 6.4a for pulse durations of τ = 100, 350, and 600 ns, respectively; and in Figure 6.4b for pulse durations of τ = 1, 2, and 3 μs, respectively. For both calculations, number of protons is constant and taken as $N_p = 4 \times 10^6$. The shorter pulse duration yields larger acoustic wave amplitude as a result of sharper dose deposition in time. The time necessary for the conversion of kinetic energy into thermal energy should be shorter than the travel time of acoustic waves. For a very large pulse duration, this condition is violated and the Equation 4.14 is no longer valid.

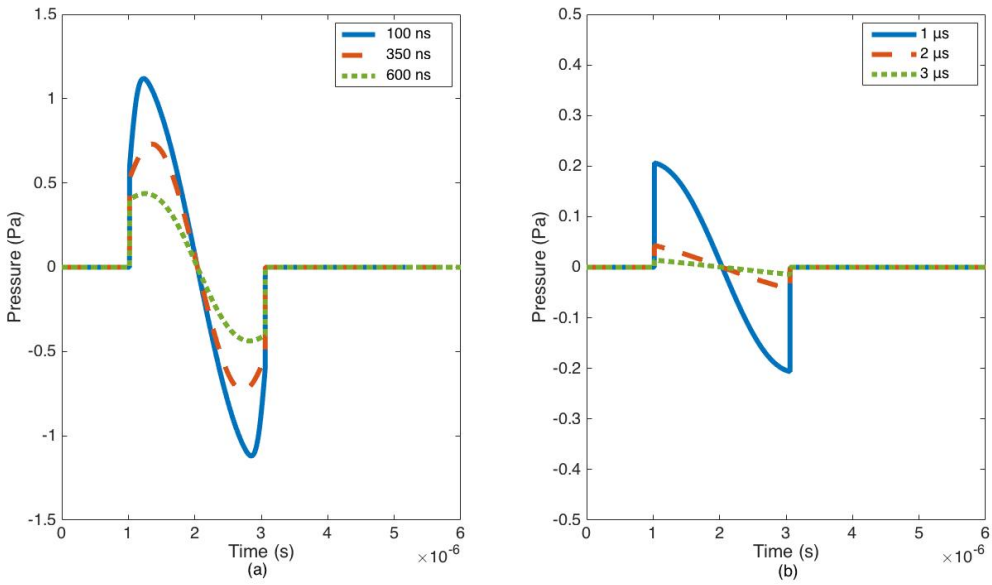

Figure 6.4. Pressure in units of Pa vs time in units of s for pulse duration values of a) τ = 100, 350, and 600 ns, respectively. b) τ = 1, 2, and 3 μs, respectively; for r = 2R, and the beam energy of 100 MeV for constant number of protons $Np = 4 \times 10^6$.

6.1.2.2. Case 2: Varying proton number with pulse duration. The simulations of the acoustic waveforms for beam energy of 70 MeV are shown in Figure 6.5a for pulse

durations of τ = 50, 100, 200, and 300 ns, respectively; and in Figure 6.5b for pulse durations of τ = 1, 2, 3, and 4 μs, respectively; for various number of protons with pulse duration. In the case of varying proton number, the amplitude of pressure wave increases with the pulse duration when spill time is on the order of nanoseconds. However, the amplitude of pressure wave decreases as pulse duration increases when spill time is on the order of microseconds since the effect of pulse duration on the acoustic wave prevails over the effect of increased proton number. The amplitude of pressure wave has a linear relationship with proton number and energy deposition, and this relation is illustrated in Figure 6.6 for pulse durations of 100 ns and 1 μs.

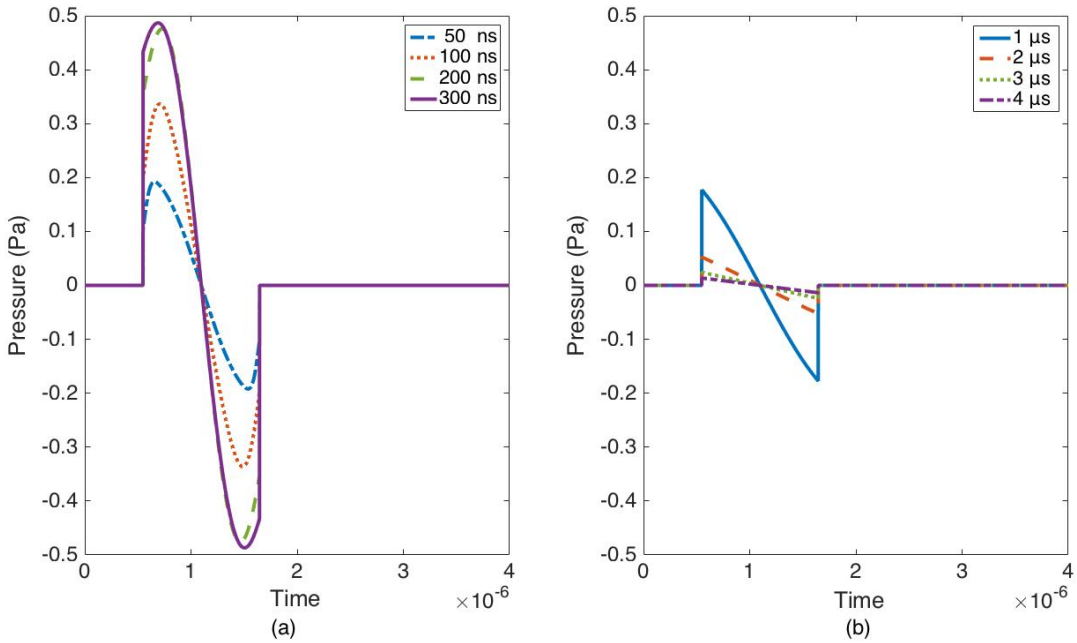

Figure 6.5. Pressure in units of Pa vs time in units of s for pulse duration values of a) τ = 50, 100, 200, and 300 ns, respectively; b) τ = 1, 2, 3, and 4 μs, respectively; for r = 2R beam diameter of 1.50 cm, and the beam energy of 70 MeV for varying number of protons with pulse duration.

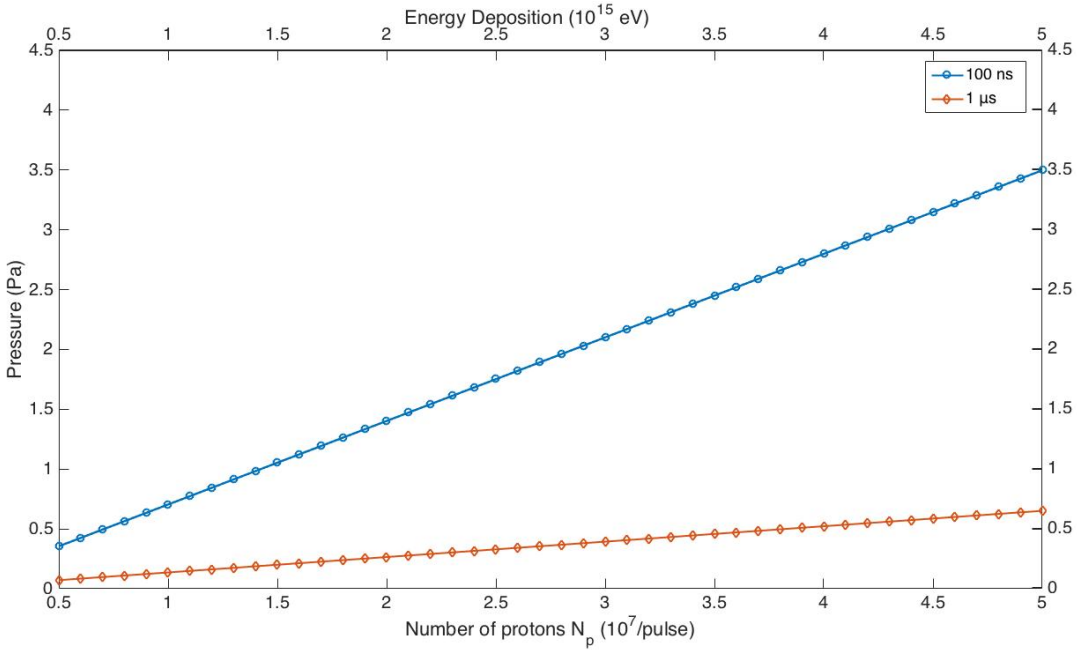

Figure 6.6. Pressure amplitude in units of Pa vs number of protons and beam energy for pulse durations of 100 ns and 1 μs.

6.1.3. The effect of the pulse duration and the energy of the proton beam on the frequency of the acoustic wave.

The simulations can also give information about the frequency spectrum of the induced pressure waves, which is important for the selection of detectors. The effect of the pulse duration and the energy of the proton beam on the frequency of the acoustic wave are investigated. Figure 6.7a shows power spectrum versus frequency for three different pulse durations, τ = 750, 1000, and 1250 ns, respectively; for a beam energy of 200 MeV while Figure 6.7b for energies E = 70, 100, and 120 MeV, respectively; for a pulse duration of 1 μs. The pulse duration and the beam width of the proton beam have a minor effect on the frequency of the acoustic wave. The main spectral components are found to be centered around 100 kHz for the first case and 200 kHz for the second.

We compare our results with existing experimental measurements and simulation studies in order to validate our approach.

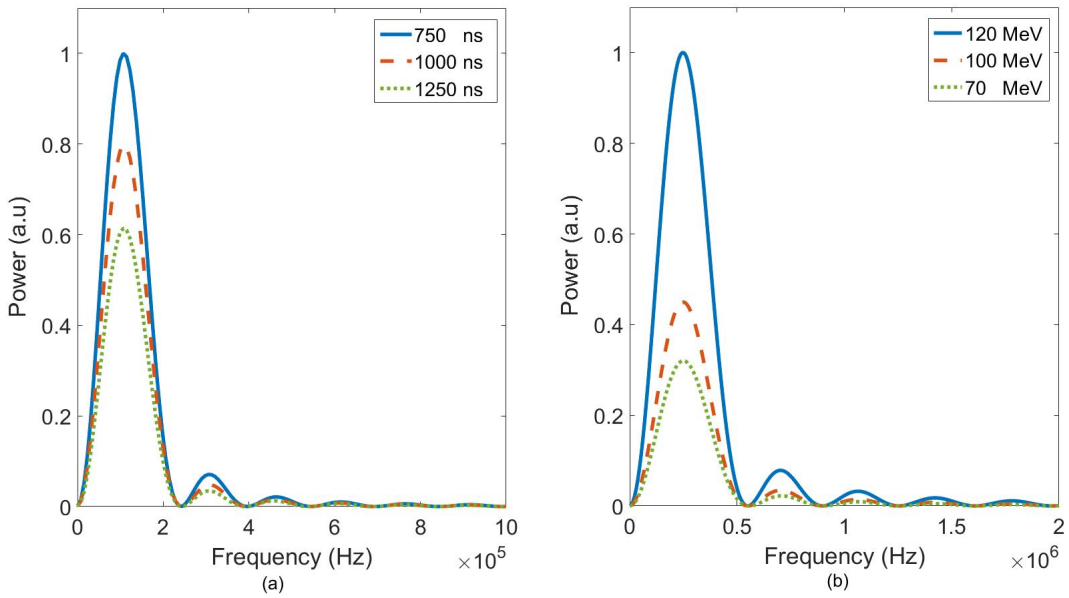

Figure 6.7. Power spectrum versus frequency a) for pulse durations τ = 750, 1000, and 1250 ns, respectively; for a beam energy of 200 MeV and b) for energies E = 70, 100, and 120 MeV, respectively; for a pulse duration of 1 μs.

Jones *et al.* measured the acoustic signals produced by cyclotron generated proton spills in a clinical setting [138]. They measured the amplitude of acoustic wave as 4, 8, 11, 17, 20, 25 mPa for the proton numbers of $N_p = 1.2 \times 10^7, 2.9 \times 10^7, 3.9 \times 10^7, 7.0 \times 10^7, 9.1 \times 10^7$, and 12×10^7, respectively. We compare our results for a beam having the same energy and the spill time (230 MeV, 18 μs). Corresponding pressure values for equivalent proton numbers are found to be 5, 11, 15, 27, 36, and 47 mPa, respectively; and these results are in a good accordance with Jones *et al.*'s study [138]. The slight differences in amplitudes can be a consequence of beam diameter variations, in addition to this; the attenuation between the source and detector is not taken into account for our simulations.

Hayakawa *et al.* delivered 0.05 Gy dose to an excised muscle through a proton beam having a pulse duration of 50 ns which was delivered with an interval of 50 ms and measured the amplitude of pressure as 1.3 Pa [143]. The corresponding situation in our simulations is for a proton beam of 50 MeV energy with 4×10^6 particle number inducing a pressure of 2.90 Pa.

Tada *et al.* measured acoustic signals induced by protons in water [144]. The pulsed proton beam with a duration of 50 ns was modulated for the ranges of 51 and 81 mm and delivered to the phantom with an interval of 50 ms. They measured the amplitude of acoustic wave as 0.12 Pa for the beam delivering 0.4 cGy/pulse at the Bragg peak. The comparative situation for our simulations is for a beam having the same ranges corresponding to an approximate of 80 and 103 MeV, respectively; with 1.50 cm spot size and 100 ns pulse duration. In our work, the amplitude of acoustic wave is found to be 0.33 Pa for 4×10^6 protons depositing 0.4 cGy/pulse.

Alsanea *et al.* simulated proton induced acoustic waves. The pulse duration was 1 μs with the number of protons per pulse $N_p = 8 \times 10^6$. For a beam energy of 172.4 MeV, delivered dose and the amplitude of the acoustic wave were reported as 0.4 cGy and 0.14 Pa, respectively [153]. The corresponding result in our simulation agrees reasonably well for a beam having the same energy, number of protons and pulse duration, the amplitude of acoustic wave is calculated as 0.44 Pa.

The results of experimental and simulation studies are compared with ours for various parameters and these are summarized in Table 6.2.

Dose delivered to the patient depends on the number of protons. To assess the influence of the beam energy on the dose, we investigate several beam energies. We plot the dose in cGys versus the beam energy in which we change the proton number. Specifically, we assign proton numbers such that they represent real proton beams used in the therapy facilities [191, 197]. Linear relationship between proton beam intensity and hydrophone signal can be seen in Fig. 6.6. Debonis also showed the same linear relationship [149]. The linear relationship and the values of pressure amplitudes are also in a good agreement with Sulak *et al.*'s and Alsanea *et al.*'s studies [142, 153]. Bortfeld's model is used without fitting in dose calculations, even the effect is minor, this is one of the limitations of this work [158].

Table 6.2. Comparison of experimental and simulation studies' results with this work's for various parameters. PN: Proton number, PD: Pulse duration, BE: Beam Energy.

		Dose (cGy)	PN ($\times 10^6$)	BE (MeV)	PD	Pressure (Pa)
Experimental Studies Performed in a Clinical Setting	Hayakawa *et al.* [145]	0.3	NA	NA	50 ns	0.300
	This work	0.3	3.5	100	50 ns	0.280
	Jones *et al.* [138]	NA	12	230	18 μs	0.004
	This work	1.3	12	230	18 μs	0.005
Experimental and Simulation Studies	Sulak *et al.* [142]	NA	8.0	158	50 μs	0.010
	This work	6.0	8.0	158	10 μs	0.012
	Hayakawa *et al.* [143]	5.0	NA	NA	50 ns	1.30
	This work	4.7	12	50	50 ns	2.90
	Tada *et al.* [144]	0.4	NA	NA	50 ns	0.12
	This work	0.4	4.0	50	50 ns	0.33
Simulation Studies	Alsanea *et al.* [153]	1.00	8.0	172.4	1 μs	0.14
	This work	0.85	8.0	172.4	1 μs	0.44
	Ahmad *et al.* [152]	2.00	4.9	100	0.1 μs	0.10
	This work	0.90	4.9	100	1.0 μs	0.14
	This work	0.90	4.9	100	0.1 μs	0.77

The amplitude of the acoustic wave is another important parameter to be taken into account when proton acoustics is implemented in clinical studies. Pressures in the order of a few Pascals are difficult to measure instrumentally which is one of the main challenges to monitor dose through acoustics. Nevertheless, several medical experiments authenticated the detection is possible [143–145, 198]. Accumulation of signals and noise reduction techniques such as usage of filters, less noisy preamplifiers and electrostatic shielding are required for measuring waveforms of such small amplitudes. Figures 6.4 and 6.5 show the dependence of the beam energy and pulse duration on the amplitude of the pressure wave, respectively. Both parameters drastically change the amplitude of the signal. The simulations show that increasing beam energy causes a sharp rise in the amplitude of acoustic wave. Notwithstanding noise modelling is out of the scope of this work, it should be noted that higher noise level is expected as a result of the less sharp spatial dose deposition. Likewise, pulse duration also has a considerable effect on the signal amplitude. Smaller pulse duration is desirable to achieve the highest signal to noise ratio when number of protons is constant [199]. Compressing protons in a shorter period of time significantly enhances the signal amplitude. For a pulse duration smaller than 50 ns, the change in the amplitude is not significant. Stress confinement condition must be met to prevent the broadening of the proton acoustic signal and a decrease in the peak pressure amplitude. Most of the accelerators produce pulse duration between ms to ns. Pulse duration in the order of nanoseconds is used especially in a medical experiment regarding dose monitoring by acoustic waves [145]. That experiment advocates the benefits of using such small pulse duration which is in harmony with the results of our simulations. Moreover, pulse duration does not directly change the dose. In the case of varying proton number, the effect of pulse duration depends on its order. The amplitude of pressure wave increases with the pulse duration when spill time is on the order of nanoseconds as shown also by [142, 154]. However, the amplitude of pressure wave decreases with the pulse duration when spill time is on the order of microseconds since the effect of pulse duration has much more influence on the acoustic wave than increased proton number. Moreover, the effect of pulse duration and the beam width of the proton beam on the frequency of the acoustic wave is negligible, and hence it does not alter the selection of the central frequency

of detector. The frequency of the respiration and blood circulation is smaller than 10 kHz, thereby has no impact on the signal but a shift [143].

Widely used and favorable accelerators in proton therapy centers worldwide are synchrotrons and cyclotrons [200]. Besides, novel accelerator technologies are also considered and being tested for therapeutic applications [201]. One of the accelerator technologies is fixed-field alternating-gradients (FFAG) which combine both cyclotrons' time-independent magnetic field and synchrotrons' alternating gradient structure. However, FFAGs are not considered as the primary accelerator choice because of high costs and necessity of large space [202]. Dielectric wall accelerators (DWA) have been used in cancer therapy lately because of their low cost and small footprint [191]. DWA is basically a modified linear accelerator (LINAC) system which is patented in 1990s [203]. Another recently suggested accelerator type is laser-driven ones which gained interest because of their inexpensive structures and freely adjustable beam parameters [204].

However, the beam extracted from an accelerator nozzle cannot be used for treatment without further modifications. In contemplation of covering a target volume and creating a spread-out Bragg peak (SOBP), beam modifying devices are required. Range shifting instruments are necessary for decreasing the beam energy and hence range. There may be some issues such as scattering and reduction in the particle number. Nevertheless, these problems can be overcome by choosing a most suitable material [198,205]. For complicated target shapes, a patient specific compensator (bolus) can be used to control the beam through the field of interest [198, 206]. The bolus system is followed by spot scanning system which makes it possible to have a radiation field of any desired shape and intensity with the reduced fluctuation [207]. Furthermore, the pulsed proton beams via continuous wave cyclotrons can easily be achieved with the help of a beam chopper providing an adjustable pulse width that helps generation of detectable acoustic signals [208].

Current developments both in therapy accelerator design and beam modifying devices, such as choppers, can increase signal to noise ratio (SNR) of acoustic waveforms enabling desired modifications on beam profile [208]. Synchrocyclotron accelerators offer substantially more protons per pulse than conventional cyclotrons that can increase the signal amplitude and reduce treatment time by delivering more doses [209]. Newly emerging single room proton therapy systems may be a more compact solution that also can reduce the cost of construction considerably by optimizing economics of proton therapy [210]. Recently, a compact laser-based accelerator has also been proposed to reduce the rather high installation cost [204]. This new acceleration technique has an expected high pulse intensity of more than 10^8 particles/ns [154]. This may clearly enhance the SNR, yet there is a limitation for dose deposition in tissue.

The beam delivery method is also important for proton therapy [211]. Two available methods are the passive scattering and the active scattering. In passive scattering the proton beam is spread over the target by using scattering materials [201]. Scattering from the material provides both the broadening and uniformity of the proton beam. The spread-out-Bragg-peak is obtained via the modulator wheel. In passive scattering systems, obtaining the pulsed proton beam and measurement of the acoustic wave would be technically challenging due the modulator wheel. In active scattering, a magnetic scanner is used to deflect the proton beam and delivery is more flexible.

Tissue heterogeneities cause slight variations in the speed of acoustic waves. However, position dependent speed results in a nonlinear wave equation that is considerably harder to solve. In addition to this, acoustic attenuation also depends on the tissue composition and it becomes dominant in high frequencies. As shown in Figure 6.7, the frequency of the induced acoustic wave is less than 1 MHz for the beam parameters used in the literature. In this scenario, the variations in the attenuation can be neglected. Thermal noise sets a fundamental limit on the lowest detectable acoustic signal. Thermal noise presents in both the medium and the detector. The root of the thermal noise is the acoustic black body radiation. At room temperature, this is around k_BT=10-20 W/Hz [32]. For ultrasonic transducers, this corresponds to microPascals. However, in

a recent study, Ahmad *et al.* have investigated the thermal noise in a realistic PZT ultrasound transducer (5 cm diameter) and presented that noise could be as high as milliPascals [152].

The shape of the beam is considered Gaussian, yet it is an approximation. However, in practice, there may be some irregularities in the shape of the beam. Therefore, shaping beam with a collimator is crucial for dose monitoring via acoustics.

7. CONCLUSION

In order to evaluate the performance of the developed laser system, pulse energy, average power and repetition rate values are compared with the ones in existing systems within the literature including fiber components and independent of seeding laser type. The tunable fiber-based laser system has three outputs; supercontinuum (from 450 to 1100 nm), 1064 nm from single-wavelength emitting port, and harmonic generation (532, 355, and 266 nm). The average power of 1064 nm output is around 3 W which seeds harmonic generation unit but also can be used for its own applications. The maximum average power values of SHG (532 nm), third harmonic generation (THG, 355 nm), and fourth harmonic generation (FHG, 266 nm) are 500, 3, 10 mW, respectively. Total output power of supercontinuum is measured over 1 W with visible output power around 270 mW with a powermeter (S314C, Thorlabs) at 65 kHz repetition rate that corresponds to 17 μJ total and 4 μJ visible energy. Various bandpass filters are used to obtain wavelength of interest from supercontinuum output and power measurements are performed to compare with the values in the literature. In order not to damage bandpass filters, a 1000 nm shortpass filter is firstly employed. Average power values at wavelengths of 680 and 830 nm with 10 nm bandwidths are measured as 5 and 11 mW by a powermeter (S142C, Thorlabs) after the achromatic lens that corresponds to 76 and 169 nJ pulse energy. For wider bandwidths, average power values for wavelengths of 650, 697, 732, 785, and 880 nm with 80, 75, 68, 62, and 70 nm bandwidths are 92, 93, 82, 84, 142 mW, respectively. Corresponding pulse energies are 1.4, 1.4, 1.3, 1.3, 2.2 μJ. These energies are higher than the ones produced through coupling the output of Q-switched Nd:YAG microchip laser to PCF which is at most 33 nJ [40]. As mentioned above, for the special case of tapered PCFs, visible output energy was reported as 6 μJ at 25 kHz, for our system that is 4 μJ at 65 kHz and comparable to that output [43, 49]. In addition to that, our laser source can provide higher pulse repetition rate, up to 1 MHz, at the expense of lower pulse energies. For the systems utilizing SRS, the energies per band were reported several hundreds of nJs with an utmost energy of 500 nJ [50, 52]. SRS peaks are produced with a bandwidth around

10 nm, pulse energies are higher than our system for such narrow bandwidths for visible region. However, when filters with wider bandwidths are selected, pulse energies become higher than ones that SRS peaks possess. To be also noted, pulse energies of SRS peaks decreases (estimated around 100 nJ) elongating near-infrared spectral region. The edge of peaks was noted as 788 nm [50], our spectrum covers up to 1100 nm. Allen *et al.* [67] produced an all-fiber laser source with a PRF up to 2 MHz but the output wavelength was fixed. Mahmud *et al.* [68] also reported a fiber based laser source. By means of electronic modulations in the oscillator, tuning the repetition rate (0.1-120 MHz), the pulse-width (0.1-5 ns) and the wavelength (1030-1080 nm) were carried out. Green light was also generated through frequency doubling. The output power was reported up to 1.1 W and pulse energy up to 500 nJ. However, wavelength can not be tuned in a broad range which does not allow for various spectroscopic photoacoustic applications. There are many other advantages of our system. All the laser parameters, which are reported as independently adjustable, could be achieved by changing FPGA configuration and currents to the pump diodes electronically without any mechanical intervention. The only exception to this is the switching among the supercontinuum and harmonic generation ports, which is achieved by a mechanically switchable mirror, that can also readily be motorized, if desired. In addition to this, it is very compact with dimensions of $40\times40\times9$ cm^3 except from free-space harmonic generation unit and does not require any big cooling unit. Thanks to its high PRF, it may be a promising source for cytometry as well [65].

In our system, the light is transmitted through the splice between Yb-doped fiber and PCF for rendering all-fiber integrity with an efficiency of 40%. One of the disadvantage of current configuration is the heating at the splice point. Despite the cooling fan, the splice should be renewed once in a while in order to compansate for decreasing power in time. In order to handle the issue for robust and long-term operation, the splicing between the gain fiber and the PCF is optimised for low-loss and high tensile strength (using GPX-3000 series splicer, Vytran, Inc.), as demonstrated in the context of in-situ absorption spectroscopy of plasmas using a similar supercontinuum source and the same type of fibre [212]. Free space coupling is also possible between Yb-doped

fiber and PCF; in that case transmission can be performed with higher efficiency and higher pulse energies can be produced if all-fiber integrity is disregarded. The present limitations to the continuously and independently adjustable laser parameters arise from the requirement of simultaneous satisfaction of the following conditions during laser design: ensuring that each amplification stage is seeded with sufficient power to prevent generation of laser noise in the form of amplified spontaneous emission (ASE), ensuring that the targeted, final pulse duration will depend on the seed pulse duration in a complex manner due to gain saturation and that there is sufficient peak power to accomplish the supercontinuum generation in the PCF. We believe that even a large range of parameters are possible, albeit at the cost of increased system complexity (by adding a second AOM and additional amplifier stages). The present parameter range was decided based on the balance between system complexity and sufficiency for most typical OR-PAM applications.

When all-fiber based laser systems are taken into consideration, the developed system improves the wavelength tunability with a repetition rate up to 1 MHz. For laser systems having fiber components, pulse energies of this system are higher from PCF coupled supercontinuum cases and comparable to the outputs of special tapered PCF designs. The system also offers all-fiber integrity and higher PRF by means of custom developed FPGA electronics controlling laser diode. Pulse energies of SRS peaks can be surpassed at near-infrared region with same bandwidth, at visible region only by using filters with wider bandwidths. This system may provide the means of spectroscopic photoacoustic microscopy applications via widely tunable fiber laser technologies.

In the analyses about proton-induced acoustic waves, our results show that the smaller spill time of the proton beam upsurges the amplitude of the acoustic wave for a constant number of protons, which is hence beneficial for dose monitoring. In the case of a varying proton number, the amplitude of the pressure wave increases with the pulse duration when the spill time is on the order of nanoseconds. However, the amplitude of the pressure wave decreases as the pulse duration increases when the spill time is on the

order of microseconds, since the effect of pulse duration on the acoustic wave prevails over the effect of an increased proton number. The amplitude of a pressure wave has a linear relationship with the proton number and energy deposition. The increase in the energy of each individual proton in the beam leads to the spatial broadening of the Bragg curve, which also yields acoustic waves of greater amplitude. The pulse duration and the beam width of the proton beam do not affect the central frequency of the acoustic wave, but they change the amplitude of the spectral components.

Although our study presents a model to investigate the relationship between the properties of the proton beam and the induced acoustic wave parameters, this model can be used to solve an inverse acoustic source problem in the future. That will lead to mapping of the acoustic source distribution which is directly related to radiation dose. Hence, this work may pave the way towards a useful tool for real time dose measurements in proton therapy.

We have obtained an analytic expression for the velocity field and scalar potential of the velocity field for the first time to express photoacoustic radiation force on incompressible spheres. These analyses are crucial for using a trapped particle as a sound wave detector. We also demonstrated that the hybrid optical tweezers and photoacoustic microscopy system would be useful in listening ultra quiet sound resources. High-frequency components of photoacoustic waves are lost during detection since they attenuate very fast (i.e., ultrasound softening). This hybrid system would be useful for getting information about those components as well since it is possible to put a trapped particle very close to the absorber and ultrasound wave would reach it before attenuating. By designing multiple optical traps with scanning galvo-mirrors or spatial light modulators, several particles can be trapped and also utilized for the localization of the photoacoustic wave sources by means of a triangulation system. We showed that it is possible to get information about the amplitude of the photoacoustic wave by courtesy of that distinct sound power levels resulted in different FFT amplitudes of the particle's trajectories. In conclusion, we have performed proof of concept experiments demonstrating how a single optically trapped particle can be used in photoacoustic

wave detection and put forth an alternative detector that has the potential to increase the sensitivity of the minimum detectable sound power level.

REFERENCES

1. Ranka, J. K., R. S. Windeler and A. J. Stentz, "Optical properties of high-delta air–silica microstructure optical fibers", *Optics letters*, Vol. 25, No. 11, pp. 796–798, 2000.

2. Dudley, J. M., G. Genty and S. Coen, "Supercontinuum Generation in Photonic Crystal Fiber", *Reviews of Modern Physics*, Vol. 78, No. 4, p. 1135, 2006.

3. Mameren, J. V., *The Member Magazine of the Institute of Physics*, 2008, `http://physicsworld.com/cws/article/indepth/2008/nov/13/optical-tweezers-where-physics-meets-biology`, accessed at July 2017.

4. Bell, A. G., "On the Production and Reproduction of Sound by Light", *American Journal of Science*, Vol. 1, No. 118, pp. 305–324, 1880.

5. Xu, M. and L. V. Wang, "Photoacoustic Imaging in Biomedicine", *Review of Scientific Instruments*, Vol. 77, No. 4, p. 041101, 2006.

6. Harrison, T., J. C. Ranasinghesagara, H. Lu, K. Mathewson, A. Walsh and R. J. Zemp, "Combined Photoacoustic and Ultrasound Biomicroscopy", *Optics Express*, Vol. 17, No. 24, pp. 22041–22046, 2009.

7. Wang, L. V., "Tutorial on Photoacoustic Microscopy and Computed Tomography", *IEEE Journal of Selected Topics in Quantum Electronics*, Vol. 14, No. 1, pp. 171–179, 2008.

8. Wang, L. V., "Multiscale Photoacoustic Microscopy and Computed Tomography", *Nature Photonics*, Vol. 3, No. 9, pp. 503–509, 2009.

9. Hu, S. and L. V. Wang, "Optical-resolution Photoacoustic Microscopy: Auscultation of Biological Systems at the Cellular Level", *Biophysical Journal*, Vol. 105,

No. 4, pp. 841–847, 2013.

10. Zhang, H. F., K. Maslov, G. Stoica and L. V. Wang, "Functional Photoacoustic Microscopy for High-resolution and Noninvasive In-vivo Imaging", *Nature Biotechnology*, Vol. 24, No. 7, pp. 848–851, 2006.

11. Maslov, K., H. F. Zhang, S. Hu and L. V. Wang, "Optical-resolution Photoacoustic Microscopy for In-vivo Imaging of Single Capillaries", *Optics Letters*, Vol. 33, No. 9, pp. 929–931, 2008.

12. Li, G., K. I. Maslov and L. V. Wang, "Reflection-mode Multifocal Optical-resolution Photoacoustic Microscopy", *Journal of Biomedical Optics*, Vol. 18, No. 3, pp. 030501–030501, 2013.

13. Xie, Z., W. Roberts, P. Carson, X. Liu, C. Tao and X. Wang, "Evaluation of Bladder Microvasculature with High-resolution Photoacoustic Imaging", *Optics Letters*, Vol. 36, No. 24, pp. 4815–4817, 2011.

14. Li, C. and L. V. Wang, "Photoacoustic Tomography and Sensing in Biomedicine", *Physics in Medicine and Biology*, Vol. 54, No. 19, p. R59, 2009.

15. Wang, L. V., X. Zhao, H. Sun and G. Ku, "Microwave-induced Acoustic Imaging of Biological Tissues", *Review of Scientific Instruments*, Vol. 70, No. 9, pp. 3744–3748, 1999.

16. Hutchins, D. and A. C. Tam, "Special Issue on Photoacoustics", *IEEE Transactions on Ultrasonics, Ferroelectrics, and Frequency Control*, Vol. 33, No. 5, pp. 427–428, 1986.

17. Beard, P., "Biomedical Photoacoustic Imaging", *Interface Focus*, Vol. 1, No. 4, pp. 602–631, 2011.

18. Kruger, R. A., P. Liu, C. R. Appledorn *et al.*, "Photoacoustic Ultrasound

(PAUS)−Reconstruction Tomography", *Medical Physics*, Vol. 22, No. 10, pp. 1605–1609, 1995.

19. Zhang, H. F., K. Maslov and L. V. Wang, "In-vivo Imaging of Subcutaneous Structures Using Functional Photoacoustic Microscopy", *Nature Protocols*, Vol. 2, No. 4, pp. 797–804, 2007.

20. Allen, T. J. and P. C. Beard, "Pulsed Near-infrared Laser Diode Excitation System for Biomedical Photoacoustic Imaging", *Optics Letters*, Vol. 31, No. 23, pp. 3462–3464, 2006.

21. Ku, G. and L. V. Wang, "Deeply Penetrating Photoacoustic Tomography in Biological Tissues Enhanced with an Optical Contrast Agent", *Optics Letters*, Vol. 30, No. 5, pp. 507–509, 2005.

22. Zeng, L., G. Liu, D. Yang and X. Ji, "3D-visual Laser-diode Based Photoacoustic Imaging", *Optics Express*, Vol. 20, No. 2, pp. 1237–1246, 2012.

23. Zeng, L., G. Liu, D. Yang and X. Ji, "Portable Optical-resolution Photoacoustic Microscopy with a Pulsed Laser Diode Excitation", *Applied Physics Letters*, Vol. 102, No. 5, p. 053704, 2013.

24. Zeng, L., G. Liu, D. Yang and X. Ji, "Cost-efficient Laser Diode Induced Optical-Resolution Photoacoustic Microscopy for Two-dimensional/Three-dimensional Biomedical Imaging", *Journal of Biomedical Optics*, Vol. 19, No. 7, p. 076017, 2014.

25. Wang, T., S. Nandy, H. S. Salehi, P. D. Kumavor and Q. Zhu, "A Low-cost Photoacoustic Microscopy system with a Laser Diode Excitation", *Biomedical Optics Express*, Vol. 5, No. 9, pp. 3053–3058, 2014.

26. Kolkman, R. G., W. Steenbergen and T. G. van Leeuwen, "In-vivo Photoacoustic Imaging of Blood Vessels with a Pulsed Laser Diode", *Lasers in Medical Science*,

Vol. 21, No. 3, pp. 134–139, 2006.

27. Zeng, L., Z. Piao, S. Huang, W. Jia and Z. Chen, "Label-free Optical-resolution Photoacoustic Microscopy of Superficial Microvasculature Using a Compact Visible Laser Diode Excitation", *Optics Express*, Vol. 23, No. 24, pp. 31026–31033, 2015.

28. Maslov, K., G. Stoica and L. V. Wang, "In-vivo Dark-field Reflection-mode Photoacoustic Microscopy", *Optics Letters*, Vol. 30, No. 6, pp. 625–627, 2005.

29. Favazza, C. P., O. Jassim, L. A. Cornelius and L. V. Wang, "In-vivo Photoacoustic Microscopy of Human Cutaneous Microvasculature and a Nevus", *Journal of Biomedical Optics*, Vol. 16, No. 1, pp. 016015–016015, 2011.

30. Li, L., R. J. Zemp, G. Lungu, G. Stoica and L. V. Wang, "Photoacoustic Imaging of LacZ Gene Expression In-vivo", *Journal of Biomedical Optics*, Vol. 12, No. 2, pp. 020504–020504, 2007.

31. Krumholz, A., S. J. VanVickle-Chavez, J. Yao, T. P. Fleming, W. E. Gillanders and L. V. Wang, "Photoacoustic Microscopy of Tyrosinase Reporter Gene In-vivo", *Journal of Biomedical Optics*, Vol. 16, No. 8, pp. 080503–080503, 2011.

32. Wang, T., Y. Yang, U. Alqasemi, P. D. Kumavor, X. Wang, M. Sanders, M. Brewer and Q. Zhu, "Characterization of Ovarian Tissue Based on Quantitative Analysis of Photoacoustic Microscopy Images", *Biomedical Optics Express*, Vol. 4, No. 12, pp. 2763–2768, 2013.

33. Song, K. H. and L. V. Wang, "Deep Reflection-mode Photoacoustic Imaging of Biological Tissue", *Journal of Biomedical Optics*, Vol. 12, No. 6, pp. 060503–060503, 2007.

34. Song, K. H., C. Kim, K. Maslov and L. V. Wang, "Noninvasive In-vivo Spectroscopic Nanorod-contrast Photoacoustic Mapping of Sentinel Lymph Nodes",

European Journal of Radiology, Vol. 70, No. 2, pp. 227–231, 2009.

35. Yao, D.-K., R. Chen, K. Maslov, Q. Zhou and L. V. Wang, "Optimal Ultraviolet Wavelength for In-vivo Photoacoustic Imaging of Cell Nuclei", *Journal of Biomedical Optics*, Vol. 17, No. 5, pp. 0560041–0560047, 2012.

36. Li, C., A. Aguirre, J. Gamelin, A. Maurudis, Q. Zhu and L. V. Wang, "Real-time Photoacoustic Tomography of Cortical Hemodynamics in Small Animals", *Journal of Biomedical Optics*, Vol. 15, No. 1, pp. 010509–010509, 2010.

37. Ai, M., W. Shu, T. Salcudean, R. Rohling, P. Abolmaesumi and S. Tang, "High Energy Laser Pulse Coupling in a Multimode Fiber for Photoacoustic Tomography", *Proceedings of International Society for Optics and Photonics*, pp. 97084H–97084H, 2016.

38. Cao, R., J. P. Kilroy, B. Ning, T. Wang, J. A. Hossack and S. Hu, "Multispectral Photoacoustic Microscopy Based on an Optical–acoustic Objective", *Photoacoustics*, Vol. 3, No. 2, pp. 55–59, 2015.

39. Zhang, C., K. Maslov, J. Yao and L. V. Wang, "In-vivo Photoacoustic Microscopy with 7.6-μm Axial resolution using a Commercial 125-MHz Ultrasonic Transducer", *Journal of Biomedical Optics*, Vol. 17, No. 11, pp. 116016–116016, 2012.

40. Billeh, Y. N., M. Liu and T. Buma, "Spectroscopic Photoacoustic Microscopy Using a Photonic Crystal Fiber Supercontinuum Source", *Optics Express*, Vol. 18, No. 18, pp. 18519–18524, 2010.

41. Lee, C., S. Han, S. Kim, M. Jeon, M. Y. Jeon, C. Kim and J. Kim, "Combined Photoacoustic and Optical Coherence Tomography Using a Single Near-infrared Supercontinuum Laser Source", *Applied Optics*, Vol. 52, No. 9, pp. 1824–1828, 2013.

42. Lee, C., M. Jeon, M. Y. Jeon, J. Kim and C. Kim, "In-vitro Photoacoustic Mea-

surement of Hemoglobin Oxygen Saturation Using a Single Pulsed Broadband Supercontinuum Laser Source", *Applied Optics*, Vol. 53, No. 18, pp. 3884–3889, 2014.

43. Shu, X., M. Bondu, B. Dong, A. Podoleanu, L. Leick and H. F. Zhang, "Single All-fiber-based Nanosecond-pulsed Supercontinuum Source for Multispectral Photoacoustic Microscopy and Optical Coherence Tomography", *Optics Letters*, Vol. 41, No. 12, pp. 2743–2746, 2016.

44. Loya, A. K., J. Dumas and T. Buma, "Photoacoustic Microscopy with a Tunable Source Based on Cascaded Stimulated Raman Scattering in a Large-mode Area Photonic Crystal Fiber", *Proceedings of IEEE International Ultrasonics Symposium*, pp. 1208–1211, 2012.

45. Koeplinger, D., M. Liu and T. Buma, "Photoacoustic Microscopy with a Pulsed Multi-color Source Based on Stimulated Raman Scattering", *Proceedings of IEEE International Ultrasonics Symposium*, pp. 296–299, 2011.

46. Ferrari, M. R., J. L. Farland and T. Buma, "Photoacoustic Microscopy Using Four-wave Mixing in a Multimode Fiber", *Proceedings of IEEE International Ultrasonics Symposium*, pp. 1–4, 2015.

47. Buma, T., B. C. Wilkinson and T. C. Sheehan, "Near-infrared Spectroscopic Photoacoustic Microscopy Using a Multi-color Fiber Laser Source", *Biomedical Optics Express*, Vol. 6, No. 8, pp. 2819–2829, 2015.

48. Liu, M. and T. Buma, "Wavelength Agile Photoacoustic Microscopy with a Photonic Crystal Fiber Supercontinuum Source", *Proceedings of International Society for Optics and Photonics*, pp. 789944–789944, 2011.

49. Bondu, M., C. Brooks, C. Jakobsen, K. Oakes, P. M. Moselund, L. Leick, O. Bang and A. Podoleanu, "High Energy Supercontinuum Sources Using Tapered Pho-

tonic Crystal Fibers for Multispectral Photoacoustic Microscopy", *Journal of Biomedical Optics*, Vol. 21, No. 6, pp. 061005–061005, 2016.

50. Hajireza, P., A. Forbrich and R. Zemp, "In-vivo Functional Optical-Resolution Photoacoustic Microscopy with Stimulated Raman Scattering Fiber-laser Source", *Biomedical Optics Express*, Vol. 5, No. 2, pp. 539–546, 2014.

51. Hajireza, P., A. Forbrich, Y. Jiang, W. Shi and R. Zemp, "In-vivo Multi-wavelength Optical-resolution Photoacoustic Microscopy with Stimulated Raman Scattering Fiber-laser Source", *Proceedings of SPIE BiOS*, pp. 858129–858129, 2013.

52. Hajireza, P., A. Forbrich and R. J. Zemp, "Multifocus Optical-resolution Photoacoustic Microscopy Using Stimulated Raman Scattering and Chromatic Aberration", *Optics Letters*, Vol. 38, No. 15, pp. 2711–2713, 2013.

53. Serebryannikov, E. and A. Zheltikov, "Supercontinuum Generation Through Cascaded Four-wave Mixing in Photonic-crystal Fibers: When Picoseconds Do it Better", *Optics Communications*, Vol. 274, No. 2, pp. 433 – 440, 2007.

54. Boucon, A., T. Sylvestre, K. Huy, J. Beugnot, G. Mélin, H. Maillotte and J. Dudley, "Supercontinuum Generation by Nanosecond Dual-Pumping Near the Two Zero-dispersion Wavelengths of a Photonic Crystal Fiber", *Optics Communications*, Vol. 284, No. 1, pp. 467 – 470, 2011.

55. Wadsworth, W., N. Joly, J. Knight, T. Birks, F. Biancalana and P. Russell, "Supercontinuum and Four-wave Mixing with Q-switched Pulses in Endlessly Single-mode Photonic Crystal Fibres", *Optics Express*, Vol. 12, No. 2, pp. 299–309, 2004.

56. Dudley, J. M., L. Provino, N. Grossard, H. Maillotte, R. S. Windeler, B. J. Eggleton and S. Coen, "Supercontinuum Generation in Air–silica Microstructured

Fibers with Nanosecond and Femtosecond Pulse Pumping", *Journal of the Optical Society of America B*, Vol. 19, No. 4, pp. 765–771, 2002.

57. Møller, U., S. T. Sørensen, C. Larsen, P. M. Moselund, C. Jakobsen, J. Johansen, C. L. Thomsen and O. Bang, "Optimum PCF Tapers for Blue-enhanced Supercontinuum Sources", *Optical Fiber Technology*, Vol. 18, No. 5, pp. 304–314, 2012.

58. Stone, J. M. and J. C. Knight, "Visibly "White" Light Generation in Uniform Photonic Crystal Fiber Using a Microchip Laser", *Optics Express*, Vol. 16, No. 4, pp. 2670–2675, 2008.

59. Sorensen, S. T., U. Moller, C. Larsen, P. Moselund, C. Jakobsen, J. Johansen, T. Andersen, C. Thomsen and O. Bang, "Deep-blue Supercontinnum Sources with Optimum Taper Profiles–verification of GAM", *Optics Express*, Vol. 20, No. 10, pp. 10635–10645, 2012.

60. Shi, W., P. Hajireza, P. Shao, A. Forbrich and R. J. Zemp, "In-vivo Near-realtime Volumetric Optical-resolution Photoacoustic Microscopy Using a High-repetition-rate Nanosecond Fiber-laser", *Optics Express*, Vol. 19, No. 18, pp. 17143–17150, 2011.

61. Shi, W., P. Shao, P. Hajireza, A. Forbrich and R. J. Zemp, "In-vivo Dynamic Process Imaging Using Real-time Optical-resolution Photoacoustic Microscopy", *Journal of Biomedical Optics*, Vol. 18, No. 2, pp. 026001–026001, 2013.

62. Hajireza, P., W. Shi and R. Zemp, "Label-free In-vivo Fiber-based Optical-resolution Photoacoustic Microscopy", *Optics Letters*, Vol. 36, No. 20, pp. 4107–4109, 2011.

63. Shi, W., S. Kerr, I. Utkin, J. Ranasagara, L. Pan, Y. Godwal, R. J. Zemp and R. Fedosejevs, "OR-PAM using Novel High-repetition-rate Q-switched Microchip Lasers", *Journal of Biomedical Optics*, Vol. 15, No. 5, pp. 056017–056017, 2010.

64. Wang, Y., K. Maslov, Y. Zhang, S. Hu, L. Yang, Y. Xia, J. Liu and L. V. Wang, "Fiber-laser-based Photoacoustic Microscopy and Melanoma Cell Detection", *Journal of Biomedical Optics*, Vol. 16, No. 1, 2011.

65. Nedosekin, D. A., M. Sarimollaoglu, E. V. Shashkov, E. I. Galanzha and V. P. Zharov, "Ultra-fast Photoacoustic Flow Cytometry with a 0.5 MHz Pulse Repetition Rate Nanosecond Laser", *Optics Express*, Vol. 18, No. 8, pp. 8605–8620, 2010.

66. Piao, Z., L. Zeng, Z. Chen and C.-S. Kim, "Q-switched Erbium-doped Fiber Laser at 1600 nm for Photoacoustic Imaging Application", *Applied Physics Letters*, Vol. 108, No. 14, p. 143701, 2016.

67. Allen, T., M. Berendt, J. Spurrell, S. Alam, E. Zhang and P. Richardson, DJ and, "Novel Fibre Lasers as Excitation Sources for Photoacoustic Tomography and Microscopy", *Proceedings of SPIE BiOS*, pp. 97080W–97080W, 2016.

68. Mahmud, M. S., A. Forbrich, P. Shao, W. Shi and R. J. Zemp, "A Tunable MOPA for Optical r-Resolution Photoacoustic Microscopy", *Proceedings of SPIE BiOS*, pp. 93233V–93233V, 2015.

69. Chen, H., S. Chen, J. Wang, Z. Chen and H. J, "35 W High Power All Fiber Supercontinuum Generation in PCF with Picosecond MOPA Laser", *Optics Communications*, Vol. 284, No. 23, pp. 5484 – 5487, 2011.

70. Ilday, F. Ö., H. Lim, J. Buckley and F. Wise, "Practical All-fiber Source of High-power, 120-fs Pulses at 1 μm", *Optics Letters*, Vol. 28, No. 15, pp. 1362–1364, 2003.

71. Yao, D.-K., K. Maslov, K. K. Shung, Q. Zhou and L. V. Wang, "In-vivo Label-free Photoacoustic Microscopy of Cell Nuclei by Excitation of DNA and RNA", *Optics Letters*, Vol. 35, No. 24, pp. 4139–4141, 2010.

72. Ashkin, A., J. M. Dziedzic, J. Bjorkholm and S. Chu, "Observation of a Single-beam Gradient Force Optical Trap for Dielectric Particles", *Optics Letters*, Vol. 11, No. 5, pp. 288–290, 1986.

73. Ashkin, A., J. M. Dziedzic and T. Yamane, "Optical Trapping and Manipulation of Single Cells Using Infrared Laser Beams", *Nature*, Vol. 330, No. 6150, pp. 769–771, 1987.

74. Maier, S. A., *Plasmonics: Fundamentals and Applications*, Springer Science & Business Media, 2007.

75. Neuman, K. C. and S. M. Block, "Optical Trapping", *Review of Scientific Instruments*, Vol. 75, No. 9, pp. 2787–2809, 2004.

76. Kendrick, M., D. McIntyre and O. Ostroverkhova, "Wavelength Dependence of Optical Tweezer Trapping Forces on Dye-doped Polystyrene Microspheres", *Journal of the Optical Society of America B*, Vol. 26, No. 11, pp. 2189–2198, 2009.

77. Ashkin, A., "Forces of a Single-beam Gradient Laser Trap on a Dielectric Sphere in the Ray Optics Regime", *Biophysical Journal*, Vol. 61, No. 2, pp. 569–582, 1992.

78. Stratton, J. A., *Electromagnetic Theory*, John Wiley & Sons, 2007.

79. Kerker, M., *The Scattering of Light and Other Electromagnetic Radiation*, Elsevier, 2016.

80. Harada, Y. and T. Asakura, "Radiation Forces on a Dielectric Sphere in the Rayleigh Scattering Regime", *Optics Communications*, Vol. 124, No. 5-6, pp. 529–541, 1996.

81. Liang, H., K. T. Vu, P. Krishnan, T. C. Trang, D. Shin, S. Kimel and M. W. Berns, "Wavelength Dependence of Cell Cloning Efficiency after Optical Trap-

ping", *Biophysical Journal*, Vol. 70, No. 3, pp. 1529–1533, 1996.

82. Schneckenburger, H., A. Hendinger, R. Sailer, M. H. Gschwend, W. S. Strauss, M. Bauer, K. Schu *et al.*, "Cell Viability in Optical Tweezers: High Power Red Laser Diode versus Nd: YAG Laser", *Journal of Biomedical Optics*, Vol. 5, No. 1, pp. 40–44, 2000.

83. Rohrbach, A., "Switching and Measuring a Force of 25 FemtoNewtons with an Optical Trap", *Optics Express*, Vol. 13, No. 24, pp. 9695–9701, 2005.

84. Andersson, M., E. Fällman, B. E. Uhlin and O. Axner, "A sticky Chain Model of the Elongation and Unfolding of Escherichia coli P pili under Stress", *Biophysical Journal*, Vol. 90, No. 5, pp. 1521–1534, 2006.

85. Wang, M. D., H. Yin, R. Landick, J. Gelles and S. M. Block, "Stretching DNA with Optical Tweezers", *Biophysical Journal*, Vol. 72, No. 3, pp. 1335–1346, 1997.

86. Clausen-Schaumann, H., M. Seitz, R. Krautbauer and H. E. Gaub, "Force Spectroscopy with Single Bio-molecules", *Current Opinion in Chemical Biology*, Vol. 4, No. 5, pp. 524–530, 2000.

87. Berg, H. C. and L. Turner, "Torque Generated by the Flagellar Motor of Escherichia Coli", *Biophysical Journal*, Vol. 65, No. 5, pp. 2201–2216, 1993.

88. Felgner, H., R. Frank and M. Schliwa, "Flexural Rigidity of Microtubules Measured with the Use of Optical Tweezers", *Journal of Cell Science*, Vol. 109, No. 2, pp. 509–516, 1996.

89. Whyte, G., G. Gibson, J. Leach, M. Padgett, D. Robert and M. Miles, "An Optical Trapped Micro-hand for Manipulating Micron-sized Objects", *Optics Express*, Vol. 14, No. 25, pp. 12497–12502, 2006.

90. Smith, S. B., Y. Cui and C. Bustamente, "Overstretching B-DNA: The Elastic

Response of Individual Double-stranded and Single-stranded DNA Molecules", *Science*, Vol. 271, No. 5250, p. 795, 1996.

91. Baumann, C. G., V. A. Bloomfield, S. B. Smith, C. Bustamante, M. D. Wang and S. M. Block, "Stretching of Single Collapsed DNA Molecules", *Biophysical Journal*, Vol. 78, No. 4, pp. 1965–1978, 2000.

92. Leger, J.-F., J. Robert, L. Bourdieu, D. Chatenay and J. F. Marko, "RecA Binding to a Single Double-stranded DNA Molecule: A Possible Role of DNA Conformational Fluctuations", *Proceedings of the National Academy of Sciences*, Vol. 95, No. 21, pp. 12295–12299, 1998.

93. Sakata-Sogawa, K., M. Kurachi, K. Sogawa, Y. Fujii-Kuriyama and H. Tashiro, "Direct Measurement of DNA Molecular Length in Solution Using Optical Tweezers: Detection of Looping due to Binding Protein Interactions", *European Biophysics Journal*, Vol. 27, No. 1, pp. 55–61, 1998.

94. Gore, J., Z. Bryant, M. Nöllmann, M. U. Le, N. R. Cozzarelli and C. Bustamante, "DNA Overwinds when Stretched", *Nature*, Vol. 442, No. 7104, pp. 836–839, 2006.

95. Lionnet, T., S. Joubaud, R. Lavery, D. Bensimon and V. Croquette, "Wringing out DNA", *Physical Review Letters*, Vol. 96, No. 17, p. 178102, 2006.

96. Williams, M. C., J. R. Wenner, I. Rouzina and V. A. Bloomfield, "Entropy and Heat Capacity of DNA Melting from Temperature Dependence of Single Molecule Stretching", *Biophysical Journal*, Vol. 80, No. 4, pp. 1932–1939, 2001.

97. Wenner, J. R., M. C. Williams, I. Rouzina and V. A. Bloomfield, "Salt Dependence of the Elasticity and Overstretching Transition of Single DNA Molecules", *Biophysical Journal*, Vol. 82, No. 6, pp. 3160–3169, 2002.

98. Bustamante, C., Y. R. Chemla, N. R. Forde and D. Izhaky, "Mechanical Processes in Biochemistry", *Annual Review of Biochemistry*, Vol. 73, No. 1, pp. 705–748,

2004.

99. Kinosita Jr, K., K. Adachi and H. Itoh, "Rotation of F1-ATPase: How an ATP-driven Molecular Machine may Work", *Annual Review of Biophysics and BiomolecularSstructure*, Vol. 33, pp. 245–268, 2004.

100. Mallik, R. and S. P. Gross, "Molecular Motors: Strategies to Get Along", *Current Biology*, Vol. 14, No. 22, pp. R971–R982, 2004.

101. Carter, N. J. and R. A. Cross, "Kinesin's Moonwalk", *Current Opinion in Cell Biology*, Vol. 18, No. 1, pp. 61–67, 2006.

102. Block, S. M., "Kinesin Motor Mechanics: Binding, Stepping, Tracking, Gating, and Limping", *Biophysical Journal*, Vol. 92, No. 9, pp. 2986–2995, 2007.

103. Seeger, S., S. Monajembashi, K.-J. Hutter, G. Futterman, J. Wolfrum and K. Greulich, "Application of Laser Optical Tweezers in Immunology and Molecular Genetics", *Cytometry Part A*, Vol. 12, No. 6, pp. 497–504, 1991.

104. Steubing, R. W., S. Cheng, W. H. Wright, Y. Numajiri and M. W. Berns, "Laser induced cell fusion in combination with optical tweezers: the laser cell fusion trap", *Cytometry Part A*, Vol. 12, No. 6, pp. 505–510, 1991.

105. Nightingale, K., M. S. Soo, R. Nightingale and G. Trahey, "Acoustic Radiation Force Impulse Imaging: In-vivo Demonstration of Clinical Feasibility", *Ultrasound in Medicine and Biology*, Vol. 28, No. 2, pp. 227–235, 2002.

106. Bercoff, J., M. Tanter and M. Fink, "Supersonic Shear Imaging: A New Technique for Soft Tissue Elasticity Mapping", *IEEE Transactions on Ultrasonics, Ferroelectrics, and Frequency Control*, Vol. 51, No. 4, pp. 396–409, 2004.

107. Tanter, M., J. Bercoff, A. Athanasiou, T. Deffieux, J.-L. Gennisson, G. Montaldo, M. Muller, A. Tardivon and M. Fink, "Quantitative Assessment of Breast

Lesion Viscoelasticity: Initial Clinical Results Using Supersonic Shear Imaging", *Ultrasound in Medicine and Biology*, Vol. 34, No. 9, pp. 1373–1386, 2008.

108. Muller, M., J.-L. Gennisson, T. Deffieux, M. Tanter and M. Fink, "Quantitative Viscoelasticity Mapping of Human Liver Using Supersonic Shear Imaging: Preliminary In-vivo Feasability Study", *Ultrasound in Medicine and Biology*, Vol. 35, No. 2, pp. 219–229, 2009.

109. Deffieux, T., J.-l. Gennisson, M. Tanter and M. Fink, "Assessment of the Mechanical Properties of the Musculoskeletal System Using 2-D and 3-D Very High Frame Rate Ultrasound", *IEEE Transactions on Ultrasonics, Ferroelectrics, and Frequency control*, Vol. 55, No. 10, pp. 2177–2190, 2008.

110. Walker, W. F., F. J. Fernandez and L. A. Negron, "A Method of Imaging Viscoelastic Parameters with Acoustic Radiation force", *Physics in Medicine and Biology*, Vol. 45, No. 6, p. 1437, 2000.

111. Dayton, P., A. Klibanov, G. Brandenburger and K. Ferrara, "Acoustic Radiation Force In-vivo: A Mechanism to Assist Targeting of Microbubbles", *Ultrasound in Medicine and Biology*, Vol. 25, No. 8, pp. 1195–1201, 1999.

112. Dayton, P. A., S. Zhao, S. H. Bloch, P. Schumann, K. Penrose, T. O. Matsunaga, R. Zutshi, A. Doinikov and K. W. Ferrara, "Application of Ultrasound to Selectively Localize Nanodroplets for Targeted Imaging and Therapy", *Molecular imaging*, Vol. 5, No. 3, pp. 7290–2006, 2006.

113. Hernot, S. and A. L. Klibanov, "Microbubbles in Ultrasound-triggered Drug-gene Delivery", *Advanced Drug Delivery Reviews*, Vol. 60, No. 10, pp. 1153–1166, 2008.

114. Zheng, X. and R. E. Apfel, "Acoustic Interaction Forces between Two Fluid Spheres in an Acoustic Field", *The Journal of the Acoustical Society of America*, Vol. 97, No. 4, pp. 2218–2226, 1995.

115. Löfstedt, R. and S. Putterman, "Theory of Long Wavelength Acoustic Radiation Pressure", *The Journal of the Acoustical Society of America*, Vol. 90, No. 4, pp. 2027–2033, 1991.

116. Lee, J., K. Ha and K. K. Shung, "A Theoretical Study of the Feasibility of Acoustical tweezers: Ray Acoustics Approach", *The Journal of the Acoustical Society of America*, Vol. 117, No. 5, pp. 3273–3280, 2005.

117. Coakley, W., J. Hawkes, M. Sobanski, C. Cousins and J. Spengler, "Analytical Scale Ultrasonic Standing Wave Manipulation of Cells and Microparticles", *Ultrasonics*, Vol. 38, No. 1, pp. 638–641, 2000.

118. Hawkes, J. J., R. W. Barber, D. R. Emerson and W. T. Coakley, "Continuous Cell Washing and Mixing Driven by an Ultrasound Standing Save within a Microfluidic Channel", *Lab on a Chip*, Vol. 4, No. 5, pp. 446–452, 2004.

119. King, L. V., "On the Acoustic Radiation Pressure on Spheres", *Proceedings of the Royal Society of London A: Mathematical, Physical and Engineering Sciences*, Vol. 147, pp. 212–240, The Royal Society, 1934.

120. Embleton, T., "Mean Force on a Sphere in a Spherical Sound Field. I. (Theoretical)", *The Journal of the Acoustical Society of America*, Vol. 26, No. 1, pp. 40–45, 1954.

121. Embleton, T., "The Radiation Force on a Spherical Obstacle in a Cylindrical Sound Field", *Canadian Journal of Physics*, Vol. 34, No. 3, pp. 276–287, 1956.

122. Yosioka, K. and Y. Kawasima, "Acoustic Radiation Pressure on a Compressible Sphere", *Acta Acustica united with Acustica*, Vol. 5, No. 3, pp. 167–173, 1955.

123. Wu, J. and G. Du, "Acoustic Radiation Force on a Small Compressible Sphere in a Focused Beam", *The Journal of the Acoustical Society of America*, Vol. 87, No. 3, pp. 997–1003, 1990.

124. Gorkov, L., "Forces Acting on a Small Particle in an Acoustic Field within an Ideal Fluid", *Doklady Akademii Nauk SSSR*, Vol. 140, No. 1, p. 88, 1961.

125. Peregrine, D., "The Acoustic Bubble.", *Journal of Fluid Mechanics*, Vol. 272, pp. 407–408, 1994.

126. Dayton, P. A., K. E. Morgan, A. L. Klibanov, G. Brandenburger, K. R. Nightingale and K. W. Ferrara, "A Preliminary Evaluation of the Effects of Primary and Secondary Radiation Forces on Acoustic Contrast Agents", *IEEE Transactions on Ultrasonics, Ferroelectrics, and Frequency Control*, Vol. 44, No. 6, pp. 1264–1277, 1997.

127. Zharov, V. P. and V. S. Letokhov, *Laser Optoacoustic Spectroscopy*, Vol. 37, Springer, 2013.

128. Liu, G., "Theory of the Photoacoustic Effect in Condensed Matter", *Applied Optics*, Vol. 21, No. 5, pp. 955–960, 1982.

129. Zharov, V., T. Malinsky and R. Kurten, "Photoacoustic Tweezers with a Pulsed Laser: Theory and Experiments", *Journal of Physics D: Applied Physics*, Vol. 38, No. 15, p. 2662, 2005.

130. Knopf, A. C. and A. Lomax, "In-vivo Proton Range Verification: A Review", *Physics in Medicine and Biology*, Vol. 58, No. 15, p. R131, 2013.

131. Grabham, P. and P. Sharma, "The Effects of Radiation on Angiogenesis", *Vascular Cell*, Vol. 5, No. 1, p. 1, 2013.

132. Levin, W., H. Kooy, J. Loeffler and T. DeLaney, "Proton Beam Therapy", *British Journal of Cancer*, Vol. 93, No. 8, pp. 849–854, 2005.

133. Goodman, G., G. Lam, R. Harrison, M. Bergstrom, W. Martin and B. Pate, "The Use of Positron Emission Tomography in Pion Radiotherapy", *International*

*Journal of Radiation Oncology * Biology * Physics*, Vol. 12, No. 10, pp. 1867–1871, 1986.

134. Shirato, H., R. Harrison, R. Kornelsen, G. K. Lam, C. C. Gaffney, G. B. Goodman, E. Grochowski and B. Pate, "Detection of Pion-induced Radioactivity by Autoradiography and Positron Emission Tomography (PET)", *Medical Physics*, Vol. 16, No. 3, pp. 338–345, 1989.

135. Min, C.-H., C. H. Kim, M.-Y. Youn and J.-W. Kim, "Prompt Gamma Measurements for Locating the Dose Falloff Region in the Proton Therapy", *Applied Physics Letters*, Vol. 89, No. 18, p. 183517, 2006.

136. Min, C. H., H. R. Lee, C. H. Kim and S. B. Lee, "Development of Array-type Prompt Gamma Measurement System for In-vivo Range Verification in Proton Therapy", *Medical Physics*, Vol. 39, No. 4, pp. 2100–2107, 2012.

137. Polf, J. C., S. Avery, D. S. Mackin and S. Beddar, "Imaging of Prompt Gamma Rays Emitted During Delivery of Clinical Proton Beams with a Compton Camera: Feasibility Studies for Range Verification", *Physics in Medicine and Biology*, Vol. 60, No. 18, p. 7085, 2015.

138. Jones, K. C., F. Vander Stappen, C. R. Bawiec, G. Janssens, P. A. Lewin, D. Prieels, T. D. Solberg, C. M. Sehgal and S. Avery, "Experimental Observation of Acoustic Emissions Generated by a Pulsed Proton Beam from a Hospital-based Clinical Cyclotron", *Medical Physics*, Vol. 42, No. 12, pp. 7090–7097, 2015.

139. Stevens, S., S. Moore and I. Kaplan, "Early and Late Bone-marrow Changes after Irradiation: MR Evaluation.", *American Journal of Roentgenology*, Vol. 154, No. 4, pp. 745–750, 1990.

140. Gensheimer, M. F., T. I. Yock, N. J. Liebsch, G. C. Sharp, H. Paganetti, N. Madan, P. E. Grant and T. Bortfeld, "In-vivo Proton Beam Range Veri-

fication Using Spine MRI Changes", *International Journal of Radiation Oncology * Biology * Physics*, Vol. 78, No. 1, pp. 268–275, 2010.

141. Yuan, Y., O. C. Andronesi, T. R. Bortfeld, C. Richter, R. Wolf, A. R. Guimaraes, T. S. Hong and J. Seco, "Feasibility Study of In-vivo MRI Based Dosimetric Verification of Proton End-of-range for Liver Cancer Patients", *Radiotherapy and Oncology*, Vol. 106, No. 3, pp. 378–382, 2013.

142. Sulak, L., T. Armstrong, H. Baranger, M. Bregman, M. Levi, D. Mael, J. Strait, T. Bowen, A. Pifer, P. Polakos *et al.*, "Experimental Studies of the Acoustic Signature of Proton Beams Traversing Fluid Media", *Nuclear Instruments and Methods*, Vol. 161, No. 2, pp. 203–217, 1979.

143. Hayakawa, Y., J. Tada, T. Inada, T. Kitagawa, T. Wagai and K. Yosioka, "Acoustic Pulse Generation in Excised Muscle by Pulsed Proton Beam Irradiation and the Possibility of Clinical Application to Radiation Therapy.", *Journal of the Acoustical Society of Japan E*, Vol. 9, No. 5, pp. 255–257, 1988.

144. Tada, J., Y. Hayakawa, K. Hosono and T. Inada, "Time Resolved Properties of Acoustic Pulses Generated in Water and in Soft Tissue by Pulsed Proton Beam Irradiation–A possibility of Doses Distribution Monitoring in Proton Radiation Therapy", *Medical Physics*, Vol. 18, No. 6, pp. 1100–1104, 1991.

145. Hayakawa, Y., J. Tada, N. Arai, K. Hosono, M. Sato, T. Wagai, H. Tsuji and H. Tsujii, "Acoustic Pulse Generated in a Patient During Treatment by Pulsed Proton Radiation Beam", *Radiation Oncology Investigations*, Vol. 3, No. 1, pp. 42–45, 1995.

146. Albul, V., V. Bychkov, S. Vasil'ev, K. Gusev, V. Demidov, E. Demidova, N. Krasnov, A. Kurchanov, V. Luk'yashin and A. Y. Sokolov, "Acoustic Field Generated by a Beam of Protons Stopping in a Water Medium", *Acoustical Physics*, Vol. 51, No. 1, pp. 33–37, 2005.

147. Graf, K., G. Anton, J. Hössl, A. Kappes, T. Karg, U. Katz, R. Lahmann, C. Naumann, K. Salomon and C. Stegmann, "Testing Thermo-acoustic Sound Generation in Water with Proton and Laser Beams", *International Journal of Modern Physics A*, Vol. 21, pp. 127–131, 2006.

148. Terunuma, T., T. Sakae, Y. Hayakawa, A. Nohtomi, Y. Takada, K. Yasuoka and A. Maruhashi, "Waveform Simulation Based on 3D Dose Distribution for Acoustic Wave Generated by Proton Beam Irradiation", *Medical Physics*, Vol. 34, No. 9, pp. 3642–3648, 2007.

149. De Bonis, G., "Acoustic Signals from Proton Beam Interaction in Water–Comparing Experimental Data and Monte Carlo simulation", *Nuclear Instruments and Methods in Physics Research A*, Vol. 604, No. 1, pp. S199–S202, 2009.

150. Bychkov, V., V. Demidov, E. Demidova, B. Ishkhanov, N. Krasnov and V. Luk'yashin, "Angular Distribution of Acoustic Radiation Created in Water by Accelerated Protons", *Acoustical Physics*, Vol. 56, No. 4, pp. 482–485, 2010.

151. Jones, K. C., A. Witztum, C. M. Sehgal and S. Avery, "Proton Beam Characterization by Proton-induced Acoustic Emission: Simulation Studies", *Physics in Medicine and Biology*, Vol. 59, No. 21, p. 6549, 2014.

152. Ahmad, M., L. Xiang, S. Yousefi and L. Xing, "Theoretical Detection Threshold of the Proton-acoustic Range Verification Technique", *Medical Physics*, Vol. 42, No. 10, pp. 5735–5744, 2015.

153. Alsanea, F., V. Moskvin and K. M. Stantz, "Feasibility of RACT for 3D Dose Measurement and Range Verification in a Water Phantom", *Medical Physics*, Vol. 42, No. 2, pp. 937–946, 2015.

154. Assmann, W., S. Kellnberger, S. Reinhardt, S. Lehrack, A. Edlich, P. Thirolf, M. Moser, G. Dollinger, M. Omar, V. Ntziachristos *et al.*, "Ionoacoustic Char-

acterization of the Proton Bragg Peak with Submillimeter Accuracy", *Medical Physics*, Vol. 42, No. 2, pp. 567–574, 2015.

155. Pedroni, E., S. Scheib, T. Böhringer, A. Coray, M. Grossmann, S. Lin and A. Lomax, "Experimental Characterization and Physical Modelling of the Dose Distribution of Scanned Proton Pencil Beams", *Physics in Medicine and Biology*, Vol. 50, No. 3, p. 541, 2005.

156. Patch, S. K., M. K. Covo, A. Jackson, Y. M. Qadadha, K. S. Campbell, R. A. Albright, P. Bloemhard, A. P. Donoghue, C. R. Siero, T. L. Gimpel, S. M. Small, B. F. Ninemire, M. B. Johnson and L. Phair, "Thermoacoustic Range Verification Using a Clinical Ultrasound Array Provides Perfectly Co-registered Overlay of the Bragg Peak onto an Ultrasound Image", *Physics in Medicine and Biolology*, Vol. 61, No. 15, p. 5621, 2016.

157. Jones, K. C., C. M. Seghal and S. Avery, "How Proton Pulse Characteristics Influence Protoacoustic Determination of Proton-beam range: Simulation studies", *Physics in Medicine and Biology*, Vol. 61, No. 6, p. 2213, 2016.

158. Bortfeld, T., "An Analytical Approximation of the Bragg Curve for Therapeutic Proton Beams", *Medical Physics*, Vol. 24, No. 12, pp. 2024–2033, 1997.

159. Erkol, H., E. Aytac-Kipergil and M. B. Unlu, "Photoacoustic Radiation Force on a Microbubble", *Physical Review E*, Vol. 90, No. 2, p. 023001, 2014.

160. Gao, F., X. Feng, R. Zhang, S. Liu, R. Ding, R. Kishor and Y. Zheng, "Single Laser Pulse Generates Dual Photoacoustic Signals for Differential Contrast Photoacoustic Imaging", *Scientific Reports*, Vol. 7, 2017.

161. Beard, P. C., "Photoacoustic Imaging of Blood Vessel Equivalent Phantoms", *International Symposium on Biomedical Optics*, pp. 54–62, International Society for Optics and Photonics, 2002.

162. Cook, J. R., R. R. Bouchard and S. Y. Emelianov, "Tissue-mimicking Phantoms for Photoacoustic and Ultrasonic Imaging", *Biomedical Optics Express*, Vol. 2, No. 11, pp. 3193–3206, 2011.

163. Fonseca, M., B. Zeqiri, P. Beard and B. Cox, "Characterisation of a PVCP based tissue-mimicking phantom for quantitative photoacoustic imaging", *European Conference on Biomedical Optics*, p. 953911, Optical Society of America, 2015.

164. Laufer, J., E. Zhang and P. Beard, "Evaluation of Absorbing Chromophores Used in Tissue Phantoms for Quantitative Photoacoustic Spectroscopy and Imaging", *IEEE Journal of Selected Topics in Quantum Electronics*, Vol. 16, No. 3, pp. 600–607, 2010.

165. Kharine, A., S. Manohar, R. Seeton, R. G. Kolkman, R. A. Bolt, W. Steenbergen and F. F. de Mul, "Poly (vinyl alcohol) Gels for Use as Tissue Phantoms in Photoacoustic Mammography", *Physics in Medicine and Biology*, Vol. 48, No. 3, p. 357, 2003.

166. Culjat, M. O., D. Goldenberg, P. Tewari and R. S. Singh, "A Review of Tissue Substitutes for Ultrasound Imaging", *Ultrasound in Medicine and Biology*, Vol. 36, No. 6, pp. 861–873, 2010.

167. Spirou, G. M., A. A. Oraevsky, I. A. Vitkin and W. M. Whelan, "Optical and Acoustic Properties at 1064 nm of Polyvinyl Chloride-plastisol for Use as a Tissue Phantom in Biomedical Optoacoustics", *Physics in Medicine and Biology*, Vol. 50, No. 14, p. N141, 2005.

168. Avigo, C., N. Di Lascio, P. Armanetti, C. Kusmic, L. Cavigli, F. Ratto, S. Meucci, C. Masciullo, M. Cecchini, R. Pini *et al.*, "Organosilicon Phantom for Photoacoustic Imaging", *Journal of Biomedical Optics*, Vol. 20, No. 4, pp. 046008–046008, 2015.

169. Strohm, E. M., M. C. Kolios, D. K. Hwang, B.-U. Moon and S. S. Tsai, "Development of a Microfluidic Device with Integrated High Frequency Ultrasound Probe for Particle Characterization", *Ultrasonics Symposium (IUS)*, pp. 1960–1963, IEEE, 2014.

170. Avigo, C., N. Di Lascio, P. Armanetti, F. Stea, L. Cavigli, F. Ratto, R. Pini, S. Meucci, M. Cecchini, C. Kusmic *et al.*, "Phantom Studies with Gold Nanorods as Contrast Agents for Photoacoustic Imaging: Novel and Old Approaches", *International Society for Optics and Photonics*, pp. 93234B–93234B, SPIE, 2015.

171. Avigo, C., P. Armanetti, C. Masciullo, N. Di Lascio, L. Cavigli, F. Ratto, R. Pini, M. Cecchini, C. Kusmic, F. Faita *et al.*, "Novel Organosilicon Phantoms as Testing Material for Photoacoustic Imaging", *International Society for Optics and Photonics*, pp. 97000I–97000I, SPIE, 2016.

172. Tsou, J. K., J. Liu, A. I. Barakat and M. F. Insana, "Role of Ultrasonic Shear Rate Estimation Errors in Assessing Inflammatory Response and Vascular Risk", *Ultrasound in Medicine and Biology*, Vol. 34, No. 6, pp. 963–972, 2008.

173. Tiana, Y., N. Wua, X. Zoub and X. Wang, "Fiber Optic Ultrasound Generator Using Periodic Gold Nanopattern Fabricated by Focused Ion Beam", *Proceedings of SPIE*, Vol. 8694, pp. 86942E–1, 2013.

174. De Jong, N., A. Bouakaz and P. Frinking, "Basic Acoustic Properties of Microbubbles", *Echocardiography*, Vol. 19, No. 3, pp. 229–240, 2002.

175. Bosschaart, N., G. J. Edelman, M. C. Aalders, T. G. van Leeuwen and D. J. Faber, "A Literature Review and Novel Theoretical Approach on the Optical Properties of Whole Blood", *Lasers in Medical Science*, Vol. 29, No. 2, p. 453, 2014.

176. Wang, L. V. and H. Wu, *Biomedical Optics: Principles and Imaging*, John Wiley and Sons, 2012.

177. Klibanov, A. L., M. S. Hughes, F. S. Villanueva, R. J. Jankowski, W. R. Wagner, J. K. Wojdyla, J. H. Wible and G. H. Brandenburger, "Targeting and Ultrasound Imaging of Microbubble-Based Contrast Agents", *Magnetic Resonance Materials in Physics, Biology and Medicine*, Vol. 8, No. 3, pp. 177–184, 1999.

178. Sboros, V., "Response of Contrast Agents to Ultrasound", *Advanced Drug Delivery Reviews*, Vol. 60, No. 10, pp. 1117–1136, 2008.

179. Coffey, W. T. and Y. P. Kalmykov, *The Langevin equation: With Applications to Stochastic Problems in Physics, Chemistry and Electrical Engineering*, Vol. 27, World Scientific, 2012.

180. Jones, P. H., O. M. Maragò and G. Volpe, *Optical tweezers: Principles and Applications*, Cambridge University Press, 2015.

181. Svoboda, K. and S. M. Block, "Biological Applications of Optical Forces", *Annual Review of Biophysics and Biomolecular Structure*, Vol. 23, No. 1, pp. 247–285, 1994.

182. Volpe, G. and G. Volpe, "Simulation of a Brownian particle in an Optical Trap", *American Journal of Physics*, Vol. 81, No. 3, pp. 224–230, 2013.

183. Bartlett, P. and S. Henderson, "Three-dimensional Force Calibration of a Single-Beam Optical Gradient Trap", *Journal of Physics: Condensed Matter*, Vol. 14, No. 33, p. 7757, 2002.

184. Tolić-Nørrelykke, S. F., E. Schäffer, J. Howard, F. S. Pavone, F. Jülicher and H. Flyvbjerg, "Calibration of Optical Tweezers with Positional Detection in the Back Focal Plane", *Review of Scientific Instruments*, Vol. 77, No. 10, p. 103101, 2006.

185. Jun, Y., S. K. Tripathy, B. R. Narayanareddy, M. K. Mattson-Hoss and S. P. Gross, "Calibration of Optical Tweezers for In-vivo Force Measurements: How

do Different Approaches Compare?", *Biophysical Journal*, Vol. 107, No. 6, pp. 1474–1484, 2014.

186. Xiang, L., S. Tang, M. Ahmad and L. Xing, "High Resolution X-ray-Induced Acoustic Tomography", *Scientific Reports*, Vol. 6, 2016.

187. Morse, P. and H. Feshbach, *Methods of Theoretical Physics*, Technology Press, 1946.

188. Gottschalk, B., A. Koehler, R. Schneider, J. Sisterson and M. Wagner, "Multiple Coulomb Scattering of 160 MeV Protons", *Nuclear Instruments and Methods in Physics Research Section B*, Vol. 74, No. 4, pp. 467–490, 1993.

189. Papash, A. and Y. G. Alenitsky, "Commercial Cyclotrons. Part I: Commercial Cyclotrons in the Energy Range 10–30 MeV for Isotope Production", *Physics of Particles and Nuclei*, Vol. 39, No. 4, pp. 597–631, 2008.

190. Slater, J. M., J. O. Archambeau, D. W. Miller, M. I. Notarus, W. Preston and J. D. Slater, "The Proton Treatment Center at Loma Linda University Medical Center: Rationale for and Description of its Development", *International Journal of Radiation Oncology * Biology * Physics*, Vol. 22, No. 2, pp. 383–389, 1992.

191. Caporaso, G. J., Y.-J. Chen and S. E. Sampayan, "The Dielectric Wall Accelerator", *Reviews of Accelerator Science and Technology*, Vol. 2, No. 01, pp. 253–263, 2009.

192. Shou-Xian, F., G. Xia-Ling, T. Jing-Yu, C. Yuan, D. Chang-Dong, D. Hai-Yi, F. Shi-Nian, J. Yi, S. Hang, O. Hua-Fu *et al.*, "ATPF–a Dedicated Proton Therapy Facility", *Chinese Physics C*, Vol. 34, No. 3, p. 383, 2010.

193. Akulinichev, S., L. V. Kravchuk *et al.*, "Medical Applications Of INR Proton Linac", Vol. 1, 2011.

194. Amaldi, U., S. Braccini and P. Puggioni, "High Frequency Linacs for Hadrontherapy", *Reviews of Accelerator Science and Technology*, Vol. 2, No. 01, pp. 111–131, 2009.

195. Pedroni, E., R. Bacher, H. Blattmann, T. Böhringer, A. Coray, A. Lomax, S. Lin, G. Munkel, S. Scheib, U. Schneider *et al.*, "The 200-MeV Proton Therapy Project at the Paul Scherrer Institute: Conceptual Design and Practical Realization", *Medical Physics*, Vol. 22, No. 1, pp. 37–53, 1995.

196. Lomax, A. J., T. Böhringer, A. Bolsi, D. Coray, F. Emert, G. Goitein, M. Jermann, S. Lin, E. Pedroni, H. Rutz *et al.*, "Treatment Planning and Verification of Proton Therapy Using Spot Scanning: Initial Experiences", *Medical Physics*, Vol. 31, No. 11, pp. 3150–3157, 2004.

197. Nishiuchi, M., H. Sakaki, T. Hori, P. Bolton, K. Ogura, A. Sagisaka, A. Yogo, M. Mori, S. Orimo, A. Pirozhkov *et al.*, "Laser-Driven Proton Accelerator for Medical Application", Vol. 1, 2010.

198. Chu, W., B. Ludewigt and T. Renner, "Instrumentation for Treatment of Cancer Using Proton and Light-ion Beams", *Review of Scientific Instruments*, Vol. 64, No. 8, pp. 2055–2122, 1993.

199. Alsanea, F. M., *Feasibility of Pulsed Proton Acoustics for 3D Dosimetry*, Ph.D. Thesis, 2014.

200. Noda, K. *et al.*, "Review of Hadron Therapy Accelerators Worldwide and Future Trends", *Proceedings of International Particle Accelerator Conference*, p. 3784, 2011.

201. Paganetti, H., *Proton Therapy Physics*, CRC Press, 2011.

202. Ruggiero, A., *Brief History Of FFAG Accelerators*, Brookhaven National Laboratory, 2006.

203. Sampayan, S. E., G. J. Caporaso and H. C. Kirbie, "Enhanced Dielectric-wall Linear Accelerator", Vol. 1, Sep. 22 1998, uS Patent 5, 811,944.

204. Daido, H., M. Nishiuchi and A. S. Pirozhkov, "Review of Laser-driven Ion Sources and Their Applications", *Reports on Progress in Physics*, Vol. 75, No. 5, p. 056401, 2012.

205. Koehler, A., R. Schneider and J. Sisterson, "Range Modulators for Protons and Heavy Ions", *Nuclear Instruments and Methods*, Vol. 131, No. 3, pp. 437–440, 1975.

206. Urie, M., J. Sisterson, A. Koehler, M. Goitein and J. Zoesman, "Proton Beam Penumbra: Effects of Separation Between Patient and Beam Modifying Devices", *Medical Physics*, Vol. 13, No. 5, pp. 734–741, 1986.

207. Kanai, T., K. Kawachi, Y. Kumamoto, H. Ogawa, T. Yamada, H. Matsuzawa and T. Inada, "Spot Scanning System for Proton Radiotherapy", *Medical Physics*, Vol. 7, No. 4, pp. 365–369, 1980.

208. Yokota, W., M. Fukuda, S. Okumura, K. Arakawa, Y. Nakamura, T. Nara, T. Agematsu and I. Ishibori, "Performance and Operation of a Beam Chopping System for a Cyclotron with Multiturn Extraction", *Review of Scientific Instruments*, Vol. 68, No. 4, pp. 1714–1719, 1997.

209. Kleeven, W., M. Abs, E. Forton, S. Henrotin, Y. Jongen, V. Nuttens, Y. Paradis, E. Pearson, S. Quets, J. Van de Walle *et al.*, "The IBA Superconducting Synchrocyclotron Project S2C2", *Proceedings of Cyclotrons*, 2013.

210. Smith, A. R., "Vision 20/ 20: Proton Therapy", *Medical Physics*, Vol. 36, No. 2, pp. 556–568, 2009.

211. Smith, A. R., "Proton Therapy", *Physics in Medicine and Biology*, Vol. 51, No. 13, p. R491, 2006.

212. Niermann, B., I. L. Budunoglu, K. Gürel, M. Böke, F. Ö. Ilday and J. Winter, "Application of a Mode-locked Fiber Laser for Highly Time Resolved Broadband Absorption Spectroscopy and Laser-assisted Breakdown on Micro-plasmas", *Journal of Physics D: Applied Physics*, Vol. 45, No. 24, p. 245202, 2012.